Karlsruhe Institute of Technology

NLO QCD corrections to $W\gamma$ production via vector boson fusion

Diplomarbeit
von

Nicolas Kaiser

An der Fakultät für Physik
Institut für Theoretische Physik

Referent:	Prof. Dr. D. Zeppenfeld
Korreferent:	Prof. Dr. U. Nierste

Bearbeitungszeit: 14. Juni 2012 – 14. Juni 2013

Ich versichere, dass ich diese Arbeit selbstständig verfasst und ausschließlich die angegebenen Hilfsmittel verwendet habe.

Nicolas Kaiser
Karlsuhe, den 15. Juni 2013

Als Diplomarbeit anerkannt.

Prof. Dr. D. Zeppenfeld
Karlsuhe, den 15. Juni 2013

CONTENTS

1. Motivation **1**

2. Theoretical background **5**
2.1. Quantum field theory . . . 5
2.1.1. Regularization and renormalization . . . 7
2.2. Standard Model . . . 8
2.2.1. Electroweak sector . . . 9
2.2.2. Quantum chromodynamics . . . 12
2.2.3. Ward identities . . . 13
2.3. Effective field theory . . . 14
2.3.1. Fermi's theory of β-decay . . . 15
2.4. Anomalous couplings . . . 16
2.4.1. Form factor . . . 18
2.5. Proton-proton collider . . . 19
2.5.1. PDFs . . . 19
2.6. Event selection at colliders: Cuts . . . 20
2.6.1. Vector boson fusion cuts . . . 21
2.6.2. Frixione photon isolation . . . 22

3. Implementation **23**
3.1. VBFNLO . . . 23
3.1.1. Numerical integration . . . 23
3.1.2. Importance sampling . . . 24
3.1.3. Program architecture . . . 25
3.2. Leading order calculation . . . 26
3.2.1. Matrix element . . . 27
3.2.2. Construction in VBFNLO . . . 28
3.2.3. Gauge terms . . . 31
3.2.4. CKM matrix . . . 31
3.3. Phase space . . . 32
3.4. Next-to-leading-order calculation . . . 34
3.5. Real emission contribution . . . 35
3.5.1. Catani-Seymour dipole subtraction . . . 36

3.6. Virtual corrections . . . 41
3.6.1. Ward identity test . . . 42
3.6.2. Dimensional reduction . . . 44
3.6.3. Subtraction of Born-types . . . 45
3.7. Anomalous couplings . . . 45

4. Checks **47**
4.1. Matrix elements . . . 47
4.2. Cross sections . . . 47
4.3. Dipoles . . . 49
4.4. Gauge tests . . . 50
4.4.1. Leading order . . . 50
4.4.2. Real emission . . . 51
4.4.3. Virtual corrections . . . 52
4.5. Virtual contributions . . . 53
4.5.1. Input . . . 53
4.5.2. Poles . . . 54
4.5.3. Comparison with different implementation . . . 55
4.5.4. Dependence on intrinsic scale . . . 55
4.5.5. Precision of the Ward test . . . 55
4.6. Relation between real emission and virtual corrections . . . 56
4.7. Anomalous couplings . . . 57

5. Phenomenology **59**
5.1. Numerical results . . . 59
5.2. Scale dependence . . . 61
5.3. Energy dependence . . . 65
5.4. LO vs NLO distributions . . . 66
5.5. Final state radiation . . . 67
5.6. Helicity correlations . . . 69
5.7. Jet veto . . . 70
5.8. Anomalous couplings . . . 72
5.8.1. Differential distributions . . . 72
5.8.2. Two dimensional cross sections analysis . . . 76
5.8.3. Sensitivity analysis . . . 78

6. Conclusion **81**

7. Zusammenfassung **85**

Appendix **89**
A. Dimension 8 operators . . . 89
B. Form factors . . . 91
C. Sensitivity analysis . . . 92
C.1. $\mathcal{L}_{T,0} - \mathcal{L}_{T,1}$ . . . 93
C.2. $\mathcal{L}_{T,0} - \mathcal{L}_{T,5}$ . . . 95
C.3. $\mathcal{L}_{T,0} - \mathcal{L}_{T,6}$ . . . 97
C.4. $\mathcal{L}_{T,1} - \mathcal{L}_{T,5}$ . . . 99
C.5. $\mathcal{L}_{T,1} - \mathcal{L}_{T,6}$ . . . 101
C.6. $\mathcal{L}_{T,5} - \mathcal{L}_{T,6}$ . . . 103

Bibliography **105**

Acknowledgements **109**

CHAPTER 1

MOTIVATION

Our current understanding of the universe is based on two theories: General Relativity describes gravity and the Standard Model (SM) of particle physics the electromagnetic, weak and strong interactions between particles. The SM is a quantum field theory, that was developed in the early 1970s. Its predictions have been confirmed in experiments with remarkable precision. It is a gauge theory, which means that the Lagrangian describing the interaction between particles is invariant under given gauge transformations.
The $SU(2)_L \times U(1)_Y$ gauge group describes the electroweak part of the SM. This symmetry is spontaneously broken down to the $U(1)_{em}$ gauge group that describes quantum electrodynamics (QED), the theory of interactions between photons and electrically charged particles. Spontaneous symmetry breaking via the Higgs mechanism enables gauge bosons like the W and Z bosons to have a non-zero mass.
The gauge bosons are the force carriers, which are exchanged between fermions when they interact. Protons and neutrons, the main components of the visible matter that surrounds us, consist of partons. Their interaction is described by quantum chromodynamics (QCD), a $SU(3)_c$ gauge theory. Although the Standard Model is a remarkably successful theory, there are still several phenomena that do not fit into its framework:

- It seems likely that all three interactions evolved from only one interaction in the early universe. Therefore, a unification of all three SM interactions is expected, in analogy to the unification of the electromagnetic and the weak interaction. This unification of forces is not possible in the Standard Model.
- Gravity, the very first fundamental force that physicists recognized as such, is not described by the Standard Model.
- From the trajectories of stars, we know that there must be more mass in the universe than the baryonic matter we observe [1]. The theory of Big Bang nucleosynthesis tells us that this additional matter can not be baryonic. The SM does not provide a candidate for this so-called dark matter.
- We know that the universe is expanding and that this expansion is accelerating. This can be inferred from the observation of the redshift of distant type 1a supernovae. Since gravitation is expected to slow down the expansion there must be a negative pressure on the universe acting contrary to gravity. This is called dark energy, which is another phenomenon described neither by the Standard Model nor by General Relativity.

- When the Standard Model was formulated, the neutrino masses were set to zero since they were known to be extremely small. From neutrino oscillation experiments, we know that at least two of the three neutrinos have a mass greater than zero. Although this can be described in the SM, there is no explanation as to why the neutrino masses are so much smaller than the masses of the other fermions.
- The measured g-factor of the muon, the constant of proportionality between its spin and magnetic moment, shows a significant deviation from its SM expectation [2].
- The fundamental parameters of the Standard Model i.e. masses and couplings have to be determined experimentally. A more satisfying situation would be if a general theory was able to predict these parameters.
- The loop corrections to the Higgs mass are proportional to the energy scale squared up to which the theory is valid. Assuming the Standard Model valid up to the Planck scale, the physical parameters have to be extremely fine-tuned, which is very unnatural. This is called the hierarchy problem.

These features do not mean that the Standard Model is wrong but rather that it is probably an effective field theory (EFT), which is only valid up to a certain energy scale. This would imply that we need a new theory to describe the fundamental interactions of particles at higher energies. There are many such theories describing physics beyond the SM, including Supersymmetry or String Theory.

Currently, the most powerful tool in the search for new physics is the Large Hadron Collider (LHC) at CERN. It provides physicists with the opportunity to examine phenomena at unprecedented energies. Since a scalar boson has been discovered recently [3, 4], a lot of effort is being put into measuring its quantum numbers and its couplings to other particles, in order to determine whether it is the Standard Model Higgs boson.
The dominant Higgs production channel at 8 TeV is gluon fusion, because gluons give the largest partonic contribution to protons at small values of Feynman x. The second largest channel is vector boson fusion (VBF), which provides a relatively clear detector signal because of its two tagging jets. The corresponding leading order Feynman diagram is depicted in figure 1.1a[1]. Moreover, this channel will become more important at higher energies since the cross section of VBF processes does not decrease with rising center-of-mass energy.

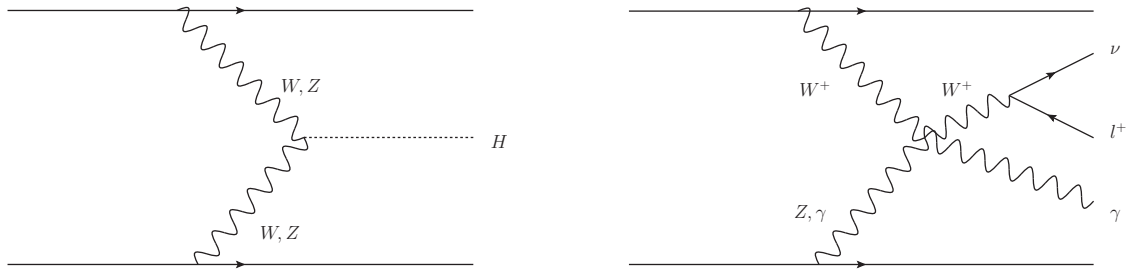

(a) Higgs production via VBF **(b)** $W^+\gamma$ production via VBF

Figure 1.1: The left Feynman diagram shows Higgs production via vector boson fusion. The right diagram shows one contribution to $W^+\gamma$ production via VBF.

[1]The Feynman diagrams and drawings in this work were created with the Gnu program JaxoDraw.

In addition to the examination of the newly discovered scalar boson and its properties, triple and quartic gauge boson couplings provide a promising avenue to probe the electroweak sector of the Standard Model. Deviations from the SM values of those couplings, which occur for example in diboson production via vector boson fusion, would be a strong hint for new physics. In order to simulate anomalous gauge boson couplings, we have implemented operators that allow us to modify the triple and quartic couplings. The approach is to extend the Standard Model with an effective field theory. This EFT contains terms in its Lagrangian that modify triple and quartic gauge boson couplings via dimension 6 and dimension 8 operators, respectively.

These couplings can occur in the production of multiple weak gauge bosons, e.g. $pp \to W\gamma + X$. Final state photon processes are especially interesting since they have a relatively high cross section. The higher the cross section, the higher the number of events one obtains for a given luminosity.
There are two basic mechanisms for $W\gamma$ production in association with two jets: the QCD induced process, which is of order $\mathcal{O}(\alpha_{em}^3\alpha_S^2)$, and the VBF process, which is of order $\mathcal{O}(\alpha_{em}^5)$ at leading order and including the leptonic decay of the W. One contribution to electroweak $W^+\gamma$ production via VBF is depicted in figure 1.1b and two contributions to QCD $W^+\gamma jj$ production are shown in figure 1.2. Despite the suppression by a factor of $(\alpha_{em}/\alpha_S)^2$, the VBF mechanism is very promising since it has a very clear signal, which helps to increase the signal to background ratio.

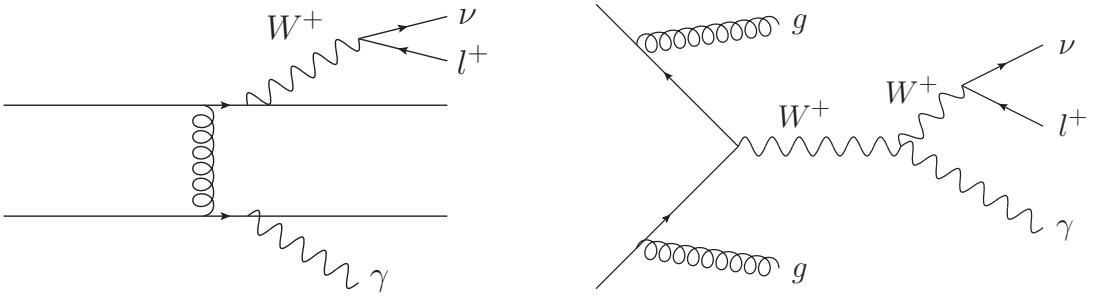

(a) QCD $W^+\gamma jj$ production via t-channel gluon exchange

(b) QCD $W^+\gamma jj$ production via s-channel

Figure 1.2: These two Feynman diagrams occur in QCD $W^+\gamma jj$ production. The right diagram contains the $WW\gamma$ coupling.

The QCD diboson mechanism contains at most triple gauge boson couplings. However, these couplings occur already in $W^+\gamma$ diboson production, which is, including the leptonic decay of the W, of order $\mathcal{O}(\alpha_{em}^3)$ and presented in figure 1.3.

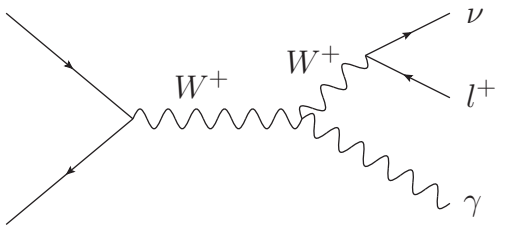

Figure 1.3: This Feynman diagram represents one contribution to $W^+\gamma$ diboson production. It contains the $WW\gamma$ coupling.

The QCD induced contributions to $pp \to W\gamma jj$ depicted in figure 1.3 contribute to the real emission of the NNLO QCD corrections to $W\gamma$ diboson production. Although they are

suppressed by a factor of α_S^2, the new channels and topologies, e.g. the gluon induced channel $gg \to W\gamma jj$, can result in non-negligible corrections in some regions of the phase space [5]. But in general, diboson production is more suitable for the examination of triple gauge boson couplings. Those couplings are currently under investigation at the LHC and the parameters of the dimension 6 operators describing deviations from their SM expectations are already strongly constrained [6]. But the parameters of the dimension 8 operators, which modify quartic gauge boson couplings, are currently significantly less restricted [7]. These couplings occur at leading order in triboson and diboson VBF processes.

Figure 1.1b shows that two quartic gauge boson couplings, namely $WW\gamma\gamma$ and $WWZ\gamma$, occur in $W^{\pm}\gamma$ production via VBF, or in other words, electroweak $W\gamma jj$ production. These couplings can be probed by looking for deviations from the SM predictions in suitable observables. Effects of anomalous couplings are usually visible at high energies. Therefore the 14 TeV runs of the LHC scheduled for 2014 will provide us with the possibility to investigate quartic gauge boson couplings with high precision for the first time.

In order to probe the theoretical predictions in an experiment, these predictions need to be very precise. For our calculation of the $W^{\pm}\gamma jj$ cross section, we use perturbative quantum field theory, which implies that we are left with a theoretical uncertainty on our results. The scale dependence of the cross section is usually used to estimate this uncertainty. The scale dependence, and with it the uncertainty, can be significantly reduced by calculating the next-to-leading-order (NLO) cross section, which is one of the central topics of this thesis. After the NLO calculation, we focus on phenomenological implications, especially anomalous coupling effects. Our calculation includes the leptonic decay of the W boson with all off-shell effects and spin correlations.

Following the discussion of the motivation in this chapter, the theoretical background will be explained in chapter 2. The implementation of the process in the parton-level Monte-Carlo program VBFNLO [8] will be described in chapter 3. In order to assure the correctness of the implementation, we conducted numerous checks, which will be listed in chapter 4. In chapter 5, *Phenomenology*, we examine the physical effects. Finally, a summary and outlook is given in chapter 6.

CHAPTER 2

THEORETICAL BACKGROUND

In this chapter, the underlying theory for the calculation presented in this thesis will be explained. After a general introduction to quantum field theory, the Standard Model of particle physics will be presented. These topics are treated in more detail in textbooks like e.g. *'An Introduction to Quantum Field Theory'* by Peskin and Schroeder [9]. The approach of effective field theories will be explained as well as how it can be used to parametrize the effects of anomalous gauge boson couplings. Since this calculation is intended to simulate the process $pp \to W^{\pm}\gamma jj$ at the LHC, we will also look at the basics of collider physics.

2.1. Quantum field theory

The theoretical basis of most theories in particle physics is quantum field theory. Our goal is to predict quantities that can be measured in experiments, such as cross sections, differential distributions or decay rates. Therefore, we need a mathematical framework that describes the transition of a given set of initial state particles to a given set of final state particles. We make use of the Lagrange and Hamilton formalisms familiar from classical mechanics. The transition of two particles with momenta $\vec{p}_a$ and $\vec{p}_b$ to final state particles with momenta $\vec{k}_1 \ldots, \vec{k}_n$ can be described using the bra-ket formalism used in quantum mechanics

$$\begin{aligned} {}_{out}\langle \vec{k}_1, \vec{k}_2, \ldots, \vec{k}_n | \vec{p}_a, \vec{p}_b \rangle_{in} &= \lim_{t\to\infty} \langle \vec{k}_1, \vec{k}_2, \ldots, \vec{k}_n, t | \vec{p}_a, \vec{p}_b, -t \rangle \\ &= \lim_{t\to\infty} \langle \vec{k}_1, \vec{k}_2, \ldots, \vec{k}_n | e^{-iH(2t)} | \vec{p}_a, \vec{p}_b \rangle \\ &\equiv \langle \vec{k}_1, \vec{k}_2, \ldots, \vec{k}_n | S | \vec{p}_a, \vec{p}_b \rangle \,. \end{aligned} \tag{2.1}$$

The initial and the final state can be described as asymptotic states in the limit $t \to \pm\infty$, as in the first line of equation (2.1). In the second line, we just express this time dependence by the time-evolution operator. The Hamilton operator comprises a free term and an interaction term, which are closely related to the Lagrangian describing the interaction

$$H = H_0 + H_I, \qquad H_I = -\int d^3x \mathcal{L}_I. \tag{2.2}$$

It is useful to separate the Hamiltonian into an interaction part H_I describing the dynamics and a free part H_0 describing the kinematics. H_I can be interpreted as a small perturbation

of H_0. In the last line of equation (2.1), we define the S matrix as the time-evolution operator in the limit of large t.

In quantum field theory, so-called second quantization is used, which is reflected in the multi-particle initial and final states in equation (2.1). This allows us to express the fields in terms of the annihilation and creation operators. To illustrate this, in the case of the Klein-Gordon field we have

$$\phi(x) = \int \frac{d^3p}{(2\pi)^3} \frac{1}{\sqrt{2E_p}} \left(a_p e^{-ip\cdot x} + a_p^\dagger e^{ip\cdot x} \right). \tag{2.3}$$

The creation operator $a_p^\dagger$ creates a particle with momentum p while the annihilation operator a_p annihilates a particle with momentum p.

The next step is to divide the S matrix into two parts

$$S = \mathbb{1} + iT. \tag{2.4}$$

The identity part of the S matrix represents the diagrams, in which the particles do not interact while iT denotes the part with the interaction diagrams. With this, we can define the transition matrix element $\mathcal{M}$ via

$$\langle \vec{k}_1, \vec{k}_2, \ldots, \vec{k}_n | iT | \vec{p}_a, \vec{p}_b \rangle = (2\pi)^4 \delta^4 \left(p_a + p_b - \sum_i k_f^i \right) i\mathcal{M}\left(p_a, p_b \to \{k_f^i\} \right). \tag{2.5}$$

The matrix element squared $|\mathcal{M}|^2$ is the probability of the transition $p_a, p_b \to \{k_f^i\}$ and the delta function assures the conservation of momenta. So far, $\langle \vec{k}_1, \vec{k}_2, \ldots, \vec{k}_n|$ and $|\vec{p}_a, \vec{p}_b\rangle$ are eigenstates of H, but we would like to replace them with the corresponding eigenstates of H_0. This is indeed possible and after a lengthy calculation one obtains

$$\begin{aligned} &\langle \vec{k}_1, \vec{k}_2, \ldots, \vec{k}_n | iT | \vec{p}_a, \vec{p}_b \rangle = \\ &\frac{1}{N} \lim_{t\to\infty(1-i\epsilon)} \left({}_0\langle \vec{k}_1, \vec{k}_2, \ldots, \vec{k}_n | T \left(\exp\left[-i \int_{-t}^{t} dt' H_I(t') \right] \right) |\vec{p}_a, \vec{p}_b\rangle_0 \right)_{\substack{connected,\\ amputated}}, \end{aligned} \tag{2.6}$$

where T denotes the time ordering operator and $1/N$ is a normalization factor. The shift of the t integration by a small imaginary part is done to remove all eigenstates of H above the ground state. The subscript 'connected' means that we do not take vacuum bubble diagrams into account and 'amputated' indicates that we do not consider diagrams with loops just on one external leg as these loops do not affect the scattering process.

The initial and the final state in equation (2.6) can be expressed in terms of their corresponding fields and the ground state of H_0. The exponential function can be rewritten as

$$\lim_{t\to\infty(1-i\epsilon)} \exp\left[-i \int_{-t}^{t} dt' H_I(t') \right] = \exp\left[i \int d^4x \mathcal{L}_I \right]. \tag{2.7}$$

The general idea now is to expand the exponential function in the coupling, which is usually small. After applying Wick's theorem and the Lehmann-Symanzik-Zimmermann (LSZ) reduction formula, we obtain the Feynman rules for our theory. With these rules, it is possible to calculate the transition matrix element $\mathcal{M}$ using a diagrammatic representation called Feynman diagrams.

Expanding the exponential function, we get diagrams of different orders in the coupling. The first non-vanishing order is called leading order (LO) and the next higher order is referred

to as next-to-leading order (NLO). For the calculation of one fixed order, one has to take all possible Feynman diagrams into account. This concept will be explained briefly with a well known example from quantum electrodynamics, namely Compton scattering. At leading order, we have two Feynman diagrams presented in figure 2.1.

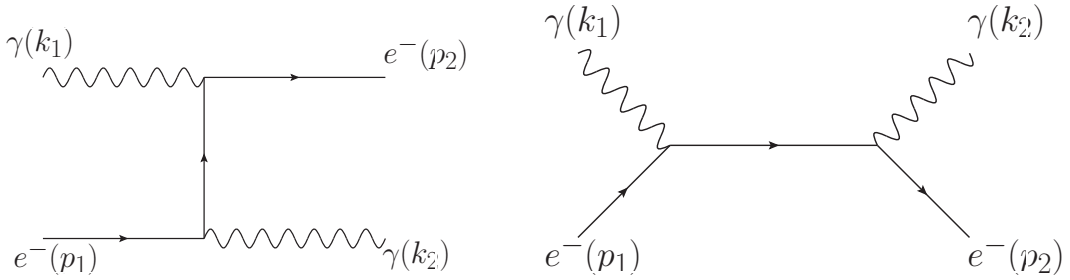

Figure 2.1: These are the two possible Feynman diagrams for Compton scattering at leading order.

At next-to-leading order, two new topologies arise. An additional photon can be radiated off the fermion line. These contributions are called real emission. Moreover, a virtual photon can be produced and annihilated on one fermion line. Due to the uncertainty principle this photon can carry all possible momenta. For illustration, two diagrams are depicted in figure 2.2.

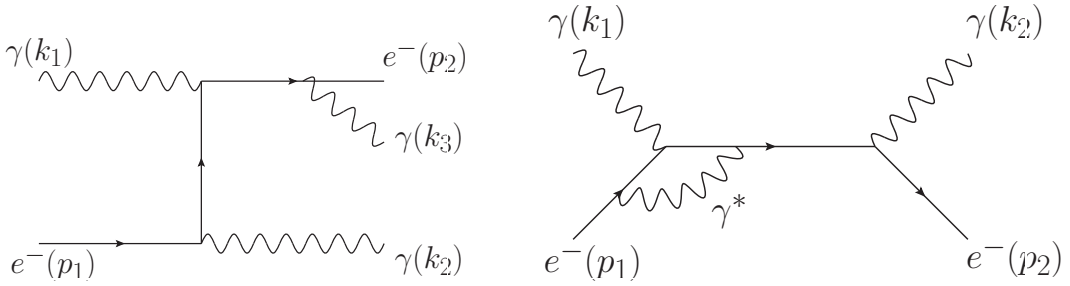

Figure 2.2: At next-to-leading order, real emission diagrams (left diagram) appear as well as virtual corrections (right diagram).

The LO and the NLO cross section are related by the so-called K-factor, which is defined as

$$K = \frac{\sigma_{NLO}}{\sigma_{LO}}. \tag{2.8}$$

Thus the K-factor indicates how large the NLO corrections are.

2.1.1. Regularization and renormalization

The loop integrals that occur at higher perturbative orders can be mathematically divergent. Since physical quantities in nature are always finite these divergences need to be regularized. This is done by introducing renormalized physical quantities

$$X_0 = Z_X X = X + \delta X \qquad \text{with} \qquad \delta X = (Z-1)X, \tag{2.9}$$

where X_0 and X denote the bare and renormalized quantities respectively, Z_X is the renormalization constant and δX the counterterm. Technically, one can use dimensional regularization,

which means that the loop integrals are evaluated in $d = 4 - 2\epsilon$ dimensions, to transform the divergences into $1/\epsilon^n$ terms that can be analytically absorbed into the counterterms.

The transformation in equation (2.9) changes the Lagrangian and leads to additional Feynman diagrams, which have to be taken into account. If one considers all possible diagrams when calculating a matrix element $\mathcal{M}$, it will be finite. The counterterms can be written as

$$\delta X = \sum_i \frac{1}{\epsilon^i} CT_i + \delta X^{fin}, \tag{2.10}$$

where $\sum_i \frac{1}{\epsilon^i} CT_i$ represents the counterterms that cancel the divergences and δX^{fin} is an additional finite term. There are several possible schemes for the choice of δX^{fin}. In the minimal substitution (MS) scheme, this term is simply set to zero, $\delta X^{fin} = 0$. In the on-shell scheme, one demands that the renormalized quantity agrees with the tree-level quantity, $X = X^{tree}$, at a given phase space point.

For the renormalization of the coupling constant, it is necessary to introduce an additional scale in order to maintain the correct dimension. This leads to a general dependence of the physical quantities on this renormalization scale μ_R. This dependence is described by the renormalization group equations (RGEs), partial differential equations with respect to μ_R. The dependence of the coupling on μ_R is given by the β function

$$\beta \equiv \mu_R \frac{dg}{d\mu_R}. \tag{2.11}$$

This effect is called running and leads to very different effects depending on the underlying theory, which will be demonstrated later on.

2.2. Standard Model

The Standard Model (SM) of particle physics is a relativistic quantum field theory. It comprises quantum chromodynamics and the electroweak interaction. Quantum chromodynamics (QCD) describes the interaction between quarks and gluons, which make up the baryonic matter. The electroweak (EW) sector covers the electromagnetic interaction, namely the coupling of photons to electrically charged particles, and the weak interaction, which describes e.g. β-decay. Matter consists of spin 1/2 fermions and the forces are mediated via spin 1 bosons. In addition, the spin 0 Higgs boson arises from spontaneous symmetry breaking in the EW sector.

The Standard Model can be described with the gauge symmetry groups

$$SU(3)_c \times SU(2)_L \times U(1)_{Y_W}. \tag{2.12}$$

The c with $SU(3)_c$ stands for the color charge of QCD. Fermions with right-handed chirality are singlets under $SU(2)_L$, thus the L indicates that only left-handed fermions posses a non-zero weak isospin and Y_W stands for the weak hyper charge.

2.2.1. Electroweak sector

The electroweak sector of the SM is described by the Glashow-Weinberg-Salam (GWS) theory [10, 11, 12]. Its symmetry group is

$$SU(2)_L \times U(1)_{Y_W}. \tag{2.13}$$

Each gauge group is associated with a gauge field

$$SU(2)_L \;\rightarrow\; W^a_\mu, \qquad a = 1, 2, 3, \tag{2.14}$$

$$U(1)_{Y_W} \;\rightarrow\; B_\mu. \tag{2.15}$$

These gauge fields transform under the adjoint representation of the corresponding symmetry group. With the covariant derivative

$$D_\mu = \partial_\mu + igW^a_\mu \frac{\sigma^a}{2} + ig' B_\mu \frac{Y_W}{2}, \tag{2.16}$$

where g and g' are the couplings of $SU(2)$ and $SU(1)$, respectively and σ^a the Pauli matrices, we can already write down the Lagrangian for the fermions

$$\mathcal{L}_{Ferm} = \sum_{\substack{x=\{l,q\} \\ j}} i\overline{L}^x_j \not{D} L^x_j + \sum_{\substack{x=\{l,u,d\} \\ j}} i\overline{R}^x_j \not{D} R^x_j. \tag{2.17}$$

The index j runs over the three particle generations and L stands for fermion doublets under $SU(2)_L$ with left-handed chirality. The fermions with right-handed chirality denoted by R are singlets under this group and thus $g' = 0$ for right-handed fermions. The index x runs over leptons and quarks for the left-handed fermions and over leptons and up-type and down-type quarks for right-handed fermions. Table 2.1 shows all fermions and their $SU(2)_L \times U(1)_{Y_W}$ quantum numbers.

$SU(2)$ doublets L			Q	T^3_W	Y_W
$\begin{pmatrix} \nu_e \\ e^- \end{pmatrix}_L$	$\begin{pmatrix} \nu_\mu \\ \mu^- \end{pmatrix}_L$	$\begin{pmatrix} \nu_\tau \\ \tau^- \end{pmatrix}_L$	0 -1	$+\frac{1}{2}$ $-\frac{1}{2}$	-1
$\begin{pmatrix} u \\ d \end{pmatrix}_L$	$\begin{pmatrix} c \\ s \end{pmatrix}_L$	$\begin{pmatrix} t \\ b \end{pmatrix}_L$	$+\frac{2}{3}$ $-\frac{1}{3}$	$+\frac{1}{2}$ $-\frac{1}{2}$	$+\frac{1}{3}$

$SU(2)$ singlets R			Q	T^3_W	Y_W
e^-_R	μ^-_R	τ^-_R	-1	0	-2
u_R	c_R	t_R	$+\frac{2}{3}$	0	$+\frac{4}{3}$
d_R	s_R	b_R	$-\frac{1}{3}$	0	$-\frac{2}{3}$

Table 2.1: This table shows all SM fermions arranged according to their transformations under $SU(2)$ and their EW quantum numbers.

T^3_W denotes the weak isospin, the quantum number of $SU(2)_L$. The electrical charge can be computed from the weak quantum numbers according to

$$Q = T^3_W + \frac{Y_W}{2}. \tag{2.18}$$

The GWS theory is a non-abelian gauge theory, which leads to gauge boson self interactions. If we look at the gauge part of the Lagrangian,

$$\mathcal{L}_{gauge} = -\frac{1}{4}W^a_{\mu\nu}W^{a\mu\nu} - \frac{1}{4}B_{\mu\nu}B^{\mu\nu} \quad \text{with} \tag{2.19}$$

$$W^a_{\mu\nu} = \partial_\mu W^a_\nu - \partial_\nu W^a_\mu + g f^{abc} W^b_\mu W^c_\nu \quad \text{and} \quad B_{\mu\nu} = \partial_\mu B_\nu - \partial_\nu B_\mu, \tag{2.20}$$

we can see the origin of the triple and quartic gauge boson couplings. These couplings occur in non-abelian gauge theories and are very important for the production of $W^\pm\gamma$ via VBF.

So far, we have not introduced any mass terms, but we know from experimental data that the fermions and three of the four electroweak bosons are massive. A classic QED mass term of the form $m(\overline{L}R + \overline{R}L)$ for fermions or a similar one for the gauge bosons would violate gauge invariance. In order to solve this problem, an additional scalar $SU(2)_L$ doublet was introduced by P. Higgs et al. [13]

$$\phi = \begin{pmatrix} \phi^+ \\ \phi^0 \end{pmatrix}. \tag{2.21}$$

It carries $Y_W = 1$ and its Lagrangian is

$$\mathcal{L}_{Higgs} = D_\mu\phi^\dagger D_\mu\phi \underbrace{-\mu^2\phi^\dagger\phi + \lambda(\phi^\dagger\phi)^2}_{V(\phi)}. \tag{2.22}$$

For the choice $\mu^2, \lambda > 0$, the Higgs potential $V(\phi)$ takes on the typical Mexican hat shape with a minimum for

$$|\phi_0| = \left(\frac{\mu^2}{2\lambda}\right)^{\frac{1}{2}} \equiv \frac{v}{\sqrt{2}}. \tag{2.23}$$

The ground state is usually chosen to be

$$\phi_0 = \frac{1}{\sqrt{2}}\begin{pmatrix} 0 \\ v \end{pmatrix}, \tag{2.24}$$

which is invariant under $U(1)$ but not under $SU(2)$ transformations anymore. Thus, the symmetry of the ground state is broken down from $SU(2)_L \times U(1)_{Y_W}$ to $U(1)_{em}$, where em indicates the electromagnetic interaction. One can now expand the Higgs field around the ground state

$$\phi = \frac{1}{\sqrt{2}}\begin{pmatrix} 0 \\ v + H(x) \end{pmatrix}, \tag{2.25}$$

where $H(x)$ describes a scalar boson, which is known as the Higgs boson. Here, we chose the unitary gauge to remove the Goldstone fields that would actually appear in equation (2.25). After the symmetry breaking, the Lagrangian of the Higgs field becomes

$$\begin{aligned} \mathcal{L}_{Higgs} = {} & \frac{1}{2}(\partial_\mu H)^2 - \frac{1}{2}m_H^2 H^2 - \lambda v H^3 - \frac{1}{4}\lambda H^4 \\ & + \left[m_W^2 W_\mu^+ W^{-\mu} + \frac{1}{2}m_Z^2 Z_\mu Z^\mu\right]\left(1 + \frac{H}{v}\right)^2, \\ \text{with} \quad & m_W^2 = \left(\frac{gv}{2}\right)^2, \quad m_Z^2 = \left(\frac{g^2 + g'^2}{2}v\right)^2, \quad m_H^2 = 2\lambda v^2. \end{aligned} \tag{2.26}$$

The Higgs field H obtains a mass term that makes it a massive boson. The Higgs boson couples to itself and to the three new massive bosons that arise, namely the $W^{\pm}$ bosons, which are defined as

$$W_{\mu}^{\pm} = \frac{1}{\sqrt{2}} \left(W_{\mu}^{1} \mp i W_{\mu}^{2} \right), \tag{2.27}$$

and the Z boson, which is a linear combination of the two remaining fields

$$\begin{pmatrix} Z_{\mu} \\ A_{\mu} \end{pmatrix} = \begin{pmatrix} \cos\theta_W & -\sin\theta_W \\ \sin\theta_W & \cos\theta_W \end{pmatrix} \begin{pmatrix} W_{\mu}^{3} \\ B_{\mu} \end{pmatrix}. \tag{2.28}$$

A_{μ} denotes the field of the massless photon, which is the gauge boson of the unbroken $U(1)_{em}$ group. The Weinberg or weak mixing angle θ_W is defined by

$$\cos\theta_W = \frac{g}{\sqrt{g^2 + g'^2}} \quad \text{and} \quad \sin\theta_W = \frac{g'}{\sqrt{g^2 + g'^2}}. \tag{2.29}$$

After the introduction of the scalar field ϕ, fermion mass terms for leptons and quarks can be added in the form

$$\mathcal{L}_{m_l} = -\sum_{i,j} \lambda_{ij}^{l} \overline{L}_{i}^{l} \phi R_{j}^{l} + h.c. \qquad \mathcal{L}_{m_q} = -\sum_{i,j} \lambda_{ij}^{d} \overline{L}_{i}^{q} \phi R_{j}^{d} - \sum_{i,j} \lambda_{ij}^{u} \epsilon^{ab} \overline{L}_{i,a}^{q} \phi_{b}^{\dagger} R_{j}^{u} + h.c. \tag{2.30}$$

The indices i and j run over the different generations and ϵ^{ab} denotes the two dimensional epsilon tensor. These terms are invariant under $SU(2)_L \times U(1)_{Y_W}$. The complex mass matrices λ_{ij}^{x} can be diagonalized using the unitary transformations

$$L_{i}^{u} = U_{ij}^{u} L'^{u}_{j}, \qquad L_{i}^{d} = U_{ij}^{d} L'^{d}_{j}, \qquad \text{etc.} \tag{2.31}$$

These transformation also affect the W boson current

$$J_{W}^{\mu +} = \frac{1}{\sqrt{2}} \overline{L}_{i}^{u} \gamma^{\mu} L_{i}^{d} = \frac{1}{\sqrt{2}} \overline{L'}^{u}_{i} \gamma^{\mu} (\underbrace{U^{u\dagger} U^{d}}_{V_{CKM}})_{ij} L'^{d}_{i}. \tag{2.32}$$

The unitary matrix V_{CKM} is the Cabbibo-Kobayashi-Maskawa matrix. Its off-diagonal elements allow transitions between different quark generations mediated by W bosons. These off-diagonal elements are small and we will show in section 3.2.4 that we can neglect these quark mixing effects in $W^{\pm}\gamma$ production via VBF.

The coupling of the photon is described by $\alpha_{em} \equiv e^2/4\pi$. As explained in section 2.1.1, the strength of the coupling is not fixed but depends on the present energy scale. Therefore, it is called running coupling 'constant'. For QED, it is at the one loop level given by

$$\alpha_{em}(Q^2) = \frac{\alpha_{em}(\mu^2)}{1 - \frac{\alpha_{em}(\mu^2)}{3\pi} \ln\left(\frac{Q^2}{\mu^2}\right)}. \tag{2.33}$$

This means that the coupling becomes stronger, the higher the energy scale and thus, the shorter the distance is. A good reference scale for $W^{\pm}\gamma$ production via VBF is the W boson mass m_W. At this scale, the electromagnetic coupling is

$$\alpha_{em}(m_W^2) = \alpha_{em}(80.4^2 \text{ GeV}^2) \approx 0.00778. \tag{2.34}$$

2.2.2. Quantum chromodynamics

The strong interaction is described by a $SU(3)_c$ symmetry group. Its Lagrangian reads

$$\mathcal{L} = \underbrace{-\frac{1}{4} G^a_{\mu\nu} G^{a\mu\nu}}_{\mathcal{L}_{gauge}} + \underbrace{\sum_q \bar{q}_i \left(i(\not{D})_{ij} - m_q \delta_{ij} \right)_{ij} q_j}_{\mathcal{L}_{ferm}} + \underbrace{\frac{1}{2\xi_0} \left(\partial_\mu A^\mu\right)^2}_{\mathcal{L}_{fix}} \underbrace{-c^{a*} \partial^\mu D^{ac}_\mu c^c}_{\mathcal{L}_{ghost}}. \tag{2.35}$$

$G^a_{\mu\nu}$ denotes the gluon field strength tensor

$$G^a_{\mu\nu} = \partial_\mu G^a_\nu - \partial_\nu G^a_\mu + g f^{abc} G^b_\mu G^c_\nu, \tag{2.36}$$

where G^a_ν is the gluon field, g the coupling and f^{abc} the structure constant. The non-abelian gauge group leads again to gauge boson self interactions. The covariant derivative is given by

$$(D_\mu)_{ij} = \delta_{ij} \partial_\mu + i g T^a_{ij} G^a_\mu, \tag{2.37}$$

where T^a_{ij} are the generators of the $SU(3)_c$ symmetry group. The sum over q in $\mathcal{L}_{ferm}$ runs over the different quark flavors. The gauge fixing term $\mathcal{L}_{fix}$ is chosen according to the Feynman 't Hooft gauge. The last term, $\mathcal{L}_{ghost}$, contains the so-called ghost fields denoted by c. These are scalar, anticommutative fields that are needed to remove two unphysical degrees of freedom in the Lagrangian.

The running of the strong coupling $\alpha_S \equiv g^2/(4\pi)$ at the one loop level is described by

$$\alpha_S(Q^2) = \frac{\alpha_S(\mu^2)}{1 + \frac{\alpha_S(\mu^2)}{12\pi}(33 - 2n_f) \ln\left(\frac{Q^2}{\mu^2}\right)}. \tag{2.38}$$

n_f denotes the number of quark flavors, which is 6 in the Standard Model. This leads to two interesting phenomena

- For $Q^2 \to \infty$, the coupling $\alpha_S(Q^2)$ goes to zero, which means that for large energies quarks and gluons interact almost as free particles. This phenomenon is called asymptotic freedom and was discovered by Politzer, Wilczek and Gross [14, 15].
- In the other limit, $Q^2 \to 0$, we see the exactly opposite behavior, the coupling goes to infinity. This means that one would need all the energy of the universe to separate two quarks and thus quarks are always bound in hadrons. This is called confinement. The scale, at which $\alpha_S(Q^2)$ becomes infinite, is called Λ_{QCD} and was experimentally determined to be $\Lambda_{QCD} \approx 200$ MeV, e.g. [16].

In our NLO QCD calculation, we use the running coupling constant at the two loop level, which is given by

$$\alpha_S(Q^2) = \frac{4\pi}{\beta_0 \ln(Q^2/\Lambda^2_{QCD})} \left[1 - \frac{2\beta_1}{\beta_0^2} \frac{\ln[\ln(Q^2/\Lambda^2_{QCD})]}{\ln(Q^2/\Lambda^2_{QCD})} \right], \tag{2.39}$$

with $\beta_0 = 11 - 2/3 n_f$ and $\beta_1 = 51 - 19/3 n_f$.

At our reference scale of the W mass, m_W, the strong coupling is

$$\alpha_S(m_W^2) \approx 0.120. \tag{2.40}$$

$\alpha_S(m_W^2)$ is approximately 15 times larger than $\alpha_{em}(m_W^2)$, which is the reason why we calculate the NLO QCD corrections and neglect the NLO EW corrections.

2.2.3. Ward identities

Ward identities are general relations between Green's functions. Their existence is a direct consequence of gauge symmetry. For the sake of simplicity, the QED Ward identities will be explained here.
The total QED Lagrangian, $\mathcal{L}_{tot}$, reads

$$\begin{aligned}&\mathcal{L}_{tot} = \mathcal{L}_{gauge} + \mathcal{L}_{fix} + \mathcal{L}_{ferm} + J^\mu(x)A_\mu(x) + J_\Psi(x)\Psi(x) - \bar{\Psi}(x)J_{\bar{\Psi}}(x) \quad \text{with}\\ &\mathcal{L}_{gauge} = -\frac{1}{4}F^{\mu\nu}F_{\mu\nu}, \quad \mathcal{L}_{fix} = \frac{1}{2\xi}\left[\partial^\mu A_\mu\right]^2, \quad \mathcal{L}_{ferm} = \bar{\Psi}(x)\left[i\gamma^\mu(\partial_\mu - ieA_\mu) - m\right]\Psi(x).\end{aligned} \tag{2.41}$$

Here, $\mathcal{L}_{gauge}$ is the Lagrangian of the gauge field, $\mathcal{L}_{fix}$ is the gauge fixing term and $\mathcal{L}_{ferm}$ is the Lagrangian for the fermions. $J^\mu, J_\Psi, J_{\bar{\Psi}}$ are the sources that generate and annihilate the respective particles.

The generating functional for the Green's functions is constructed as

$$Z[J, J_\Psi, J_{\bar{\Psi}}] = \int e^{i\int \mathcal{L}_{tot}dx} dA d\bar{\Psi} d\Psi. \tag{2.42}$$

This functional can be used to determine the Green's function by

$$\frac{\delta T_c}{\delta J_a(x)\delta J_b(y)}\Big|_{J=0} = G_c^{ab}(x,y) \quad \text{with} \quad T[J] = e^{iT_c} \quad \text{and} \quad T = \frac{Z[J]}{Z[0]}. \tag{2.43}$$

Here, T is the normalized generating functional and T_c is a modified version of T that contains only the connected parts. $G_c^{ab}(x,y)$ is the two-point Green's function for a particle a generated at x becoming particle b and getting annihilated at y. It contains all possible diagrams in all orders of perturbation theory.

Using an infinitesimal gauge transformation of the generating functional Z in equation (2.42) and the principle of equation (2.43), one can derive the Ward identity

$$-k^\mu G^{AA_i\Psi\bar{\Psi}}_{C\mu\mu_i}(k, k_i, p_j, q_j) = e\sum_l \left[G^{A_i\Psi\bar{\Psi}}_{C\mu_i}(k_i, p_j + \delta_{jl}k, q_j) - G^{A_i\Psi\bar{\Psi}}_{C\mu_i}(k_i, p_j, q_j + \delta_{jl}k)\right]. \tag{2.44}$$

$G^{AA_i\Psi\bar{\Psi}}_{C\mu\mu_i}(k, k_i, p_j, q_j)$ denotes Green's function for n photon fields A_i with momenta k_i, m fermion and anti-fermion fields Ψ and $\bar{\Psi}$ with their respective momenta p_j and q_j and the external photon field A, that will be replaced with its momentum k. To illustrate this, figure 2.3 shows a diagrammatic version of equation (2.44).

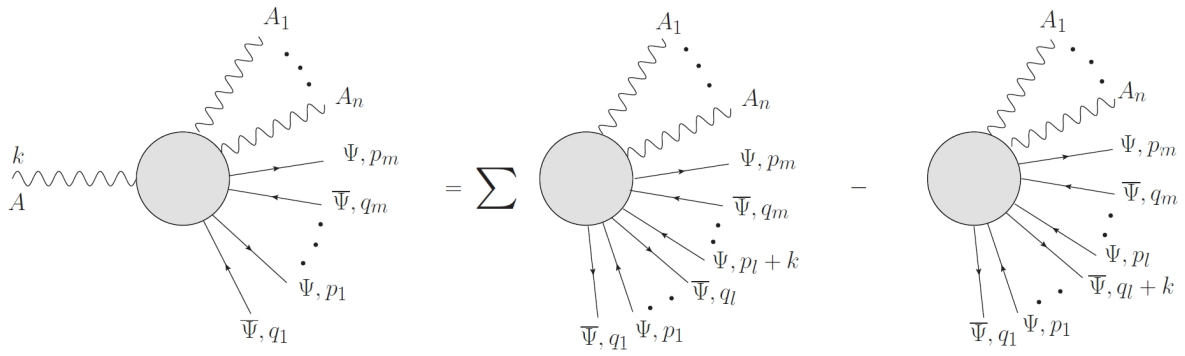

Figure 2.3: The diagrammatic illustration of the Ward identity shows an arbitrary QED Green's function with at least one external photon field A. If the photon is replaced by its momentum, the Green's function will decompose into the difference of two topologies without the replaced photon.

Figure 2.3 and equation (2.44) show that a Green's function for an arbitrary number of fermion-anti-fermion pairs and at least one photon decomposes into a sum over the difference of the two next simpler Green's functions without this photon, if the photon is replaced by its momentum. This is the Ward identity, which will be used to control the numerical stability of the virtual corrections in section 3.6.1.
After truncating all the external lines in figure 2.3 and setting all the momenta on-shell, equation (2.44) can be written as

$$- k^{\mu} G_{c\,\mu}^{\underline{A}\,\underline{A_i}\,\Psi\,\bar{\Psi}}\big|_{k_i^2=0,\, p_j^2=m^2,\, q_j^2=m^2} = 0. \tag{2.45}$$

The underlined fields, e.g. $\underline{A_i}$, symbolize the truncated fields. Equation (2.45) is also valid for matrix elements. So the amplitude will vanish if the photon is replaced by its momentum. This is also referred to as 'gauge invariance' and will be used for several gauge tests in section 4.4.

2.3. Effective field theory

An effective field theory (EFT) is an approximation of a more general theory including the relevant symmetries and degrees of freedom. It is often used to describe physics at an energy E, which is much lower than the energy scale Λ, at which the details of a more general theory have to be taken into account. The EFT averages out the microscopic effects of a higher theory that are negligible at much lower energies.
EFTs are often used to parametrize the effects of new physics originating from an unknown theory at an energy scale much higher than the one that is experimentally accessible. For this purpose, it is not necessary to know the exact behavior of the 'correct' theory at a much higher energy. The Lagrangian of an effective field theory comprises operators that respect the symmetries and degrees of freedom of the known theory at the experimentally accessible energy

$$\mathcal{L}_{EFT} = \sum_d \sum_i \frac{f_i^{(d)}}{\Lambda^{d-4}} \mathcal{O}_i^{(d)}. \tag{2.46}$$

Here, d denotes the energy dimension and i runs over all possible operators of fixed dimension. The dimension of the Lagrangian is 4 because the action S is dimensionless and $S = \int d^4x \mathcal{L}$. Therefore, an operator with dimension d must be divided by the appropriate power of the

energy scale Λ^{d-4} so that the coupling constants $f_i^{(d)}$ are dimensionless. Note that theories containing operators with $d > 4$ are not renormalizable any more (e.g. [9]).
Although the sum over the dimensions in equation (2.46) can go up to infinity, we only need to take a limited number of operators into account. The reason for this is that the energy E reached in the experiment is usually much lower than the scale Λ, up to which the EFT is valid. This leads to a suppression of the operators $\mathcal{O}_i^{(d)}$ by $(E/\Lambda)^d$.

2.3.1. Fermi's theory of β-decay

The best known example of an EFT is Fermi's interaction [17]. This theory was developed by Enrico Fermi to describe the β-decay of the neutron via the interaction of four fermions in one vertex as depicted in figure 2.4.

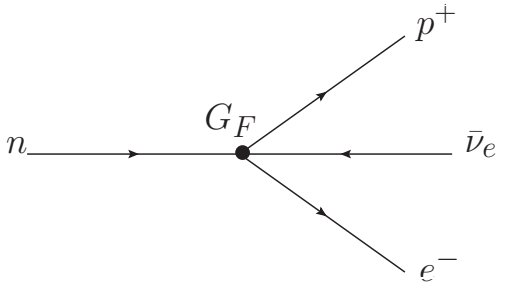

Figure 2.4: The neutron decays via the four fermion vertex in Fermi's theory.

When Fermi set up a phenomenological Lagrangian for this, he did not know the exact structure of the couplings. By now, we know that the couplings of the weak interaction have a vector minus axial vector structure. Taking this into account, we can write down the Lagrangian for Fermi's interaction

$$\mathcal{L} = -\frac{G_F}{\sqrt{2}}\bar{p}\gamma^\alpha(1-\gamma_5)n\bar{e}\gamma_\alpha(1-\gamma^5)\nu_e. \tag{2.47}$$

The fermion fields are denoted with n, p^+, e^- and $\bar{\nu}_e$ and G_F is Fermi's constant. It's value has been determined experimentally

$$G_F = 1.16637(1)\cdot 10^{-5}\ \text{GeV}^{-2}. \tag{2.48}$$

We can express the Lagrangian in equation (2.47) in terms of the general structure of an EFT as in equation (2.46)

$$\mathcal{L}_F = \frac{f_F}{\Lambda^2}\mathcal{O}_F \quad \text{with} \quad \frac{f_F}{\Lambda^2} = \frac{G_F}{\sqrt{2}}, \quad \mathcal{O}_F = \bar{p}\gamma^\alpha(1-\gamma_5)n\bar{e}\gamma_\alpha(1-\gamma^5)\nu_e. \tag{2.49}$$

A general problem of EFTs is that the cross section rises with the center of mass energy. This leads to violation of the unitarity of the S-matrix above a certain scale.

At and above that scale, a more general theory is needed to solve this problem. In our case, this is the GWS-theory, which was introduced in 2.2.1. In the GWS theory the massive W-bosons mediate the beta decay as depicted in figure 2.5.

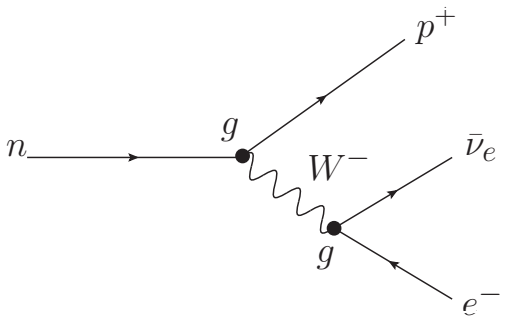

Figure 2.5: In the GWS theory the beta decay is mediated by the W boson.

This interaction can be described by

$$\mathcal{O} = \frac{g^2}{8}\bar{p}\gamma^\alpha(1-\gamma_5)n\frac{1}{q^2-m_W^2}\bar{e}\gamma_\alpha(1-\gamma^5)\nu_e. \tag{2.50}$$

Now, the propagator of the massive W boson prevents the cross section from rising with the CMS energy $s = q^2$ and thus from violating unitarity. Fermi's interaction can be interpreted as the low energy limit of the GWS theory since

$$\frac{1}{q^2-m_W^2} \approx -\frac{1}{m_W^2} \quad \text{for} \quad q^2 \ll m_W^2, \tag{2.51}$$

which leads to

$$\frac{G_F}{\sqrt{2}} = \frac{g^2}{8m_W^2}. \tag{2.52}$$

When we compare this to the EFT parametrization of Fermi's interaction in equation (2.49), we can see that the scale for new physics is $\Lambda = m_W$ and the coupling constant $f_F = g^2/8$.

2.4. Anomalous couplings

In VBFNLO, an EFT is used to parametrize the effects of anomalous couplings of weak gauge bosons beyond the SM. The basic idea is to assume that the Standard Model is the first term of this field theory, which is written as a series in $1/\Lambda$. For each power $1/\Lambda^n$, we can construct operators with the corresponding dimension that respect the $SU(2)_L \times U(1)_{Y_W}$ gauge symmetry and Lorentz invariance. There are only operators with even energy dimension as odd dimensions would violate gauge or Lorentz invariance. We want to modify only weak boson self and weak boson Higgs couplings since couplings between fermions and weak bosons are already strongly constrained [18]. Since high powers of $1/\Lambda^n$ are strongly suppressed, we introduce only dimension 6 and 8 operators denoted by $\mathcal{O}_i$ and $\mathcal{L}_j$, respectively. The Lagrangian of our EFT has the structure

$$\mathcal{L}_{EFT} = \mathcal{L}_{SM} + \sum_i \frac{f_i}{\Lambda^2}\mathcal{O}_i + \sum_j \frac{f_j}{\Lambda^4}\mathcal{L}_j. \tag{2.53}$$

For the construction of the operators, the following building blocks are available

$$\hat{W}_{\mu\nu} = i\frac{g}{2}W^a_{\mu\nu}\sigma^a\,, \tag{2.54a}$$

$$\hat{B}_{\mu\nu} = i\frac{g'}{2}B_{\mu\nu}\,, \tag{2.54b}$$

$$D_\mu = \partial_\mu + igW^a_\mu\frac{\sigma^a}{2} + i\frac{g'}{2}B_\mu\,, \tag{2.54c}$$

$$\Phi = \frac{1}{\sqrt{2}}\begin{pmatrix} 0 \\ v+H \end{pmatrix}\,, \tag{2.54d}$$

where $W^a_{\mu\nu}$ and $B_{\mu\nu}$ are the field strength tensors that were introduced in section 2.2.1. All operators should form gauge invariant quantities.

Here, just a few operators will be explained explicitly. A full list of all possible dimension 8 operators can be found in appendix A. In case of the dimension 6 operators, we must distinguish between $\mathcal{CP}$-even and $\mathcal{CP}$-odd operators. Two examples for $\mathcal{CP}$ even dimension 6 operators are

$$\mathcal{O}_{WW} = \Phi^\dagger\hat{W}_{\mu\nu}\hat{W}^{\mu\nu}\Phi, \tag{2.55a}$$

$$\mathcal{O}_{BB} = \Phi^\dagger\hat{B}_{\mu\nu}\hat{B}^{\mu\nu}\Phi. \tag{2.55b}$$

$\mathcal{O}_{WW}$ modifies the HW^+W^- coupling and both operators affect the HZZ coupling. In addition, both operators give rise to $HZ\gamma$ and $H\gamma\gamma$ couplings that do not exist in the Standard Model. In order to construct $\mathcal{CP}$-odd dimension 6 operators, we need the dual field strength tensors

$$\hat{W}_{\mu\nu} \to \hat{\widetilde{W}}_{\mu\nu} = \frac{1}{2}\epsilon_{\mu\nu\rho\sigma}\hat{W}^{\rho\sigma}, \tag{2.56a}$$

$$\hat{B}_{\mu\nu} \to \hat{\widetilde{B}}_{\mu\nu} = \frac{1}{2}\epsilon_{\mu\nu\rho\sigma}\hat{B}^{\rho\sigma}. \tag{2.56b}$$

The $\mathcal{CP}$-odd operators that correspond to the ones above are

$$\mathcal{O}_{\widetilde{W}W} = \Phi^\dagger\hat{\widetilde{W}}_{\mu\nu}\hat{W}^{\mu\nu}\Phi, \tag{2.57a}$$

$$\mathcal{O}_{\widetilde{B}B} = \Phi^\dagger\hat{\widetilde{B}}_{\mu\nu}\hat{B}^{\mu\nu}\Phi. \tag{2.57b}$$

They affect the same couplings as the corresponding $\mathcal{CP}$-even operators.

As pointed out earlier, the focus of this work lies on dimension 8 operators for two reasons. Firstly, dimension 6 operators occur already in QCD diboson production like e.g. $pp \to W^\pm\gamma$. Diboson processes have significantly larger cross section than the corresponding VBF processes and thus are much more sensitive to anomalous couplings. Secondly, the dimension 6 operators are already strongly constrained by experimental data [6]. The parametrization of the dimension 8 operators follows Ref. [19]. They can be divided into three categories

- Operators that contain only $D_\mu\phi$, e.g.

$$\mathcal{L}_{S,0} = \left[(D_\mu\phi)^\dagger(D_\nu\phi)\right] \times \left[(D^\mu\phi)^\dagger(D^\nu\phi)\right]. \tag{2.58}$$

- Operators that contain $D_\mu\phi$ and field strength tensors ($\hat{W}_{\mu\nu}$, $\hat{B}_{\mu\nu}$), e.g.

$$\mathcal{L}_{M,0} = \mathrm{Tr}\left[\hat{W}_{\mu\nu}\hat{W}^{\mu\nu}\right] \times \left[(D_\beta\phi)^\dagger(D^\beta\phi)\right], \tag{2.59a}$$

$$\mathcal{L}_{M,5} = \left[(D_\mu\phi)^\dagger\hat{W}_{\beta\nu}(D^\nu\phi)\right] \times \hat{B}^{\beta\mu}. \tag{2.59b}$$

- Operators that contain only field strength tensors ($\hat{W}_{\mu\nu}$, $\hat{B}_{\mu\nu}$), e.g.

$$\mathcal{L}_{T,0} = \mathrm{Tr}\left[\hat{W}_{\mu\nu}\hat{W}^{\mu\nu}\right] \times \mathrm{Tr}\left[\hat{W}_{\alpha\beta}\hat{W}^{\alpha\beta}\right], \tag{2.60a}$$

$$\mathcal{L}_{T,5} = \mathrm{Tr}\left[\hat{W}_{\mu\nu}\hat{W}^{\mu\nu}\right] \times \hat{B}_{\alpha\beta}\hat{B}^{\alpha\beta}. \tag{2.60b}$$

The last category of operators is the one with the largest influence on the $WW\gamma\gamma$ and $WWZ\gamma$ couplings that occur in $W^{\pm}\gamma$ production via VBF.

2.4.1. Form factor

Analogously to the violation of unitarity in Fermi's interaction in section 2.3.1, the EFT describing anomalous couplings will violate unitarity above a certain scale. The reason for this is that for high energies the assumption $E \ll \Lambda$ is not valid any more. This can happen when the available energy in the gauge boson scattering process reaches several TeV, which is already possible in the 7 and 8 TeV runs of the LHC. We can see the unitarity violating behavior in the $d\sigma/dp_T^{\gamma}$ and $d\sigma/dm_T^{W\gamma}$ distributions in figure 2.6[1].

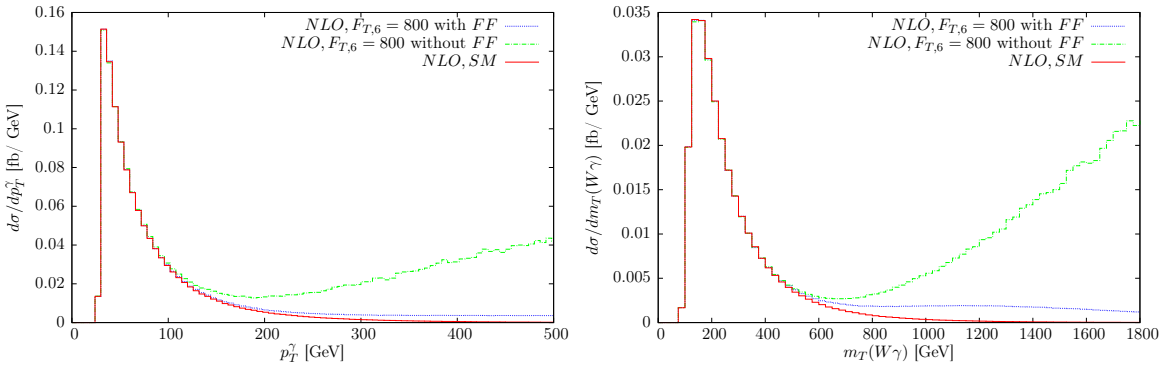

Figure 2.6: The $d\sigma/dp_T^{\gamma}$ and $d\sigma/dm_T^{W\gamma}$ distributions show a strong increase in the high energy region for anomalous couplings without form factor. When the form factor of equation (2.61) with $n = 2$ and $\Lambda_{FF} = 1700$ GeV is applied, this strong increase can be suppressed.

The steep increase of anomalous couplings effects in the high energy region leads to $|\mathcal{M}|^2 > 1$, which violates the unitarity of the S matrix. In this region, the terms with energy dimension higher than 8 that we neglected in equation (2.53) become important.

In order to avoid the violation of unitarity, we apply a form factor that suppresses the anomalous couplings effects in the high energy region. This form factor is given by

$$\mathcal{F}(s) = \frac{1}{\left(1 + \frac{s}{\Lambda_{FF}}\right)^n}, \tag{2.61}$$

where Λ_{FF} is the energy scale, at which one expects the unitarity violating behavior of the anomalous couplings. This scale is in general different for each operator. The exponent n is basically arbitrary but should be chosen not too big to avoid a too strong suppression but big enough to prevent the unitarity violation. For dimension 6 operators, we usually choose $n = 1$ and for dimension 8 operators $n = 2$. Figure 2.6 shows that the form factor prevents the unitarity violation while anomalous couplings effects are still observable.

[1] All plots in this thesis were created with GNUPLOT.

2.5. Proton-proton collider

The Large Hadron Collider (LHC) is the largest particle collider available at present. Bunches of protons are accelerated using electrical fields and forced on a circular path by magnetic fields. When the bunches reach the highly relativistic limit, they collide inside one of the detectors. These detectors allow us to observe the trajectories of the particles produced in the collision and thus to reconstruct the events.

Because the energies at the LHC are on the order of TeV, not the protons themselves, but their constituents, the partons, interact. The momentum that these partons carry is distributed statistically and described by the so-called parton distribution functions (PDF).

2.5.1. PDFs

The fraction of the proton momentum that a parton carries is denoted by the parameter x, which was introduced by R. Feynman. A parton distribution functions (PDF) gives the probability that a parton of a given flavor carries a specific momentum fraction x. The running of the strong coupling α_S leads to large values of the coupling at low energies. That way, sea quarks and gluons are continuously generated and annihilated alongside the valence quarks. Furthermore, this is the reason why the PDFs can not be calculated perturbatively, but have to be fitted to experimental data.
The PDFs depend on the energy scale Q^2 of the proton and have to be evolved to the present energy scale of the proton once they were fitted for a specific scale. To perform this evolution, the so-called DGLAP equations [20, 21, 22] are used.
A common interface to multiple PDF sets is LHAPDF [23]. Among others, it contains the CTEQ6m PDF, for which the relevant PDFs are shown in figure 2.7. The PDFs are dominated

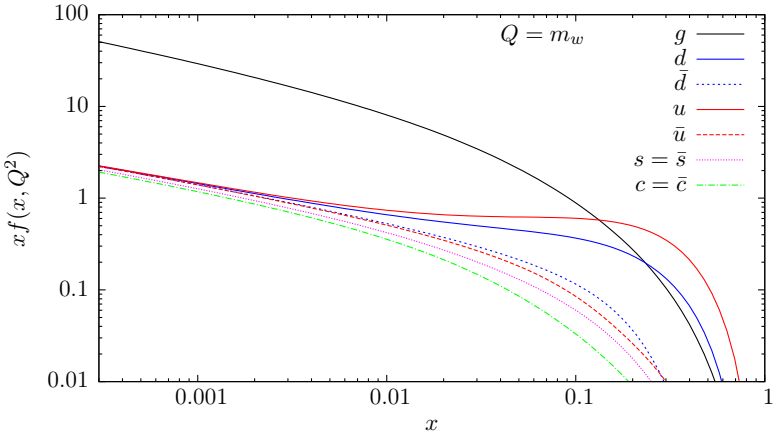

Figure 2.7: This plot shows the parton density functions of the CTEQ6m set for the relevant flavors. Note that the gluons dominate the region of small Feynman x values.

by up quarks for large Feynman x. Charm, strange and all anti-quarks, which are the sea quarks, carry only a little share of the proton momentum. For small values of Feynman x the PDFs are dominated by gluons. This can lead to large enhancements of diagrams with initial state gluons. The PDFs used in this work are the CTEQ6l1 [24] for LO and CT10 [25] for NLO calculations.

2.6. Event selection at colliders: Cuts

In general, cuts are used to simulate the experimental detector acceptance in a theoretical calculation. Moreover, they can be used to remove singularities or to increase the signal to background ratio by suppressing undesired contributions. It is convenient and conventional in collider physics to introduce several variables:

- The pseudo-rapidity of a particle is defined as

$$\eta = -\ln\left(\tan\frac{\theta}{2}\right), \tag{2.62}$$

  where θ is the angle between the particle and the beam axis. This transformation maps particles that are very close to the beam axis to very large, positive or negative pseudo-rapidities. These particles can hardly be detected and are therefore discarded. Moreover, the pseudo-rapidity can be expressed as

$$\eta = \frac{1}{2}\ln\frac{|\vec{p}| + p_L}{|\vec{p}| - p_L}, \tag{2.63}$$

  with the three dimensional momentum $\vec{p}$ and the longitudinal momentum p_L of the particle.

- Strongly related to the second definition of the pseudo-rapidity is the rapidity

$$y = \frac{1}{2}\ln\frac{E + p_L}{E - p_L}, \tag{2.64}$$

  where E is the energy of the particle. For massless particles, rapidity and pseudo-rapidity are identical.

- The R-separation is introduced to measure angular distances between two particles. It is defined as

$$\Delta R_{12} = \sqrt{(\eta_2 - \eta_1)^2 + (\phi_2 - \phi_1)^2}. \tag{2.65}$$

  ϕ_i is the azimuthal angle of particle i. Restricting this variable by imposing cuts has two purposes. In a theoretical calculation, it helps to avoid collinear singularities, e.g. if the photon is radiated off the lepton. Furthermore, the angular separation is necessary between jets and leptons or photons since the detector resolution in the experiment is limited.

The full list of cuts that were applied for the calculation of $W^{\pm}\gamma$ production in VBF can be found in table 5.2.

In addition, we need a technical cut to avoid singularities in our calculation. The photon propagator of the t-channel photon in figure 2.8 is proportional to $1/p_\gamma^2$, which can lead to singularities for $p_\gamma^2 \to 0$. For this reason, we apply a cutoff on the momentum squared of the photon $p_\gamma^2 > 4$ GeV^2. The phase space region that is removed by this cut is strongly suppressed by the vector boson fusion cuts.

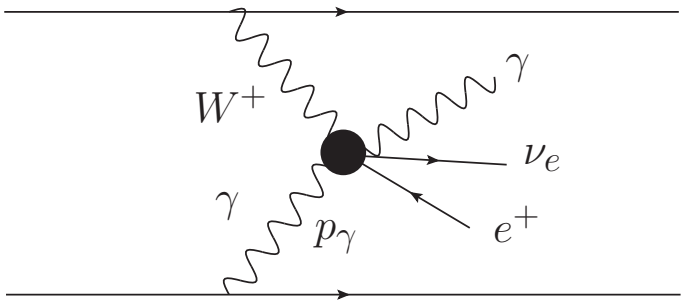

Figure 2.8: The photon in the t-channel can lead to singularities if its momentum squared p_γ^2 gets small.

2.6.1. Vector boson fusion cuts

For weak boson scattering and vector boson fusion processes, we apply the following cuts

$$y_{j_1} \cdot y_{j_2} < 0, \qquad |y_{j_1} - y_{j_2}| > 4, \qquad m_{j_1 j_2} > 600 \text{ GeV}. \tag{2.66}$$

j_1 and j_2 denote the jets with the highest and the second highest transverse momentum, $p_T^{j_i}$, respectively, or in other words, the two hardest jets. These two jets are called tagging jets since they are used to identify VBF events in the experiment. $y_{j_1} \cdot y_{j_2} < 0$ requires the tagging jets to be in opposite detector hemispheres. By imposing $|y_{j_1} - y_{j_2}| > 4$, we separate the rapidities of the tagging jets significantly. The cut on the invariant mass of the tagging jets $m_{j_1 j_2} > 600$ GeV leads to a large R-separation of the tagging jets. In summary, the VBF cuts require the tagging jets to be approximately back-to-back.

The VBF cuts are not only necessary for the event identification in the experiment. They also suppress s-channel contributions, which are not included in the calculation done in this thesis. Two example diagrams of s-channel contributions are shown in figure 2.9. In these diagrams, the two jets are produced in the decay of weak bosons.

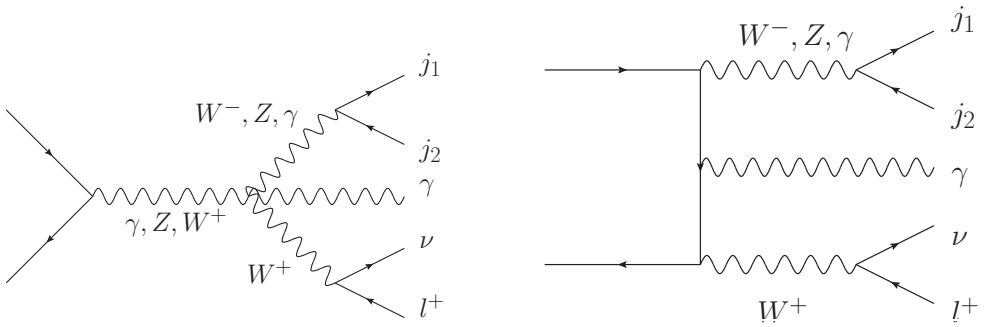

Figure 2.9: These Feynman diagrams show two s-channel contributions to $W^+\gamma$ production that occur at leading order.

Considering the masses of $m_W = 80.4$ GeV and $m_Z = 91.2$ GeV and the widths of $\Gamma_W = 2.1$ GeV and $\Gamma_Z = 2.5$ GeV of the dominating W and Z bosons, we see that these channels are almost completely removed by the $m_{j_1 j_2} > 600$ GeV cut.

At NLO QCD, a third jet can be created in addition to the two s-channel jets from figure 2.9. With this third jet, topologies such as the one in figure 2.10 are able to pass the VBF cuts in some cases. However, these topologies are not included in this calculation of $W^\pm\gamma$ production via VBF since they are considered to be part of the corresponding QCD triboson production processes in VBFNLO. In section 4.2, it will be explicitly shown that these contributions are small.

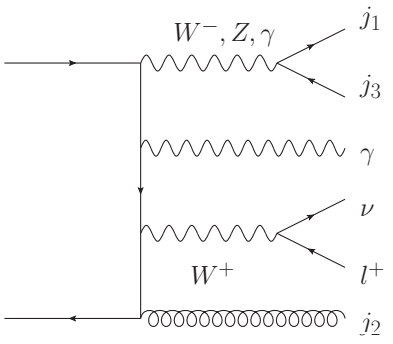

Figure 2.10: At NLO QCD the additional jet can lead to s-channel contributions passing the VBF cuts.

Furthermore, the VBF cuts suppress the dominant QCD $W^{\pm}\gamma jj$ production mode presented in figure 1.2, where the event and the radiation are characterized to be more central.

2.6.2. Frixione photon isolation

For processes with final state photons and jets, it is very important to isolate the photon properly from the partons. In scattering phenomena, photons can be produced either in the direct process or via photon fragmentation. Obviously, the photons produced by the latter method can lie inside of hadronic jets. This is a potential source of collinear singularities.
A straightforward approach to solving this problem is the so-called cone approach. One can calculate a cone around the photon axis and then impose that no parton can be found inside of that cone. The problem with this method is that it also cuts away soft gluons lying in the cone, which are needed to cancel infrared singularities. A proper solution to this problem was proposed by S. Frixione [26]. Here, the implementation of the formalism in VBFNLO is explained, which involves three steps:

1. For each parton, calculate angular distance between the photon and the parton i

$$R_{p_i\gamma} = \sqrt{(\eta_{p_i} - \eta_\gamma)^2 + (\phi_{p_i} - \phi_\gamma)^2}. \tag{2.67}$$

2. Reject event unless

$$\sum_i E_{T_{p_i}} \Theta(\delta - R_{p_i\gamma}) \leq \chi(\delta) \quad \forall \delta \leq \delta_0, \tag{2.68}$$

$$\text{with} \quad \chi(\delta) = \epsilon_\gamma E_{T\gamma} \left(\frac{1 - \cos\delta}{1 - \cos\delta_0} \right)^n, \tag{2.69}$$

   where $E_{T\gamma}$ is the transverse energy of the photon, ϵ_γ the efficiency of the cut and n some arbitrary exponent.

3. Apply jet finding algorithm and all remaining cuts.

In this way, soft gluons are allowed inside the cone while collinear singularities are avoided. We use $\epsilon_\gamma = 1$ and $n = 1$. This procedure is available in VBFNLO [8] and has to be applied for $W^{\pm}\gamma jj$ production at NLO QCD.

CHAPTER 3

IMPLEMENTATION

In the course of this diploma thesis, $W^{\pm}\gamma$ production via vector boson scattering was calculated at NLO QCD and implemented into the program VBFNLO [8]. After an introduction to the general structure of VBFNLO, the implementation of this process will be described in detail.

3.1. VBFNLO

VBFNLO is a parton level Monte-Carlo program, which was written to calculate vector boson fusion processes at next-to-leading order accuracy. By now it also contains QCD di- and triboson production processes as well as Higgs production via gluon fusion. It is written in FORTRAN and developed at the ITP [1] in the group of Dieter Zeppenfeld.

VBFNLO uses an adaptive Monte-Carlo approach to solve the phase space integral, which yields the cross section. In the following, the Monte-Carlo integration method will be explained.

3.1.1. Numerical integration

In order to calculate the cross section of a process $pp \to X$, the following integral has to be solved [27]

$$\sigma = \int dx_1 dx_2 \sum_{\substack{sub- \\ processes}} f_{a_1/p_1}(x_1) f_{a_2/p_2}(x_2) \frac{1}{2\hat{s}} \int d\Phi_{2\to n} \Theta(cuts) \overline{\sum_{\substack{spin, \\ color}}} |\mathcal{M}|^2 (a_1 a_2 \to f_1 \dots f_n). \tag{3.1}$$

Here, $f_{a/p}(x)$ is the parton distribution function (PDF), x_i is the Feynman x, $\sqrt{\hat{s}}$ is the available center of mass energy in the partonic subprocess and $d\Phi_{2\to n}$ is the Lorentz invariant phase space element. In general, one uses cuts to restrict the phase space in order to take experimental constraints into account or to avoid singularities in the calculation of the integral. This is represented by $\Theta(cuts)$. The remaining part $|\mathcal{M}|^2 (a_1 a_2 \to f_1 \dots f_2)$ stands for

[1] Institute for Theoretical Physics, Karlsruhe Institute of Technology

the transition matrix element, which corresponds to one subprocess. It has to be summed over the colors and polarizations of all outgoing particles and averaged over those quantum numbers of all incoming particles.
It is not possible to evaluate the integral of equation (3.1) analytically since the PDFs are only known numerically. Furthermore, it is not trivial to evaluate the phase space integral analytically. The complexity rises with the number of external legs, which also rises the dimension of the integral. Including the two x integrations, there are 12 non-trivial integrations, that have to be solved for the calculation of $pp \to l^{\pm}\overset{(-)}{\nu}\gamma jj$ at leading order. For the numerical integration it is convenient to map the phase space onto a d-dimensional unit cube $V = [0,1]^d$.

For the sake of simplicity and without loosing generality, the integral will be written in the following form

$$I = \int_{V=[0,1]^d} f(\vec{x}) d^d x. \tag{3.2}$$

The Monte-Carlo program now randomly chooses points $\vec{x}_i$ in the hyper cube and evaluates the integrand $f(\vec{x}_i)$ in those points. In a simple Monte-Carlo program, those random numbers are uniformly distributed and the Monte-Carlo approximation of the integral is

$$I_{MC} = \frac{1}{N} \sum_{i=1}^{N} f(\vec{x}_i). \tag{3.3}$$

According to the law of large numbers, the approximate value I_{MC} converges towards the exact value I

$$\lim_{N\to\infty} I_{MC} = I. \tag{3.4}$$

The variance of the integrand σ_f^2 is defined as

$$\sigma_f^2 = \frac{1}{N-1} \sum_{i=1}^{N} \left(f(\vec{x}_i) - I_{MC}\right)^2. \tag{3.5}$$

This can be used to estimate the variance of the Monte-Carlo result

$$\sigma_{I_{MC}}^2 = \frac{1}{N^2} \sum_{i=1}^{N} \sigma_f^2 = \frac{\sigma_N^2}{N}. \tag{3.6}$$

This means that the error of I_{MC}, $\delta I_{MC} \approx \sqrt{\sigma_{I_{MC}}^2}$, scales as $1/\sqrt{N}$ and is independent of the hyper cube dimension. This is another point in favor of the usage of Monte-Carlo integration for higher dimensional problems.

3.1.2. Importance sampling

Importance sampling is a technique to improve the convergence of the Monte-Carlo integration. The basic idea is to sample more points in the hyper space regions where the integrand is large and vice versa. This is done by modeling a probability distribution $P(\vec{x})$ that approximates $f(\vec{x})$ as good as possible. With this, the integral can be transformed into

$$\int f(\vec{x}) d^d x = \int \frac{f(\vec{x})}{p(\vec{x})} dP(\vec{x}) \quad \text{with} \quad dP(\vec{x}) = p(\vec{x}) d^d x. \tag{3.7}$$

Here $p(\vec{x})$ is the probability density of $P(\vec{x})$. The Monte-Carlo approximation of the integral in equation (3.7) is now

$$I_{MC} = \frac{1}{N} \sum_{i=1}^{N} \frac{f(\vec{x}_i)}{p(\vec{x}_i)}, \tag{3.8}$$

with the points $\vec{x}_i$ chosen according to the probability distribution $P(\vec{x})$. With this improvement, the statistical error of the Monte-Carlo result is

$$\frac{1}{\sqrt{N}} \sigma \left(\frac{f}{p} \right), \tag{3.9}$$

which can be significantly reduced for good choices of $p(\vec{x})$.

VBFNLO uses a modified version of the VEGAS algorithm [28], which is an adaptive Monte-Carlo algorithm that does importance sampling over several iterations. In the first iteration, it starts with a constant probability density and divides up the phase space into a plane grid. After each iteration, the borders within the grid are moved such that the individual segments give the same contribution to the integral. Thus the algorithm puts many points in regions where the integrand is large and vice versa. The advantage of this kind of importance sampling is that the probability distribution does not need to be known but will be constructed by VEGAS.

In addition to the importance sampling done by VEGAS, we also use manual importance sampling in VBFNLO. We know where some of the resonances of the matrix element $|\mathcal{M}|^2$ in equation (3.1) lie, since the decay of massive vector bosons follows a Breit-Wigner distribution. This knowledge can be used to improve the phase space generator. This will be explained in detail in section 3.3.

3.1.3. Program architecture

In this subsection, the general program architecture of VBFNLO will be explained. VBFNLO is written in FORTRAN and has a modular structure, which is very useful e.g. for the implementation of theories that modify the gauge boson couplings. The input data for the process is read from the file **vbfnlo.dat**. The cuts can be set in **cuts.dat**. Those parameters are read in at the very beginning of the program by the main routine, which is stored in **vbfnlo_main.F**. Then all the parameters for the phase space, the PDFs, the couplings, the histograms and the random number generator are initialized. The main operations for the calculation of a leading order cross section are done in three loops. The outer loop is over the iterations, which optimize the grid as described in section 3.1.2. The middle one loops over the different phase space channels that will be described in section 3.3 for $W^{\pm}\gamma jj$ production. The inner loop goes through the individual phase space points sampled by the integration routine. For each point, the following steps are done:

1. The integration routines yields an array of random numbers and the weight of this point in the hypercube. The weight is determined by the importance sampling.
2. The routine *phasespace* converts the random numbers into the momenta of the external particles (section 3.3).
3. In the routine *cuts*, it is checked whether the phase space point is within the cuts specified in **cuts.dat**. If the point does not pass the cuts, the rest of the code will be skipped and a new point will be sampled.

4. The routine *scales* calculates factorization and renormalization scales, which can in general depend on the phase space point.
5. Now the function *amplitude* is called. The calculation of the transition matrix element $|\mathcal{M}|^2$ takes place here and will be described in detail in section 3.2.1.
6. Finally, the matrix element $|\mathcal{M}|^2$ is multiplied by the phase space factor and returned to the integration routine.

In the last iteration, the events are passed to the histogram routine. Within this routine, one can easily add custom one and two dimensional histograms. All the histograms presented in this diploma thesis were calculated with this routine. Furthermore, it is possible to write the LO events to a file as Les-Houches-Accord [29] or HepMC [30] events.

The integration routine sums up all the contributions from the individual phase space points. At the end of each iteration, the Monte-Carlo result and the corresponding error estimate are returned.

In the following, the description of the leading order calculation of $W\gamma$ production via VBF is given.

3.2. Leading order calculation

The function *amplitude* called by the main routine is only an interface for all the processes in VBFNLO. For $W^{\pm}\gamma jj$ via VBF, *amplitude* calls the function *m2s_wbfw*. This function has two main purposes. First, it calculates the leptonic tensors, the polarization vector of the photon and the off-shell current of the W boson. Furthermore, it calculates the values of the PDFs for the given scale and Feynman x values. How this works will be explained in detail in sections 3.2.1 - 3.2.3.
Then, it calls a routine named *wbf_w2j* with every possible combination of particles and anti-particles for the four external quarks. This routine now finally calls the routines *qqwpaqq* or *qqwmaqq* where the matrix elements for $W^+\gamma jj$ or $W^-\gamma jj$ are calculated, respectively.

The matrix elements are only calculated for four specific flavor combinations:

$W^+\gamma jj$	$W^-\gamma jj$
$u\ c \to u\ s\ l^+\ \nu\ \gamma$	$d\ c \to u\ c\ l^-\ \bar{\nu}\ \gamma$
$d\ c \to d\ s\ l^+\ \nu\ \gamma$	$d\ s \to u\ s\ l^-\ \bar{\nu}\ \gamma$
$u\ c \to d\ c\ l^+\ \nu\ \gamma$	$d\ s \to d\ c\ l^-\ \bar{\nu}\ \gamma$
$u\ s \to d\ s\ l^+\ \nu\ \gamma$	$u\ s \to u\ c\ l^-\ \bar{\nu}\ \gamma$

After being calculated in *qqwpaqq* or *qqwmaqq*, the four matrix elements are generalized to all possible flavor combinations in *m2s_wbfw* and multiplied by the PDFs.

3.2.1. Matrix element

For the calculation of the leading order matrix element, there are 72 Feynman diagrams that have to be taken into account. They can be classified into six topologies, presented in figure 3.1.

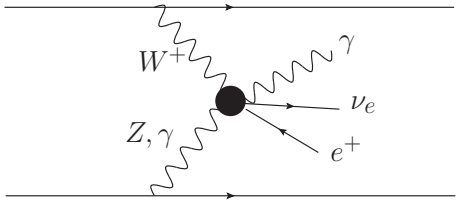

(a) Gauge boson scattering in W V → W γ

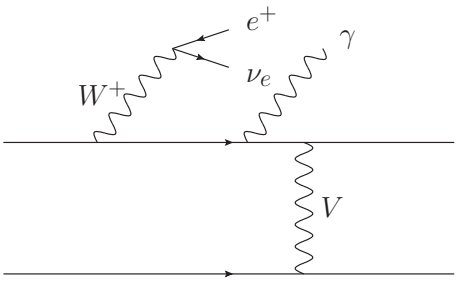

(b) Three gauge bosons on one quark line

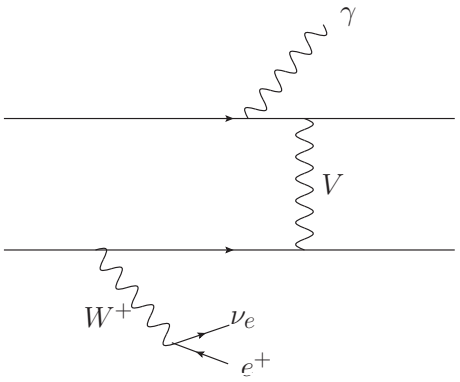

(c) Two gauge bosons on each quark line respectively.

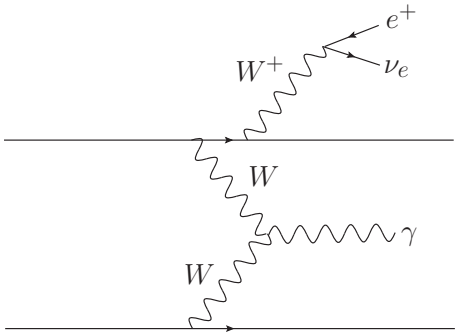

(d) $W^+ W^- \to \gamma$

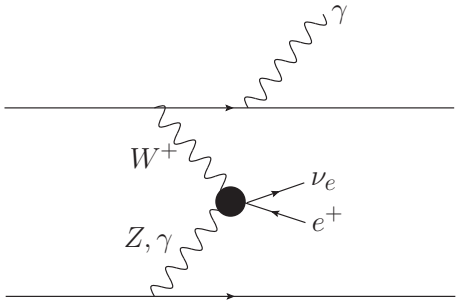

(e) W V → W

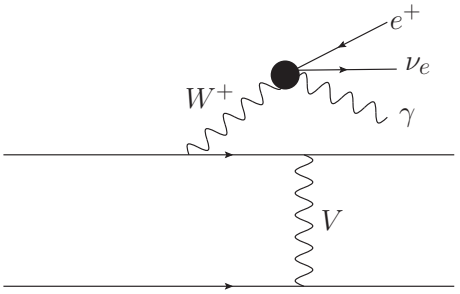

(f) $W \to W\gamma$

Figure 3.1: The figures above show the six general topologies. The black circles represent the leptonic tensors (section 3.2.2).

The black circles represent the leptonic tensors, which contain all possible electroweak leading order diagrams for the given initial and final state particles. The quartic couplings, $WW\gamma\gamma$ and $WWZ\gamma$, occur only in the topology of figure 3.1a. This topology is also the only one that will get only vertex corrections at next-to-leading order. The topology with three gauge bosons on one quark line (figure 3.1b) will get virtual corrections up to a pentagon at NLO QCD. All remaining topologies give rise to box corrections at NLO. The topology with two gauge bosons on each quark line will have two box corrections, one for the upper and one

the lower line separately. This topology will give rise to a Heptagon diagram if one considers gluon exchange between the quark lines. But the interference terms of these contributions with the corresponding Born contributions are identically zero due to their color structure, and therefore not considered.
In the following, it will be illustrated how to calculate the contribution of one topology to the total matrix element. As an example the topology $WW \to \gamma$ (figure 3.1d) is chosen. First of all, we need the leptonic tensor.

3.2.2. Construction in VBFNLO

The leptonic tensors contain the electroweak part of the diagrams. This is especially handy since they are the same for all subprocesses and the NLO QCD corrections only affect the quark lines. Therefore, the leptonic tensors have to be calculated only once per phase space point. This saves a significant amount of computing time. For the calculation of the leptonic tensors, the routines of the *HELAS* package [31] are used. With the help of the *HELAS* routines, one can compute different wave functions for a fixed set of external helicities. For fermions, the routines that generate an in- or outgoing particle are:

- $IXXXXX(p_f^\mu, m_f, hel, part, |f\rangle)$,
- $OXXXXX(p_f^\mu, m_f, hel, part, \langle f|)$,

respectively. Here p_f^μ, denotes the fermion's 4-momentum, m_f its mass and *hel* its helicity. *part* represents whether the fermion is a particle or an anti-particle. *hel* and *part* are quantities that can be either $+1$ or -1. The routines *IXXXXX* and *OXXXXX* return the bra $\langle f|$ or ket $|f\rangle$ as an array, respectively. $|f\rangle$ corresponds to the Dirac spinor u for particles and v for anti-particles and $\langle f|$ to $\bar{u}$ and $\bar{v}$.
Another important *HELAS* routine is:

- $VXXXXX(p_V^\mu, m_V, hel, In/Fin, \epsilon_V^\mu)$,

which calculates the polarization vector of an external vector boson. Analogously to the routines above, p_V^μ is the momentum of the vector boson, m_V its mass and *hel* its helicity. In/Fin is ± 1 and denotes whether the vector boson is in the initial or the final state. ϵ_V^μ is the polarization vector computed by *VXXXXX*. A routine, which is not included but very similar to the ones in the *HELAS* package, is:

- $VCARTX(p_V^\mu, m_V, \Gamma_V, polcart, In/Fin, \epsilon_V^\mu)$.

It computes the polarization vector ϵ_V^μ of an off-shell vector boson. These bosons couple to quark lines and other vector bosons. Γ_V stands for the decay width and *polcart* for the Cartesian polarization of the vector boson.

The leptonic tensor $\Gamma^{\mu\nu}_{WW\to\gamma}$ in figure 3.2 is constructed by calling the routine *VCARTX* for each W boson and each Cartesian polarization, which is done in two loops. The external photon is created with *VXXXX*. The triple gauge boson coupling is built with the routine *VVVXXX*.

Now that we have the leptonic tensor, we need to compute the off-shell current j_W^μ of the W that is attached to the upper line in figure 3.1d. For this, we use the following routine:

- $JIOXXX(|f_{in}\rangle, \langle f_{out}|, G_F, m_W, \Gamma_W, j_W^\mu)$.

$|f_{in}\rangle$ and $\langle f_{out}|$ are the wave functions of the W decay products and G_F is the Fermi coupling constant.

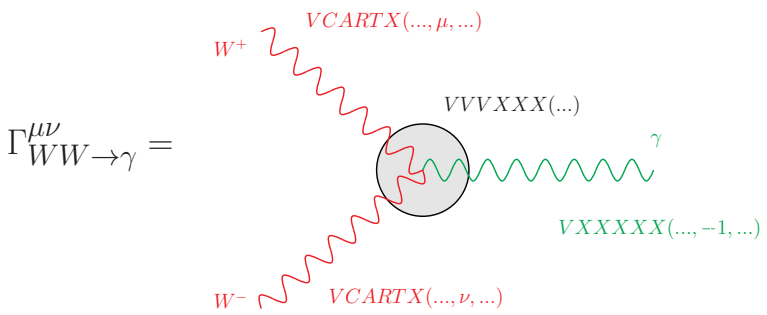

Figure 3.2: For each component of the leptonic tensor $\Gamma^{\mu\nu}_{WW\to\gamma}$ two W bosons with Cartesian polarizations μ and ν are generated with the routine *VCARTX*. Then these off-shell currents are contracted with the polarization vector of the photon ϵ^{μ}_{γ} via the function *VVVXXX*. The photon polarization vector is calculated with the function *VXXXXX*.

The fermions are generated with the functions *IXXXXX* and *OXXXXX* as described above. Their helicity is fixed since the W boson couples only to left-handed particle and right-handed anti-particles. The routine *JIOXXX* connects them and creates the W off-shell current j^{μ}_{W} as shown in figure 3.3.

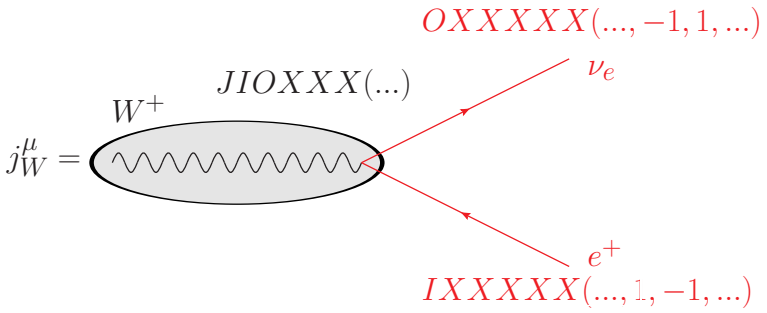

Figure 3.3: The off-shell current for the W^+ boson is constructed by calling the function *JIOXXX*. This routine needs the bra and the ket vectors of the positron and the electron neutrino as input and returns j^{μ}_{W}.

Now that we have the electroweak part, we need to look at the quark lines. For the calculation of the bra and ket vectors for the quarks, the following routine is used:

- $psi0m(n_f, p^{\mu}_i, sign(i), \Psi)$,

where n_f is the number of fermions, for which the bras and kets are to be calculated, p^{μ}_i is an array containing the momenta of the quarks and $sign(i)$ indicates whether particle i is a quark or an anti-quark. The subroutine returns a complex array Ψ containing the ket vector for outgoing and the bra vector for incoming quarks, respectively.

With those bras and kets, we can already calculate a current $j^{\mu}_{q_2q_1} = \langle p_2| \gamma^{\mu} |p_1\rangle$. For this purpose, we use the routine:

- $curr6(sigmax, \langle p_2|, p^{\mu}_2, |p_1\rangle, p^{\mu}_1, j^{\mu}_{q_2q_1})$.

sigmax is an upper limit for the helicity of the current. $\langle p_2|$ and $|p_1\rangle$ are the output of *psi0m* with their respective momenta p^{μ}_2 and p^{μ}_1 that are needed for the calculation of $j^{\mu}_{q_2q_1}$. Moreover, the subroutine *curr6* also stores the momentum of the current in its 4^{th} and 5^{th} component.

It is also possible to use the subroutines *ket2c* and *bra2c* in order to attach a vector boson to a quark line:

- $ket2c(|p\rangle, chreal, p^{\mu}, sigma, k^{\nu}_W, j^{\nu}_W, |p + W\rangle, (p - k)^{\mu})$,
- $bra2c(\langle p|, chreal, p^{\mu}, sigma, k^{\nu}_W, j^{\nu}_W, \langle p + W|, (p + k)^{\mu})$.

Here, *chreal* indicates whether one component of the ket (bra) is real and *sigma* is the helicity of the quark. k_W^ν is the momentum of the vector boson (here the W) and j_W^ν is its off shell current. The output of the subroutines are the new ket (bra) of the quark with the attached vector boson and its new momentum.

Now we have all the building blocks for the matrix element $WW \to \gamma$ (figure 3.1d). The following functions are used to contract the building blocks:

- *contract_T1j*($\Gamma^{\nu\mu}_{WW\to\gamma}$, $j_\nu^{q_3q_4}$, $\epsilon^\mu_{WW\to\gamma}$),
- *dotcc*(A_μ,B^μ),
- *dotrc*(C_μ,B^μ).

contract_T1j contracts a complex rank two tensor with a current and returns the resulting current. *dotcc* and *dotrc* compute scalar products. *dotcc* contracts two complex 4-vectors and *dotrc* a real one with a complex one. In order to calculate the matrix element, the leptonic tensor $\Gamma^{\nu\mu}_{WW\to\gamma}$ is contracted with the current of the lower line $j^\nu_{q_3q_4}$ first and then the resulting current $\epsilon^\mu_{WW\to\gamma}$ is contracted with the current of the upper line $j^\nu_{q_2q_1W}$. The remaining coupling constants are then multiplied to the matrix element. The construction of the whole example matrix element is depicted in figure 3.4.

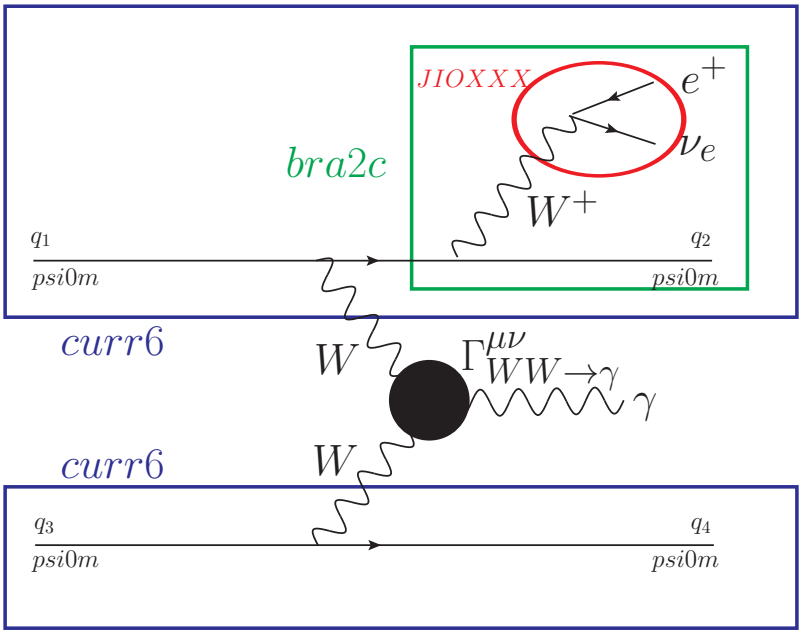

Figure 3.4: This figure shows the construction of the Feynman diagram $WW \to \gamma$ depicted in figure 3.1d. The off-shell current of the W boson j_W^μ is attached to the final state quark of the upper line using *bra2c*. Now the upper and the lower line quarks are put together to currents using *curr6*. The lower line current is then contracted with the leptonic tensor $\Gamma^{\nu\mu}_{WW\to\gamma}$ with the help of *contract_T1j*. The resulting current $\epsilon^\mu_{WW\to\gamma}$ is finally contracted with the current of the upper line quarks using *dotcc*.

3.2.3. Gauge terms

So far, we have only considered the $g^{\mu\nu}$ term of the gauge boson propagator. Using the complex mass scheme [32], the full gauge boson propagator in unitary gauge is:

$$D_V^{\mu\nu} = \frac{-i}{k^2 - m^2 + im\Gamma}\left(g^{\mu\nu} - \frac{k^\mu k^\nu}{k^2}\right). \tag{3.10}$$

Although the remaining $k^\mu k^\nu$ terms are usually small in most phase space regions at collider energies around 14 TeV, they can not be neglected since this would violate gauge invariance. For the calculation of the $k^\mu k^\nu$ terms one can simply contract $\epsilon^\mu_{WW\to\gamma}$ with the momentum of j^ν_W and multiply the result with the scalar product of the upper line quark current with the W boson current $j^\mu_{q_1 q_2} j^W_\mu$.

With the subroutines mentioned above, it is possible to construct all the topologies of figure 3.1 except for the diagrams with three gauge bosons attached to one line (figure 3.1b). Those diagrams are built using the routine *s1c*:

- *s1c*($\langle p + V_1|$, $j^\mu_{V_2}$, *timeex*, *sigma*, $|q + V_3\rangle$).

This function returns the matrix element $\langle p + V_1| \not{J}^\mu_{V_2} |q + V_3\rangle$. The bool variable *timeex* indicates whether the time component of the current $j^\mu_{V_2}$ vanishes. The bra $\langle p + V_1|$ (ket $|q + V_3\rangle$) represents the incoming (outgoing) quark with momentum p^μ (q^μ), to which the vector boson V_1^μ (V_3^μ) is attached.

3.2.4. CKM matrix

In this work, the Cabibbo-Kobayashi-Maskawa matrix V_{CKM} introduced in section 2.2.1 has been set to the identity matrix. This will be justified in this section following the reasoning of Ref. [33].
Let us consider only the subprocess $d\ c \to d\ s\ l^+\ \nu\ \gamma$ of $W^+\gamma jj$ production. We need to distinguish between two types of diagrams:

- Diagrams with only one W boson being emitted from the quark lines. These diagrams are necessarily proportional to V_{cs}.
- Diagrams with two W bosons attached to one quark line and one to the other. These diagrams are proportional to $V_{cs}V^\dagger_{di}V_{id}$ with $i = u, c, t$. If we assume that all quarks are massless the sum over all flavors becomes

$$\sum_{i=u,c,t} V_{cs}V^\dagger_{di}V_{iu} = V_{cs}\sum_{i=u,c,t} V^\dagger_{di}V_{id} = V_{cs}\mathbb{1}, \tag{3.11}$$

  since V_{CKM} is unitary. The error that we make by neglecting the top mass is proportional to $|V_{dt}|^2 \approx 10^{-4}$ and thus negligible.

In both cases, the matrix element squared is proportional to $|V_{cs}|^2$. Additional to $d\ c \to d\ s\ l^+\ \nu\ \gamma$, the channels $d\ c \to d\ d\ l^+\ \nu\ \gamma$ and $d\ c \to d\ b\ l^+\ \nu\ \gamma$ contribute to $d\ c \to j\ j\ l^+\ \nu\ \gamma$ scattering. The sum over the three channels above is proportional to:

$$|V_{cs}|^2 + |V_{cd}|^2 + |V_{cb}|^2 = 1, \tag{3.12}$$

by unitarity. So one obtains the same result by calculating only the first subprocess with V_{CKM} set to unity.

3.3. Phase space

In order to calculate the total cross section, one does need the matrix element as well as the corresponding phase space element $d\Phi_n$ from equation (3.1). For a given process $q_1 q_2 \to f_1 \dots f_n$, it reads

$$d\Phi_n = (2\pi)^4 \delta^4 \left(p_{q_1} + p_{q_2} - \sum_{i=1}^{n} p_{f_i} \right) \prod_{i=1}^{n} \frac{d^3 \vec{p_{f_i}}}{(2\pi)^3 2E_{f_i}}. \tag{3.13}$$

Here, p_{q_i} are the 4-momenta of the incoming partons and p_{f_i} (E_{f_i}) the momenta (energies) of the final state particles. The product is constructed in a Lorentz invariant way and the δ-function assures the conservation of momenta.

Since we use the complex mass scheme [32], the propagators of massive gauge bosons are given by equation (3.10). In the squared amplitude $|\mathcal{M}|^2$, this leads to Breit-Wigner-resonances

$$|\mathcal{M}|^2 \propto p(q^2) \propto \frac{1}{(q^2 - m^2)^2 + m^2\Gamma^2}. \tag{3.14}$$

Here, $p(q^2)$ is the probability to create a gauge boson with invariant mass q^2. It peaks at $q^2 = m^2$ and its width is determined by the decay width Γ of the gauge boson.
We can use this knowledge and do some manual importance sampling to improve the convergence of the Monte-Carlo integration. This means that we map more phase space points into the resonant regions from the very beginning.
The photon can be created in two different phase space channels, shown symbolically in figure 3.5. It can be either created as an additional jet since there is no difference between jets and photons at the level of the phase space generation, or it can be radiated off the W boson (figure 3.1f). Both cases cover different regions of the phase space and a multi-channel generator can be used to get a good phase space sampling in both regions.

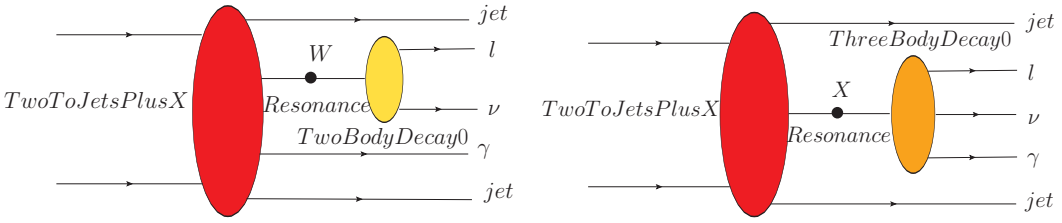

Figure 3.5: For $W^{\pm}\gamma jj$ production two phase space channels are necessary to improve the convergence of the Monte-Carlo. The photon can be either created as a jet or it can be radiated off the W boson as in the topology $W \to W\gamma$ (figure 3.1f).

The contribution of each channel is calculated separately in VBFNLO. To avoid double counting of phase space points, there is a function called *Choose_PS* that determines the correct channel for each phase space point. The decision criterion is the invariant mass of the $l\nu\gamma$ system. If it is close to the mass of the W boson the point must be in the $W \to W\gamma$ channel.

How the phase space is built up will be explained in detail for the channel $W \to W\gamma$. With the first random number *rand*[1] from VEGAS [28], the function *Resonance* calculates the

invariant mass of the $l\nu\gamma$ system. This is done via tan mapping, which will be briefly explained in the following. The phase space integral has the following form:

$$I = \int_{q^2_{min}}^{q^2_{max}} \frac{dq^2}{2\pi} \frac{f(q^2)}{(q^2 - m^2)^2 + (m\Gamma)^2}. \tag{3.15}$$

Here, the function $f(q^2)$ represents the remaining part of the matrix element $|\mathcal{M}|^2$. In our case, m and Γ are the mass and the width of the W boson, respectively. Our goal is to map this integral onto the plane space of the random numbers. We make the substitutions:

$$q^2 = m^2 + m\Gamma \tan x \quad \text{and} \quad dq^2 = m\Gamma(1 + \tan^2 x)dx, \tag{3.16}$$

and obtain:

$$I = \int_{x_{min}}^{x_{max}} f(x)dx \quad \text{with} \quad x_i = arctan\left(\frac{q_i^2 - m^2}{m\Gamma}\right), \quad i = min, max. \tag{3.17}$$

This integral can be mapped to the interval [0,1] via the substitution:

$$x = x_{min} + (x_{max} - x_{min}) * R \qquad dx = (x_{max} - x_{min}) * dR. \tag{3.18}$$

The resulting integral is:

$$I = \frac{x_{max} - x_{min}}{2\pi m\Gamma} \int_0^1 f(q^2(x(R)))dR. \tag{3.19}$$

Now, the integrand is flat and the random numbers can be sampled from the interval [0,1]. Thus, the integral can be evaluated with the Monte-Carlo method very efficiently.

The function *Resonance*:

- *Resonance*(m^2, $m\Gamma$, q^2_{min} ,q^2_{max} , $rand[1]$, $weight$, $q^2_{l\nu\gamma}$),

does not only yield the invariant mass of the $l\nu\gamma$ system, but also the new weight of the phase space point by taking the Jacobi-factors of the substitutions into account:

$$weight_{new} = weight * \frac{x_{max} - x_{min}}{2\pi} m\Gamma(1 + \tan^2 x). \tag{3.20}$$

Now, the function *TwoToJetsPlusX* is used to calculate the momenta of the two incoming partons $\vec{k}_1$ and $\vec{k}_2$, their corresponding Feynman x values x_1 and x_2, the momenta of the outgoing jets $p^\mu_{jet_i}$ and the $l\nu\gamma$ system $p^\mu_{l\nu\gamma}$ and the new weight:

- *TwoToJetsPlusX*(#*Jets*, $rand[7]$, 0, E_{cm}, p_T^{cut}, $q^2_{l\nu\gamma}$, $\vec{k}_1$, $\vec{k}_2$, x_1, x_2, $p^\mu_{l\nu\gamma}$, $p^\mu_{jet_i}$, $weight$).

To achieve this the function requires the number of jets #*Jets*, 3 random numbers for each jet stored in $rand[7, ..., 12]$, the collider energy E_{cm}, the cut on the transverse momentum of the jet definition p_T^{cut} and $q^2_{l\nu\gamma}$.

Finally, the decay of the intermediate state particle into lepton, neutrino and photon is calculated with the function *ThreeBodyDecay0*:

- *ThreeBodyDecay0*($rand[2]$, $p^\mu_{l\nu\gamma}$, $q^2_{l\nu\gamma}$, p^μ_l, p^μ_ν, p^μ_γ, $weight$).

It uses the momentum and the invariant mass of the $l\nu\gamma$ system and 5 random numbers to generate the momenta of the decay particles p^μ_l, p^μ_ν and p^μ_γ and a new weight. All generated momenta are now passed to the routine *Cuts* in **cuts.F**.

3.4. Next-to-leading-order calculation

In order to calculate the next-to-leading-order cross section, one needs to calculate the real emission (RE) and the virtual corrections part. This has been explained in section 2.1. The total next-to-leading-order cross section for a process with m particles in the final state has the form

$$\sigma^{NLO} = \int_{m+1} d\sigma^R + \int_m d\sigma^V + \int_m d\sigma^C. \tag{3.21}$$

Here, $d\sigma^R$ denotes the real emission part, which has to be integrated over the $m+1$ particle phase space and $d\sigma^V$ denotes the virtual loop corrections. $d\sigma^C$ is the collinear subtraction counterterm, which is needed to absorb parts of the initial state singularities into a redefinition of the PDFs. The calculation of these parts is more complex and time consuming than the leading order calculation, but we will see that the scale uncertainty is significantly reduced at NLO QCD.

The LO cross section is of order $\mathcal{O}(\alpha_{em}^5)$ so the NLO QCD cross section is of order $\mathcal{O}(\alpha_{em}^5 \alpha_S)$. The real emission Feynman diagrams have one additional gluon coupling compared to leading order, which corresponds to a factor $\alpha_S^{1/2}$. Thus the real emission cross section can be calculated by

$$\sigma_R = \int dx_1 dx_2 \sum_{\substack{sub- \\ processes}} f_{a_1/p_1}(x_1) f_{a_2/p_2}(x_2) \frac{1}{2\hat{s}} \int d\Phi_{2\to m+1} \Theta(cuts) \overline{\sum_{\substack{spin, \\ color}}} |\mathcal{M}_{RE}|^2 . \tag{3.22}$$

However, in the matrix elements with virtual corrections the gluon couples in two places, which leads directly to a factor α_S. Therefore, we calculate the interference term given by

$$\sigma_V = \int dx_1 dx_2 \sum_{\substack{sub- \\ processes}} f_{a_1/p_1}(x_1) f_{a_2/p_2}(x_2) \frac{1}{2\hat{s}} \int d\Phi_{2\to m} \Theta(cuts) \overline{\sum_{\substack{spin, \\ color}}} 2Re\left[\mathcal{M}_B \mathcal{M}_V\right] . \tag{3.23}$$

This term is of order $\mathcal{O}(\alpha_{em}^5 \alpha_S)$.

3.5. Real emission contribution

To obtain the QCD real emission corrections, an additional gluon has to be added to each diagram. It can be in the initial or in the final state. The following Feynman diagrams in figure 3.6 show the topologies, that have to be taken into account for the calculation of the real emission.

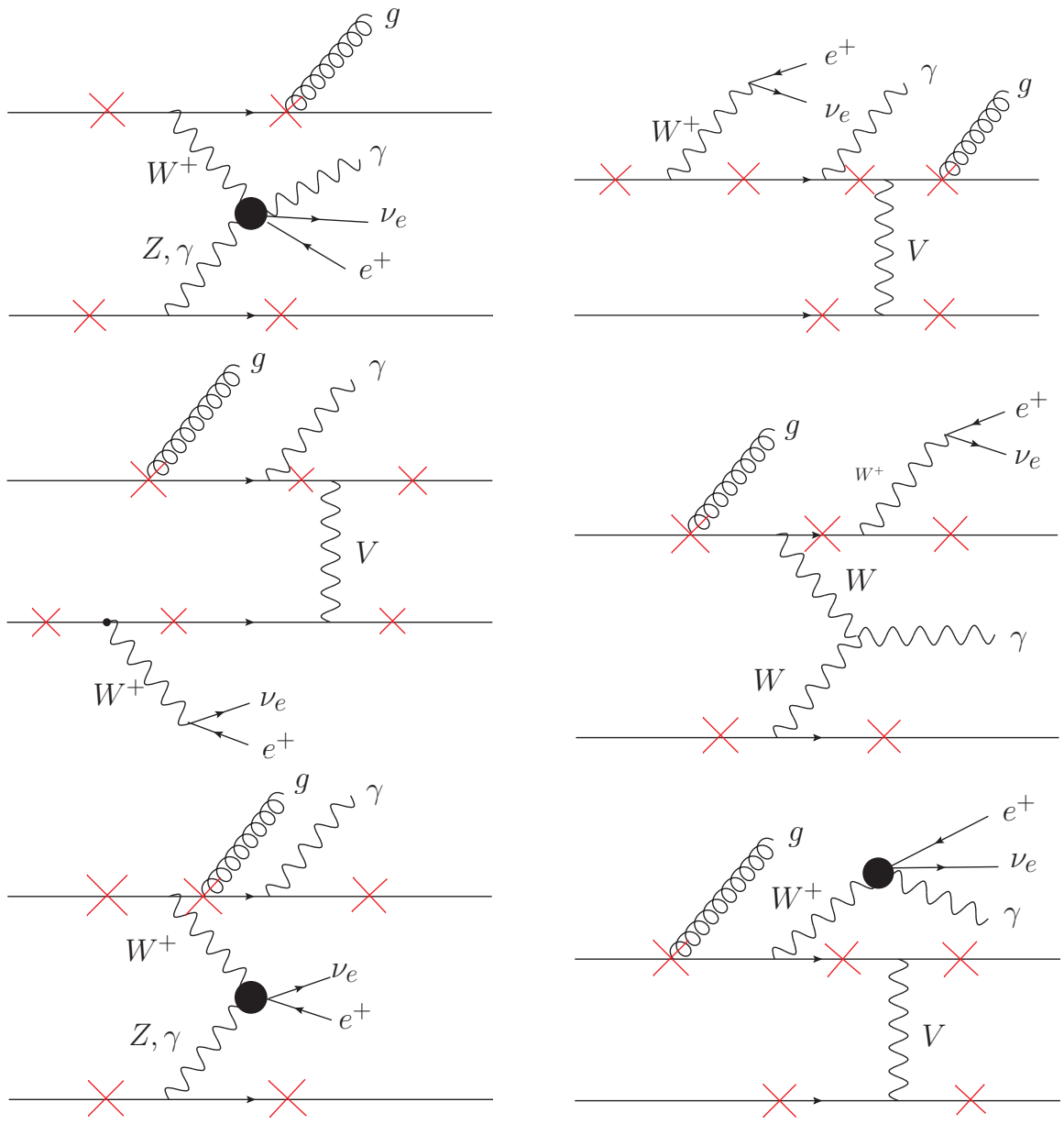

Figure 3.6: The figures above show again the six general topologies found in figure 3.1 with an additional gluon attached to each diagram. The red crosses mark all the places where the gluon can be attached.

In each topology, the gluon is attached at an example spot. The red crosses mark all possible positions where the gluon can be attached. In total, 369 diagrams have to be calculated for the real emission.

Instead of a quark going to a quark and a gluon, it is also possible that an initial state gluon splits into a quark and an anti-quark. The initial state gluons access the gluon PDFs, which are enhanced at the LHC and could result in potentially large NLO QCD corrections. This is a completely new channel entering at NLO QCD, which is basically calculated at LO. The remaining scale uncertainty at NLO is partly due to this channel. However, due to our scale choice and the VBF cuts we will apply, the initial state gluon contributions do not result in large NLO QCD corrections.

The construction of the matrix elements for the real emission diagrams is very similar to the leading order. The main difference is the gluon, which can be generated using the subroutine *polvec*.

- polvec(p_g^μ, *pol*, ϵ_g^μ)

p_g^μ is the momentum of the gluon and ϵ_g^μ its polarization vector. Since the gluon is a massless gauge boson, it can have two different polarizations, represented by *pol*.

The gluon now can be attached to the quarks using the routines *ket2c* and *bra2c*. Furthermore, it is possible to attach several gauge bosons to a quark using those functions. In this way, all the necessary diagrams can be constructed similarly to the leading order diagrams.

3.5.1. Catani-Seymour dipole subtraction

A general problem in numerical next-to-leading-order calculations arises, because the real emission and the virtual corrections have to be calculated separately, since their phase space is different. These two parts of equation (3.21) are separately divergent in four dimensions and only their sum, the total NLO cross section, is finite. Thus, without further modifications it is not possible to calculate these integrals separately using numerical methods.

A general solution for this problem was proposed by Catani and Seymour [34]. With the help of dimensional regularization, which means solving these integrals in $d = 4 - 2\epsilon$ dimensions, the divergences appear as $1/\epsilon$ and $1/\epsilon^2$ poles. The structure of the poles is the same for the virtual correction and the real emission, but the overall sign is different.

The idea is to introduce a local counterterm $d\sigma^A$ for the real emission part $d\sigma^R$. $d\sigma^A$ is constructed in such a way that it reproduces the singular behavior of $d\sigma^R$. This counterterm is then subtracted from the real and added to the virtual part of the cross section, correspondingly

$$d\sigma^{NLO} = \left[d\sigma^R - d\sigma^A\right] + d\sigma^A + d\sigma^V + d\sigma^C. \tag{3.24}$$

An additional condition for $d\sigma^A$ is that it must be integrable analytically over the one parton phase space, such that one can cancel the divergences analytically against the virtual part

$$\sigma^{NLO} = \int_{m+1} \left[d\sigma^R - d\sigma^A\right] + \int_{m+1} d\sigma^A + \int_m d\sigma^V + \int_m d\sigma^C \tag{3.25}$$

$$\stackrel{\epsilon\to 0}{=} \int_{m+1} \left[(d\sigma^R)_{\epsilon=0} - (d\sigma^A)_{\epsilon=0}\right] + \int_m \left[d\sigma^V + d\sigma^C + \int_1 d\sigma^A\right]_{\epsilon=0}. \tag{3.26}$$

We remind that the contribution $d\sigma^C$ is needed to absorb parts of the initial state singularities into a redefinition of the PDFs. Now all the individual integrals are finite in four dimensions and can be solved using the Monte-Carlo method.

If one carries out the integration over the one particle phase space in the second part of equation (3.26) one will obtain

$$\int_m d\sigma^V + \int_{m+1} d\sigma^A + \int_m d\sigma^C = \int_m \left[d\sigma^V + d\sigma^B \otimes \boldsymbol{I}(\epsilon)\right] + \int_0^1 dx \int_m d\sigma_B \otimes (\boldsymbol{P}(x) + \boldsymbol{K}(x)) \,. \tag{3.27}$$

Here, $d\sigma^B$ denotes the born cross section, $\boldsymbol{I}(\epsilon)$ the insertion operator and the operators $\boldsymbol{P}$ and $\boldsymbol{K}$ correspond to the finite collinear remainder.

According to [33], the insertion operator $\boldsymbol{I}(\epsilon)$ is given by

$$\langle \boldsymbol{I}(\epsilon) \rangle = \frac{\alpha_S(\mu_R)}{2\pi} C_F \left(\frac{4\pi\mu_R}{Q^2}\right)^{\epsilon} \Gamma(1+\epsilon) \left[\frac{2}{\epsilon^2} + \frac{3}{\epsilon} + 9 - \frac{4}{3}\pi^2\right], \tag{3.28}$$

for this process. The poles of the $\boldsymbol{I}$ operator cancel exactly against the poles of the virtual cross section $d\sigma^V$ according to the Kinoshita-Lee-Nauenberg (KLN) theorem [35].

Obviously, the crucial part of this subtraction method is the construction of $d\sigma^A$. One of the big advantages of the Catani-Seymour method is that it makes use of the Born cross section $d\sigma^B$, which we already know

$$d\sigma^A = \sum_{dipoles} d\sigma^B \otimes dV_{dipole}. \tag{3.29}$$

The symbol $\otimes$ stands for a properly defined phase space mapping of the real emission contributions to the born kinematics and dV_{dipole} for the dipole factors that reproduce the singular behavior of $d\sigma^R$.

There are two types of singularities that occur in $d\sigma^R$:

- Soft singularities occur in the so-called soft region where the gluon momentum is:

$$p_g^\mu = \lambda q^\mu, \qquad \lambda \to 0, \tag{3.30}$$

  with an arbitrary 4-momentum q^μ. In this region, the matrix element $|\mathcal{M}_{m+1}|^2$ behaves as $1/\lambda^2$.

- The collinear region is characterized by two partons whose R-separation goes to zero. We have to distinguish between two cases. Two final state partons with momenta p_i^μ and p_j^μ can become collinear, which can be defined as

$$\begin{aligned} &p_i^\mu = zp^\mu + k_\perp^\mu - \frac{k_\perp^2}{z}\frac{n^\mu}{2p\cdot n}, \qquad p_j^\mu = (1-z)p^\mu - k_\perp^\mu - \frac{k_\perp^2}{1-z}\frac{n^\mu}{2p\cdot n}, \\ &2p_i \cdot p_j = -\frac{k_\perp^2}{z(1-z)}, \qquad k_\perp \to 0. \end{aligned} \tag{3.31}$$

  Here, $k_\perp$ denotes the transverse component, p^μ the collinear direction and n^μ is an auxiliary vector specifying the collinear limit ($k_\perp p = k_\perp n = 0$). z is the momentum fraction that is involved in the splitting $ij \to i+j$. In this region, the matrix element $|\mathcal{M}_{m+1}|^2$ behaves as $1/p_i \cdot p_j$.
  Moreover, a final-state parton i can become collinear to an initial-state parton a

$$\begin{aligned} &p_i^\mu = (1-x)p_a^\mu + k_\perp^\mu - \frac{k_\perp^2}{1-x}\frac{n^\mu}{2p_a\cdot n}, \\ &2p_i \cdot p_a = -\frac{k_\perp^2}{1-x}, \qquad k_\perp \to 0. \end{aligned} \tag{3.32}$$

The momentum of the parton ai that is generated in the splitting $a \to ai + i$ is xp_a^μ where x is a dimensionless kinematic variable denoting its fraction of momentum. In this case, the matrix element behaves as $1/(xp_i \cdot p_a)$.

The singular behavior of the real emission matrix element $\mathcal{M}_{m+1}$ factorizes with respect to the born matrix element $\mathcal{M}_m$ analogously to equation (3.29)

$$|\mathcal{M}_{m+1}|^2 \to |\mathcal{M}_m|^2 \otimes \mathbf{V}_{ij,k}. \tag{3.33}$$

The structure of $\mathbf{V}_{ij,k}$ corresponds to a classical dipole with respect to the color and spin indices. These dipoles are universal and the reason why this is called dipole factorization formula. For the calculation of $|\mathcal{M}_m|^2$ the partons (i) and (j) are combined to one external parton (ij). In addition, a spectator parton (k) is used to get the parton (ij) back on the mass shell. This transformation leads to the so-called tilde kinematics, which will be described below.

The explanation of the subtraction procedure follows the one in reference [36] since the singular behavior is exactly the same for Higgs and $W\gamma$ production in VBF. Let us look at the subprocess:

$$\bar{q}(p_a) + Q(p_b) \to g(p_1) + \bar{q}(p_2) + Q(p_3) + l^+(p_l) + \nu(p_\nu) + \gamma(p_\gamma), \tag{3.34}$$

denoted by the real emission matrix element $\mathcal{M}_r^{\bar{q}}$ and represented by figures 3.7a and 3.7b. This subprocess has collinear singularities from initial- or final-state splitting and soft gluon singularities.

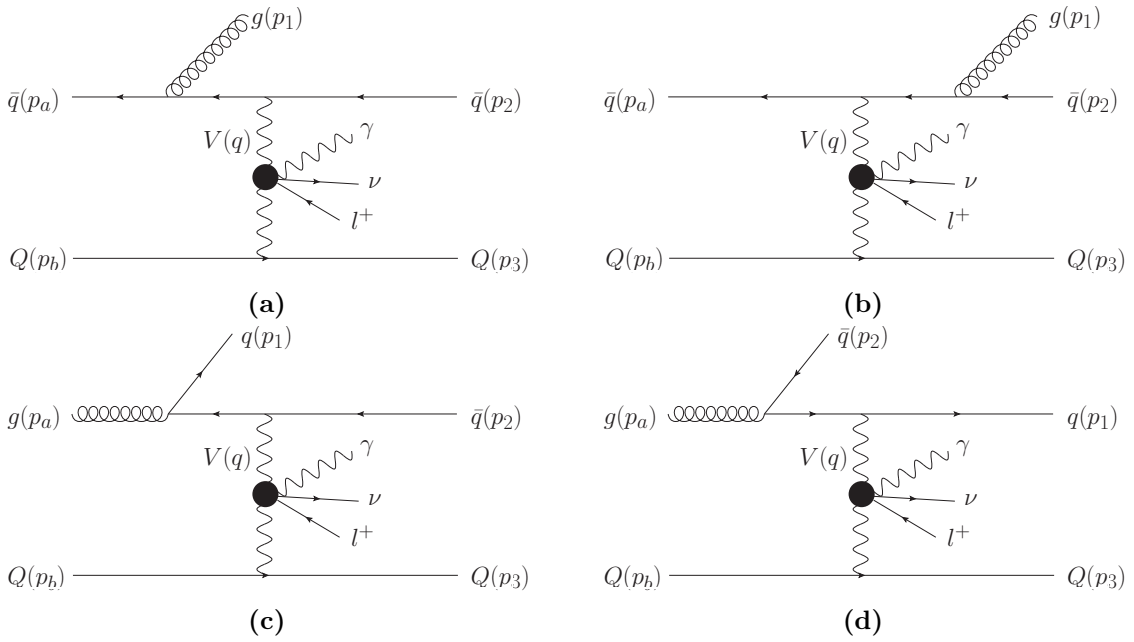

Figure 3.7: This figure shows an example topology with all the possible real emission contributions. A final-state gluon can be produced in either initial- (a) or final-state $\bar{q} \to \bar{q}g$ splitting (b). In gluon initiated processes shown in subfigures (c) and (d) we only have initial-state splitting but the gluon can become collinear to either, the quark (c) or the anti-quark (d).

For the construction of the counterterm that reproduces those singularities we need the born matrix element $\mathcal{M}_B^{\bar{q}}$ for the process

$$\bar{q}(\tilde{p}_a) + Q(p_b) \to \bar{q}(\tilde{p}_2) + Q(p_3) + l^+(p_l) + \nu(p_\nu) + \gamma(p_\gamma), \tag{3.35}$$

with the tilde kinematics

$$\tilde{p}_a = x p_a, \qquad \tilde{p}_2 = p_1 + p_2 - (1-x)p_a, \tag{3.36}$$

and the dimensionless kinematic variables

$$\begin{aligned} x &= 1 - \frac{p_1 \cdot p_2}{(p_1+p_2)\cdot p_a}, \\ z &= 1 - \frac{p_1 \cdot p_a}{(p_1+p_2)\cdot p_a} = \frac{p_2 \cdot p_a}{(p_1+p_2)\cdot p_a}. \end{aligned} \tag{3.37}$$

The counterterm can now be constructed as

$$|\mathcal{M}^{\bar{q}}|^2_{sub} = \mathcal{D}_2^{\bar{q}1} + \mathcal{D}_{12}^{\bar{q}} = 8\pi\alpha_S(\mu_R) C_F \frac{1}{Q^2} \frac{x^2+z^2}{(1-x)(1-z)} |\mathcal{M}_B^{\bar{q}}(\tilde{p}_a, \tilde{p}_2, q)|^2. \tag{3.38}$$

$\mathcal{D}_2^{\bar{q}1}$ and $\mathcal{D}_{12}^{\bar{q}}$ are the dipoles for initial- and final-state $\bar{q} \to \bar{q}g$ splitting on the upper line, respectively and $C_F = 4/3$. q is the momentum transferred on the upper line, $q = p_1 + p_2 - p_a$, and $Q^2 = -q^2$ is a measure for the virtuality of the exchanged weak boson $V(q)$. The subtraction matrix element squared in equation (3.38) reproduces the singular behavior of $|\mathcal{M}_r^{\bar{q}}|^2$ for

- soft final-state gluons ($p_1 \to 0 \;\Rightarrow\; x \to 1,\; z \to 1$)
- collinear final-state partons ($p_1 \parallel p_2,\; p_1 \cdot p_2 \to 0 \;\Rightarrow\; x \to 1$)
- collinear initial-state splitting ($p_1 \to (1-x)p_a \;\Rightarrow\; z \to 1$)

For the gluon initiated subprocess denoted by $\mathcal{M}_r^g$ and depicted in figures 3.7c and 3.7d

$$g(p_a) + Q(p_b) \to q(p_1) + \bar{q}(p_2) + Q(p_3) + l^+(p_l) + \nu(p_\nu) + \gamma(p_\gamma), \tag{3.39}$$

where we have $g \to \bar{q}q$ splitting, the counterterm is different, namely

$$\begin{aligned} |\mathcal{M}^g|^2_{sub} = \mathcal{D}_2^{g1} + \mathcal{D}_1^{g2} = 8\pi\alpha_S(\mu_R) T_F \frac{1}{Q^2} \Bigg(& \frac{x^2+(1-x)^2}{1-z} |\mathcal{M}_B^{\bar{q}}(\tilde{p}_a, \tilde{p}_2, q)|^2 \\ & + \frac{x^2+(1-x)^2}{z} |\mathcal{M}_B^{q}(\tilde{p}_a, \tilde{p}_2, q)|^2 \Bigg). \end{aligned} \tag{3.40}$$

The dipole $\mathcal{D}_2^{g1}$ ($\mathcal{D}_1^{g2}$) corresponds to the gluon becoming collinear with the anti-quark (quark), $T_F = 1/2$ and the born matrix elements $\mathcal{M}^{\bar{q}}$ and $\mathcal{M}^q$ correspond to the LO subprocesses

$$\bar{q}(\tilde{p}_a) + Q(p_b) \to \bar{q}(\tilde{p}_2) + Q(p_3) + l^+(p_l) + \nu(p_\nu) + \gamma(p_\gamma) \quad \text{and} \tag{3.41}$$

$$q(\tilde{p}_a) + Q(p_b) \to q(\tilde{p}_2) + Q(p_3) + l^+(p_l) + \nu(p_\nu) + \gamma(p_\gamma), \tag{3.42}$$

respectively.

The subtraction matrix element in equation (3.40) covers the two possible singular constellations

- gluon collinear with quark ($p_a \parallel p_1,\ p_a \cdot p_1 \to 0 \ \Rightarrow\ z \to 1$)
- gluon collinear with anti-quark ($p_a \parallel p_2,\ p_a \cdot p_2 \to 0 \ \Rightarrow\ z \to 0$)

Not only the renormalization of the matrix elements leads to divergences, but divergent terms also occur when the PDFs are renormalized. In order to regularize these divergences we absorb some of the divergent parts of the subtraction matrix elements in equations (3.38) and (3.40) into the PDFs. The remaining part of the cross section is called the finite collinear term $\sigma^{NLO}_{2,coll}$. For the process listed in equation (3.34), it is given by

$$\begin{aligned}\sigma^{NLO}_{2,coll}(\bar{q}Q \to \bar{q}Qgl\nu\gamma) = \int\int_0^1 dx_a \int_0^1 dx_b\, f^c_{\bar{q},p}(x_a,\mu_F,\mu_{Ra}) f_{Q,p}(x_b,\mu_F) \\ \times \frac{1}{2\hat{s}} \left|\mathcal{M}^{\bar{q}}_B\right|^2 F^{(2)}_J(p_2,p_3) d\Phi_5(p_2,p_3,p_l,p_\nu,p_\gamma;p_a+p_b)\end{aligned} \tag{3.43}$$

Here, the center of mass energy is denoted by $\hat{s} = (p_a + p_b)^2$, $F^{(2)}_J$ is the jet finding algorithm for 2 jets, $f_{Q,p}$ is the normal quark PDF for Q and $f^c_{\bar{q},p}$ is the modified anti-quark PDF for $\bar{q}$

$$\begin{aligned}f^c_{\bar{q},p}(x,\mu_F,\mu_R) = \frac{\alpha_s(\mu_R)}{2\pi}\int_x^1 \frac{dz}{z}\Big\{ f_{g/p}\left(\frac{x}{z},\mu_F\right) A(z) \\ \left[f_{\bar{q}/p}\left(\frac{x}{z},\mu_F\right) - z f_{\bar{q}/p}\left(x,\mu_F\right)\right] B(z) + f_{g/p}\left(\frac{x}{z},\mu_F\right) C(z)\Big\} \\ + \frac{\alpha_s(\mu_R)}{2\pi} f_{\bar{q}/p}\left(x,\mu_F\right) D(x),\end{aligned} \tag{3.44}$$

with its integration kernels

$$A(z) = T_F\left[z^2 + (1-z)^2\right] \ln\frac{Q^2(1-z)}{\mu_F^2 z} + 2T_F\, z(1-z), \tag{3.45}$$

$$B(z) = C_F\left[\frac{2}{1-z}\ln\frac{Q^2(1-z)}{\mu_F^2} - \frac{3}{2}\frac{1}{1-z}\right], \tag{3.46}$$

$$C(z) = C_F\left[1 - z - \frac{2}{1-z}\ln z - (1+z)\ln\frac{Q^2(1-z)}{\mu_F^2 z}\right], \tag{3.47}$$

$$D(x) = C_F\left[\frac{3}{2}\ln\frac{Q^2}{\mu_F^2(1-x)} + 2\ln(1-x)\ln\frac{Q^2}{\mu_F^2} + \ln^2(1-x) + \underbrace{\frac{2\pi^2}{3} - \frac{13}{2}}_{c'_{real}}\right]. \tag{3.48}$$

The kernel $D(x)$ yields a constant term that is proportional to the born matrix element squared, denoted by c'_{real}. In *VBFNLO*, we add the finite part of the $\boldsymbol{I}$ operator to this finite term and obtain a new constant

$$c_{real} = c'_{real} + 9 - \frac{4\pi^2}{3} = -\frac{2\pi^2}{3} + \frac{5}{2} \tag{3.49}$$

From the virtual corrections we will also obtain a finite term that is proportional to $|\mathcal{M}_B|^2$, denoted by c_{virt}. Only the sum of these two terms is fixed but the terms can be shifted by a constant. This will be used to implement a consistency check later on in section 4.6.

The integration kernels are the same for the modified quark PDF $f^c_{q,p}$ needed for the subprocess $qQ \to qQl\nu\gamma$. For real emission corrections to the lower quark line the procedure works completely analogously to the one above with the replacements $(p_a \longleftrightarrow p_b)$ and $(p_2 \longleftrightarrow p_3)$. Note that we strictly separate the real emission contribution and the virtual corrections for both quark lines. This allows us to use different scales for both lines, namely the momentum transferred squared between the initial- and the final-state partons of the line.

3.6. Virtual corrections

For the calculation of the virtual-loop corrections, the subroutines *Boxline* and *Penline* have been used. They were created by Francisco Campanario [37]. The *Boxline* routine calculates the matrix element for all possible virtual QCD corrections to a quark line with two vector bosons attached. That includes one box, two vertex and one self energy diagrams as demonstrated in figure 3.8.

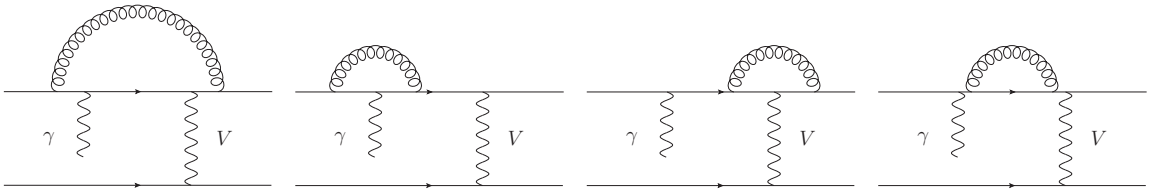

Figure 3.8: The subroutine *Boxline* computes not only the box correction to a quark line with two vector bosons but also the self energy and the two vertex corrections.

Similarly, the *Penline* routine computes the pentagon correction to a quark line with three vector bosons. Furthermore, it also calculates the two box and the three vertex corrections as well as the self energy diagrams as shown in figure 3.9.

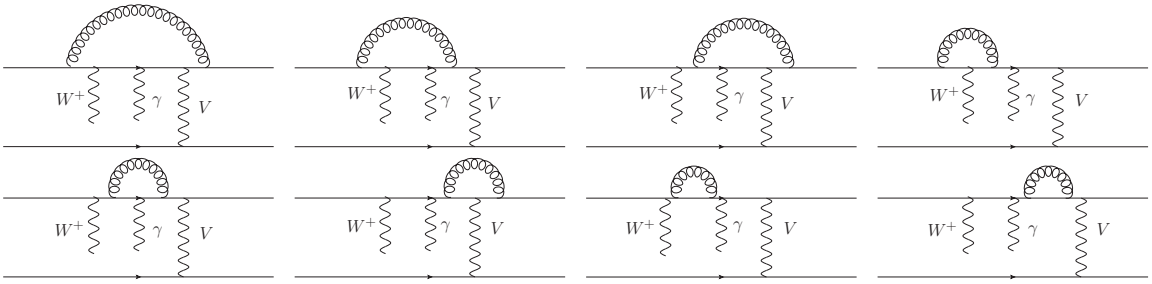

Figure 3.9: The subroutine *Penline* computes the pentagon, two box, three vertex and two self energy corrections to a quark line with three gauge bosons attached in a fixed order.

The *Boxline* routine needs the momenta of the quarks $p^\mu_{q_i}$, their spinors Ψ_i, the momenta of the vector bosons $p^\mu_{V_j}$ and their polarization vector $\epsilon^\mu_{V_j}$ or current $j^\mu_{V_j}$ as input. Furthermore, the renormalization scale μ_{Ri} and the helicity sig of the quark line have to be given to the routine.

- $boxlineABETotal(p^\mu_{q_1}, p^\mu_{V_1}, p^\mu_{V_2}, p^\mu_{q_2}, \Psi_2, \Psi_1, \epsilon^\mu_{V_1}, j^\mu_{V_2}, \mu_{Ri}, sig, \mathcal{M}^g_V, \mathcal{M}_V, \mathcal{M}^g_B, \mathcal{M}_B, div)$

It returns four different matrix elements; the matrix element for the virtual corrections $\mathcal{M}_V$ and the corresponding Born matrix element $\mathcal{M}_B$. Moreover, these two matrix elements are calculated with the replacements $\epsilon^\mu_{V_1} \to p^\mu_{V_2}$ or $j^\mu_{V_2} \to p^\mu_{V_2}$. They are called $\mathcal{M}^g_V$ and $\mathcal{M}^g_B$ and used to create Ward identity tests in **GaugeTest.F**, that allow us to control the numerical stability. The parameter *div* can be set to 0, 1 or 2, to return the matrix elements for the finite part, the $1/\epsilon$ or the $1/\epsilon^2$ poles, respectively. The in- and output of the *Penline* routine works completely analogously.

In the calculation of the loop corrections, one uses Passarino-Veltman tensor reduction [38] to reduce complicated integral to simpler ones. For this, one has to solve relatively simple systems of linear equation with the structure

$$\begin{pmatrix} G_1 & G_2 \\ G_3 & G_4 \end{pmatrix} \begin{pmatrix} C_1 \\ C_2 \end{pmatrix} = \begin{pmatrix} R_1 \\ R_2 \end{pmatrix}. \tag{3.50}$$

Although, this is not difficult to solve on an analytic level by inverting the matrix

$$\begin{pmatrix} C_1 \\ C_2 \end{pmatrix} = \frac{1}{G_1 G_4 - G_2 G_3} \begin{pmatrix} G_4 & -G_2 \\ -G_3 & G_1 \end{pmatrix} \begin{pmatrix} R_1 \\ R_2 \end{pmatrix}, \tag{3.51}$$

numerical problems will arise if the Gram determinant $(G_1 G_4 - G_2 G_3)$ is small. The phase space points, in which this happens, can produce instabilities depending on the severity of the cancellations and have to be rejected.

To reduce the instabilities we use a numerically more stable procedure to invert the matrix, namely the LU decomposition method. The idea is to decompose the Gram matrix into a lower and an upper triangular matrix

$$\begin{pmatrix} G_1 & G_2 \\ G_3 & G_4 \end{pmatrix} = \begin{pmatrix} L_1 & 0 \\ L_2 & L_3 \end{pmatrix} \begin{pmatrix} U_1 & U_2 \\ 0 & U_3 \end{pmatrix}. \tag{3.52}$$

Now, equation (3.50) can be inverted by solving the two systems of linear equations consecutively. This method is numerically a lot more stable compared to simply inverting the matrix. Moreover, it is not more time consuming.

3.6.1. Ward identity test

Despite a reduction of instabilities by a factor 10, the LU decomposition method does not solve the problem of vanishing Gram determinants. To control the accuracy of the result, we make use of Ward identities, described in section 2.2.3. In case those are not satisfied with a required level of accuracy, the point is considered unstable and rejected.
The quintessence of the Ward identity is that a loop diagram with at least one external gauge boson decomposes into several simpler diagrams if one of its external bosons is replaced with its respective momentum. In case of the Penline there are three external gauge bosons. Each of them can be replaced by its momentum to get three quantities that we can check.

For the calculation of a pentagon correction the following integral has to be solved

$$\mathcal{E}_{\mu_2\mu_3\mu_4}(p_1,p_2,p_3,p_4,p_5) = \int \frac{d^dq}{(2\pi)^d}\frac{1}{q^2}\gamma^\alpha \frac{1}{\not{q}+\not{p}_{14}}\gamma_{\mu_4}\frac{1}{\not{q}+\not{p}_{13}}\gamma_{\mu_3}\frac{1}{\not{q}+\not{p}_{12}}\gamma_{\mu_2}\frac{1}{\not{q}+\not{p}_{1}}\gamma_\alpha. \quad (3.53)$$

The momenta are defined as in figure 3.10 and the convention for the momenta is $p_1+p_2+p_3+p_4+p_5=0$. For the sake of clarity, the notation $p_{1j}\equiv\sum_{i=1}^{j}p_i$ has been used.

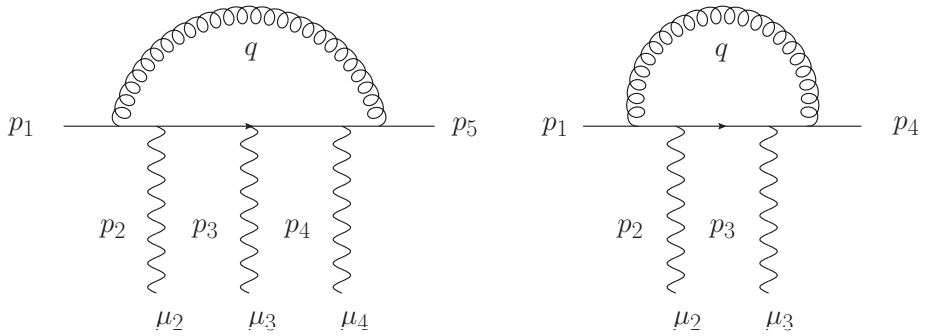

Figure 3.10: The diagram on the left hand side is a pentagon represented by the function $\mathcal{E}_{\mu_2\mu_3\mu_4}(p_1,p_2,p_3,p_4,p_5)$. The diagram on the right is a box denoted by $\mathcal{D}_{\mu_2\mu_3}(p_1,p_2,p_3,p_4)$.

When we contract $\mathcal{E}_{\mu_2\mu_3\mu_4}(p_1,p_2,p_3,p_4,p_5)$ with the momentum of the first gauge boson $p_2^{\mu_2}$, we can analytically express $\not{p}_2$ as a difference of denominators of two propagators, which is used to reduce the pentagon to a difference of two boxes

$$\begin{aligned} p_2^{\mu_2}\mathcal{E}_{\mu_2\mu_3\mu_4}(p_1,p_2,p_3,p_4,p_5) =& \left[(p_2+p_1+q)^{\mu_2}-(p_1+q)^{\mu_2}\right]\mathcal{E}_{\mu_2\mu_3\mu_4}(p_1,p_2,p_3,p_4,p_5) \\ =& \mathcal{D}_{\mu_3\mu_4}(p_1,p_2+p_3,p_4,p_5)-\mathcal{D}_{\mu_3\mu_4}(p_1+p_2,p_3,p_4,p_5). \end{aligned} \quad (3.54)$$

This procedure works completely analogously when the pentagon $\mathcal{E}_{\mu_2\mu_3\mu_4}(p_1,p_2,p_3,p_4,p_5)$ is contracted with one of the other momenta $p_3^{\mu_3}$ or $p_4^{\mu_4}$

$$\begin{aligned} p_3^{\mu_3}\mathcal{E}_{\mu_2\mu_3\mu_4}(p_1,p_2,p_3,p_4,p_5) &= \mathcal{D}_{\mu_2\mu_4}(p_1,p_2,p_3+p_4,p_5)-\mathcal{D}_{\mu_2\mu_4}(p_1,p_2+p_3,p_4,p_5), \\ p_4^{\mu_4}\mathcal{E}_{\mu_2\mu_3\mu_4}(p_1,p_2,p_3,p_4,p_5) &= \mathcal{D}_{\mu_2\mu_3}(p_1,p_2,p_3,p_4+p_5)-\mathcal{D}_{\mu_2\mu_3}(p_1,p_2,p_3+p_4,p_5). \end{aligned} \quad (3.55)$$

We use these identities to check the numerical accuracy by requiring that these equalities are satisfied within a global precision ϵ. If the deviation is larger than ϵ the Ward test will fail and the virtual contributions for this phase space point will be neglected. It will be shown in section 4.5.5 that this is justified.

For the *Boxline* two Ward identities can be constructed corresponding to the replacement of one of the two external bosons with its momentum. Analogously to the pentagon, the expression for the box diagram reduces to the difference of two vertex corrections. One of those vertex corrections vanishes and the other one can be written as a constant *cte* times the corresponding Born matrix element since vertex corrections are directly proportional to the Born matrix element

$$p_2^{\mu_2}\mathcal{D}_{\mu_2\mu_3}(p_1,p_2,p_3,p_4) = cte * \mathcal{M}^{born}_{\mu_3}. \quad (3.56)$$

Again, we can check that the deviations from this equation is smaller than ϵ by building the normalized quantity

$$\left| p_2^{\mu_2} \mathcal{D}_{\mu_2\mu_3}(p_1, p_2, p_3, p_4)/(cte * \mathcal{M}_{\mu_3}^{born}) - 1 \right| < \epsilon. \tag{3.57}$$

If $cte * \mathcal{M}_{\mu_3}^{born}$ is small, numerical problems might arise. In this case, we subtract both sides of equation (3.56) and check that the absolute value of the result is smaller than ϵ.

The precision of these tests ϵ affects the share of phase space points that fail the test and are neglected. This will be examined in section 4.5.5.

3.6.2. Dimensional reduction

Dimensional reduction (DRED) [39] is a variant of dimensional regularization (DREG) [40]. Both methods are used to regularize loop integrals, which are in general divergent in $D = 4$ dimensions. In DREG, the whole loop integral is evaluated in $D = 4 - 2\epsilon$ dimensions. In DRED, only the momenta are shifted to $D = 4 - 2\epsilon$, whereas the γ matrices and the gauge fields remain in $D = 4$ dimensions.

For the virtual corrections up to pentagons, the analytic expression for the poles of the matrix element is known, independently of whether the external particles are massive or massless [37]. It has the same structure in both schemes and can be written in the following form

$$\begin{aligned} \mathcal{M}_{V_1\ldots V_n} = g^{V_1}\ldots g^{V_n} C_F \frac{\alpha_S(\mu_{Ri})}{4\pi} \Bigg(& \widetilde{\mathcal{M}}_{V_1\ldots V_n} \\ & + \left(\frac{4\pi\mu_{Ri}^2}{Q_i^2} \right)^{\epsilon} \Gamma(1+\epsilon) \left[\frac{A}{\epsilon^2} + \frac{B}{\epsilon} + c_{virt} \right] \mathcal{M}^{\mathcal{B}}_{V_1\ldots V_n} \Bigg). \end{aligned} \tag{3.58}$$

Here, the indices V_j represent the vector bosons attached to the quark line, the corresponding couplings are represented by g^{V_j}, α_S is the strong coupling and μ_{Ri} is the renormalization scale of the quark line. $\widetilde{\mathcal{M}}_{V_1\ldots V_n}$ denotes the finite part of the total matrix element that is not proportional to the Born matrix element $\mathcal{M}^{\mathcal{B}}_{V_1\ldots V_n}$. $C_F = 4/3$ is the Casimir operator of the color structure, c_{virt} is the constant of proportionality for the finite part proportional to $\mathcal{M}^{\mathcal{B}}_{V_1\ldots V_n}$ and A and B are the constants of proportionality for the divergent parts of $\mathcal{M}_{V_1\ldots V_n}$. For VBF processes, these constants are

$$A = -2 \quad \text{and} \quad B = -\frac{10 - D}{2}. \tag{3.59}$$

Here, $Q_i^2 = -(p_{q_i}^{out} - p_{q_i}^{in})^2$ is minus the momentum squared transferred between the initial and the final state of the quark line. In this work, the renormalization scale of quark line i is chosen to be $\mu_{Ri} = Q_i \equiv \sqrt{Q_i^2}$ and the DRED scheme is used, which means that $D = 4$ in equation (3.59) and we obtain $B = -3$ and $c_{virt}^{DRED} = \frac{\pi^2}{3} - 7$.
In DREG, $D = 4 - 2\epsilon$ and one obtains a new finite term in equation (3.58). This term can be absorbed in c_{virt}, which leads to

$$c_{virt}^{DREG} = c_{virt}^{DRED} - 1 = \frac{\pi^2}{3} - 8. \tag{3.60}$$

This is not inconsistent since this change is compensated in the real emission contribution such that

$$c_{real}^{DREG} = c_{real}^{DRED} + 1 = -\frac{2\pi^2}{3} + \frac{7}{2}, \tag{3.61}$$

and only the sum $c_{virt} + c_{real}$ is fixed. This points out the necessity to be consistent in the calculation of both, the real and the virtual corrections. Since the DRED scheme will be used throughout this work the index $DRED$ will be omitted for the sake of clarity, which means that in the following $c_{virt} \equiv c_{virt}^{DRED}$.

3.6.3. Subtraction of Born-types

After canceling the singularities against the $\boldsymbol{I}$ operator, the vertex corrections are proportional to the corresponding Born diagram and one can set $\widetilde{\mathcal{M}}_{V_i} \equiv 0$, which defines the value of c_{virt}. A significant fraction of the total finite part of the *Box*- and *Penline* corrections

$$\mathcal{M}^{fin}_{V_1 \ldots V_n} \equiv \widetilde{\mathcal{M}}_{V_1 \ldots V_n} + c_{virt} \cdot \mathcal{M}^{\mathcal{B}}_{V_1 \ldots V_n}, \tag{3.62}$$

are the Born-type contributions, $c_{virt} \cdot \mathcal{M}^{\mathcal{B}}_{V_1 \ldots V_n}$. A trick is to reduce the *Box*- and *Penline* contributions by shifting these Born-types to a different iteration and integrate the smaller finite matrix elements

$$\widetilde{\mathcal{M}}^{fin}_{VV} = \underbrace{\mathcal{M}^{fin}_{VV} - c_{virt} * \mathcal{M}^{\mathcal{B}}_{VV}}_{small} = \widetilde{\mathcal{M}}_{VV}, \tag{3.63}$$

$$\widetilde{\mathcal{M}}^{fin}_{VVV} = \underbrace{\mathcal{M}^{fin}_{VVV} - c_{virt} * \mathcal{M}^{\mathcal{B}}_{VVV}}_{small} = \widetilde{\mathcal{M}}_{VVV}. \tag{3.64}$$

The advantage of these smaller quantities is that one can achieve a higher absolute precision a lot faster in a Monte-Carlo integration. It has been checked that the resulting quantities are indeed very small.

Of course we need to add back the terms we have subtracted. Since

$$\widetilde{\mathcal{M}}_V = c_{virt} * \mathcal{M}^{\mathcal{B}}_V, \tag{3.65}$$

one can put all remaining terms together and one obtains

$$c_{virt} * \left(\mathcal{M}^{\mathcal{B}}_V + \mathcal{M}^{\mathcal{B}}_{VV} + \mathcal{M}^{\mathcal{B}}_{VVV}\right) = c_{virt} * \mathcal{M}^{\mathcal{B}}_{Tot}, \tag{3.66}$$

which can be calculated by simply calculating $\mathcal{M}^{\mathcal{B}}_{Tot}$ and multiplying it by c_{virt}. This trick saves a significant amount of CPU time.

3.7. Anomalous couplings

In the implementation of anomalous couplings, the crucial point are the new leptonic tensors. For their calculation, a new file called **towa_anomal.F** was created. The routines in this file were renamed e.g. from **vwptowma** to **vwptowma_anomal**. In the first step, the routines contained only the same code as the corresponding ones in **towa.F**, which were created with MadGraph [41]. In the second step, all HELAS routines for gauge boson self couplings had to be replaced by the HELAS routines with anomalous couplings. For example, the routine **VVVXXX(...)** was replaced with **wwa_anomal3(...)**. Since the anomalous couplings modify only triple and quartic gauge boson couplings, only the routines containing three or four vector bosons had to be modified.
Moreover, the anomalous couplings give rise to new vertices, e.g. $\gamma\gamma H$ and $Z\gamma H$ as depicted in figure 3.11. This yields a new contribution to the $W\gamma \to W\gamma$ and the $WZ \to W\gamma$ tensor.

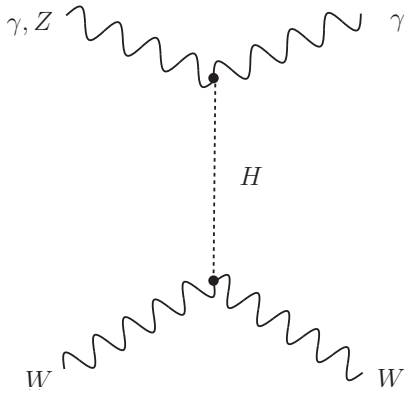

Figure 3.11: The anomalous gauge boson couplings give rise to the topology depicted above. These diagrams are not allowed in the Standard Model but have to be included in the leptonic tensor calculation when anomalous couplings are used.

Because of those additional Feynman diagrams, it can be necessary to add more channels to the phase space generator. But since for $W^{\pm}\gamma jj$ production via VBF the additional Higgs propagator only occurs in the t-channel, no additional channels are needed.

CHAPTER 4

CHECKS

In order to assure the correctness of the implementation of the $W^{\pm}\gamma jj$ VBF production process into VBFNLO a variety of checks have been performed.

4.1. Matrix elements

When calculating the matrix elements for the leading order and the real emission, it is possible to check them against an independent calculation for individual phase space points. The program MadGraph [41] was used to generate independent code for the calculation of the matrix element for each flavor combination. The agreement between our and the MadGraph results is on the order of 9 to 14 digits.

4.2. Cross sections

After making sure that the matrix elements are correct, still, the total cross sections remains to be checked. For this purpose, the Monte Carlo event generator Sherpa [42] was used. Since for vector boson fusion processes the t-channel contributions are very much dominant once VBF cuts are applied, the s-channel contributions were not implemented into VBFNLO [8] as shown in 2.6.1. However, Sherpa does calculate all possible contributions including interferences of t- and u-channel diagrams, which are also not included in our calculation. The VBF cuts were applied to keep non t-channel contributions small as described in section 2.6.1. The input parameters are listed in table 4.1.

- Proton-proton collider, $E_{cm} = 14$ TeV
- PDFs: CTEQ6l1 [24]
- $\mu_{Fi} = \mu_{Ri} = m_Z = 91.1876$ GeV
- VBF cuts on tagging jets
  - $|\eta_{j_1} - \eta_{j_2}| > 4, \quad \eta_{j_1} \times \eta_{j_2} < 0, \quad m_{j_1 j_2} > 600\,\text{GeV}$

- Inclusive cuts
  - jets: $p_T^j > 30\,\text{GeV}, \quad |\eta_j| < 4.5, \quad \Delta R_{jj} > 0.4$
  - leptons: $p_{T,l} > 20\,\text{GeV}, \quad |\eta_{l,\gamma}| < 2.5, \quad \Delta R_{j\,l} > 0.4$
  - photons: $p_{T,\gamma} > 30\,\text{GeV}, \quad \Delta R_{j\,\gamma} > 0.7, \quad \Delta R_{l\,\gamma} > 0.4$

Table 4.1: This table gives the setup that was used for the comparison with SHERPA.

The results of VBFNLO and SHERPA for the leading order ($W^{\pm}\gamma jj$) cross section are listed in table 4.2.

Process	VBFNLO σ [fb]	SHERPA σ [fb]	Deviation
$W^+\gamma jj$	8.152 ± 0.006	8.140 ± 0.017	0.16%
$W^-\gamma jj$	4.636 ± 0.003	4.632 ± 0.007	0.09%

Table 4.2: This table gives the LO $W^{\pm}\gamma jj$ cross sections calculated by VBFNLO and SHERPA.

The agreement that was found is on the order of one per mille for both processes. The results for the comparison of the leading order ($W^{\pm}\gamma jjj$) cross section are shown in table 4.3.

Process	VBFNLO σ [fb]	SHERPA σ [fb]	Deviation
$W^+\gamma jjj$	2.057 ± 0.003	2.088 ± 0.002	-1.49 %
$W^-\gamma jjj$	1.088 ± 0.001	1.132 ± 0.001	-3.94 %

Table 4.3: This table shows the 3 jet LO ($W^{\pm}\gamma jjj$) cross sections calculated by VBFNLO and SHERPA.

Here, we can see that our results deviate significantly from the SHERPA results. The reason for this are mainly the s-channel contributions depicted in figure 2.10, which are included in SHERPA but not in VBFNLO and can pass the VBF cuts in some phase space regions. In order to examine these s-channel contributions, they were calculated with SHERPA using the setup given in table 4.1. The results can be found in table 4.4 and 4.5 for $W^+\gamma jjj$ and $W^-\gamma jjj$ production respectively.

Process	SHERPA σ [fb]
$W^+\gamma(W^-)^* j;\ (W^-)^* \to jj$	$(2.743 \pm 0.004) \cdot 10^{-2}$
$W^+\gamma Z^* j;\ Z^* \to jj$	$(1.172 \pm 0.002) \cdot 10^{-2}$
$W^+\gamma\gamma^* j;\ \gamma^* \to jj$	$(5.583 \pm 0.007) \cdot 10^{-5}$

Table 4.4: In this table we present the cross sections for the three different s-channel contributions to $W^+\gamma jjj$ production calculated by SHERPA.

Process	SHERPA σ [fb]
$W^-\gamma(W^+)^*j;\ (W^+)^* \to jj$	$(3.964 \pm 0.009) \cdot 10^{-2}$
$W^-\gamma Z^*j;\ Z^* \to jj$	$(6.536 \pm 0.007) \cdot 10^{-3}$
$W^-\gamma\gamma^*j;\ \gamma^* \to jj$	$(1.653 \pm 0.002) \cdot 10^{-5}$

Table 4.5: This table gives the corresponding s-channel contributions to $W^+\gamma jjj$ production.

The s-channel contributions are on the order of a few percent of the full cross section. A s-channel W^+ boson decaying into two jets is enhanced by the PDFs over a W^- boson. This explains why the deviation is larger for the $W^-\gamma jjj$ case. The $\Delta R_{jj} > 0.4$ cut has the same effect as imposing a lower cut on the invariant mass of the two s-channel jets. This is why the photon channel is strongly suppressed here.

When we subtract the s-channel contributions from the whole SHERPA results we can compare this again to the VBFNLO results.

Process	VBFNLO σ [fb]	SHERPA σ [fb] without s-channel	Deviation
$W^+\gamma jjj$	2.057 ± 0.003	2.049 ± 0.002	-0.40 %
$W^-\gamma jjj$	1.088 ± 0.001	1.086 ± 0.001	-0.15 %

Table 4.6: In this table we subtracted the s-channel contributions from the SHERPA cross sections.

In table 4.6 one can see that both results agree within the Monte-Carlo errors. This proofs that the deviation originates from neglecting s-channel diagrams in VBFNLO and that our calculation is correct.

4.3. Dipoles

Since the dipole subtraction described in section 3.5.1 is done at the level of the matrix elements squared, one can compare the real emission matrix element $|\mathcal{M}_{RE}|^2$ to the subtraction term $|\mathcal{M}_{sub}|^2$ by taking the ratio $|\mathcal{M}_{sub}|^2/|\mathcal{M}_{RE}|^2$ for individual phase space points. Then, this ratio was plotted over $p_q \cdot p_g$ for the collinear limit and over E_g for the soft limit. Here p_q and p_g denote the 4-momenta of the gluon and a quark, respectively and E_g is the energy of the gluon. The ratio $|\mathcal{M}_{sub}|^2/|\mathcal{M}_{RE}|^2$ is expected to converge to 1 with $p_q \cdot p_g$ or E_g going to zero, respectively. One has to distinguish between final state gluons, depicted in figure 4.1, and initial state gluons (figure 4.2). The convergence is very good in all three cases. This shows that the dipole subtraction method works very well.

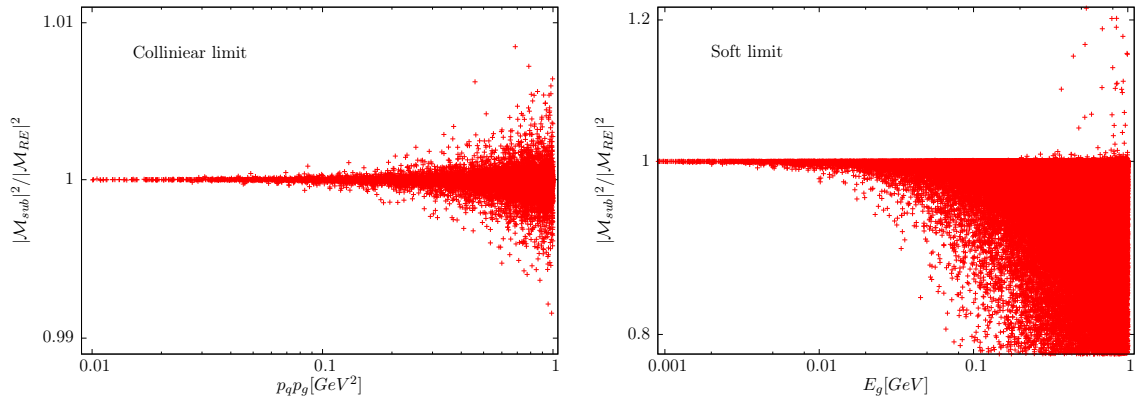

Figure 4.1: Final state gluons: The left plot shows the collinear limit for a quark and the gluon. On the right the soft limit is plotted.

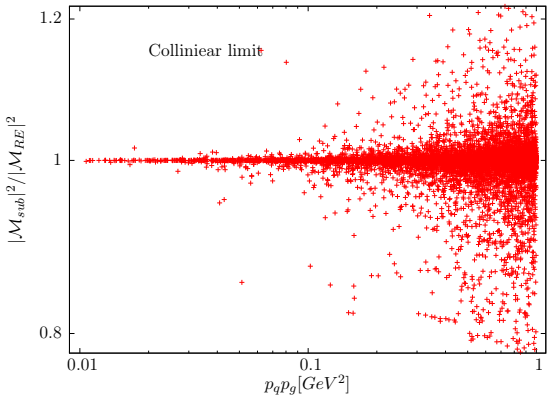

Figure 4.2: Initial state gluons: This plot shows the collinear limit of a quark and the initial state gluon. Note that there are no soft initial state gluons.

4.4. Gauge tests

As explained in section 2.2, the standard model is a gauge theory. A direct consequence of this is that the full matrix element with at least one external gauge boson vanishes, if the polarization vector of the gauge boson is replaced by its momentum (see equation (2.45))

$$\epsilon_\mu \mathcal{M}^\mu \quad \rightarrow \quad p_\mu \mathcal{M}^\mu = 0. \tag{4.1}$$

This is called gauge invariance and it is very important not to violate gauge invariance when doing approximations.

4.4.1. Leading order

To perform the gauge test for the leading order, we use a normalized replacement

$$\epsilon^\gamma_\mu \mathcal{M}^\mu_{\mathcal{B}} \equiv \mathcal{M}_{Born} \quad \rightarrow \quad \frac{p^\gamma_\mu}{E_\gamma} \mathcal{M}^\mu_{\mathcal{B}} \equiv \mathcal{M}^{gauge}_{Born}. \tag{4.2}$$

The division by E_γ is done due to numerical reasons. The values of the photon momenta in GeV are rather large compared to the photon polarization vector. After this replacement, the matrix element $\mathcal{M}^{gauge}_{Born}$ is significantly smaller than before. The histogram of

$$log_{10}\left(|\mathcal{M}^{gauge}_{Born}/\mathcal{M}_{Born}|\right) \tag{4.3}$$

was made to demonstrate this and can be found in figure 4.3.

As described in section 3.2.2 we calculate the matrix element for four flavor combinations for each phase space point. For the filling of the histogram, only the worst of these four results has been taken. Thus the satisfaction of the gauge test is on average better than in the following figures (4.3, 4.4, 4.6, 4.7).

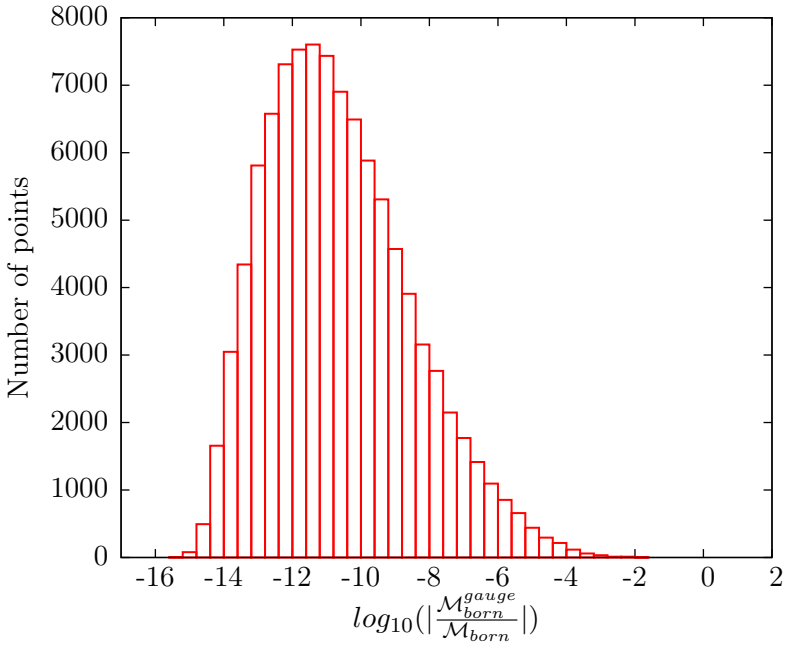

Figure 4.3: This is a histogram of the results of the gauge test for the leading order matrix element. For each phase space point, one obtains a different result for each flavor combination. Note that the histogram is always filled with the largest of those values.

Figure 4.3 shows that $|\mathcal{M}^{gauge}_{Born}|$ is usually between 8 and 14 orders of magnitude smaller than $|\mathcal{M}_{Born}|$. This means that gauge invariance is also satisfied numerically.

4.4.2. Real emission

In the case of the real emission, there are two external massless gauge bosons, the photon and the gluon. The gauge test can be performed for either of them separately. The results for both cases are depicted in figure 4.4.

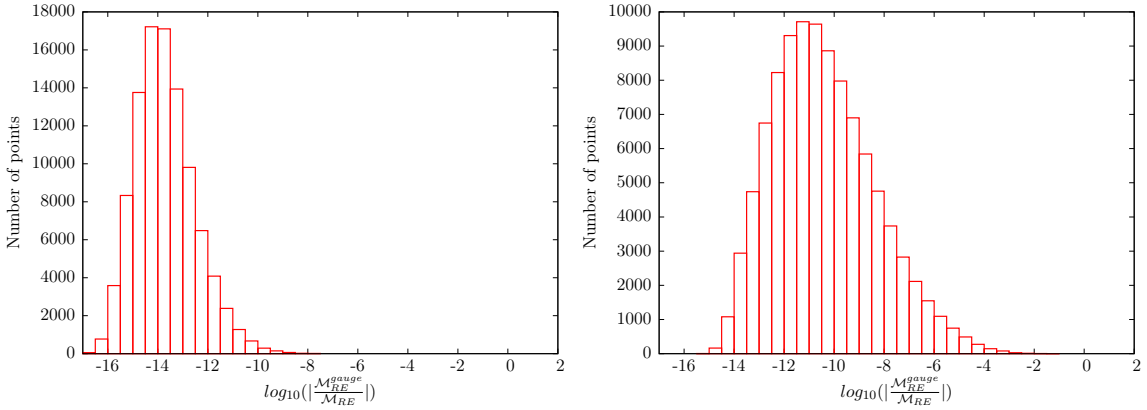

Figure 4.4: These two plots show histograms of the results of the gauge tests for the real emission matrix element. The plot on the left hand side shows the result for the gluon gauge test and the plot on the right shows the result for the photon gauge test.

Again the matrix elements are numerically consistent with zero after replacing one of the massless gauge boson with its 'normalized' momentum.

4.4.3. Virtual corrections

Here we exploit the fact that several diagrams are gauge related. This means that in general a single diagram is not gauge invariant by itself but the sum of all diagrams contributing to the matrix element is gauge invariant. In the case of $W\gamma$ production via vector boson fusion, the topologies depicted in figure 4.5 are gauge related.

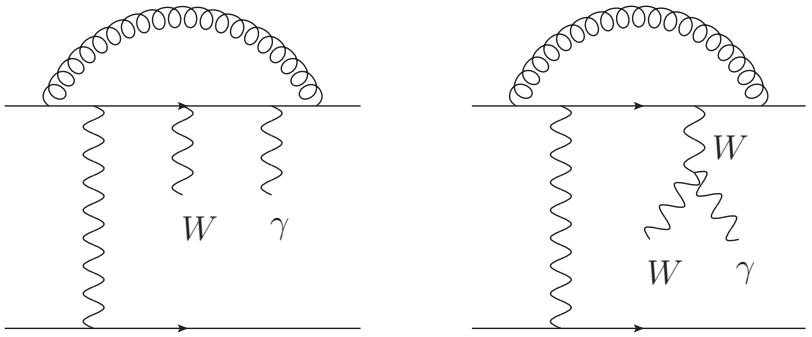

Figure 4.5: On the left, there is a pentagon diagram and on the right, a box diagram, in which the photon is radiated off the W boson. These two topologies are gauge related.

This relation allows us to check the relative signs between pentagon and box diagrams. The sign is correct if the virtual matrix element $\mathcal{M}_{virt}$ vanishes under the replacement

$$\epsilon_\mu^\gamma \mathcal{M}_{virt}^\mu \equiv \mathcal{M}_{virt} \quad \rightarrow \quad \frac{p_\mu^\gamma}{E_\gamma} \mathcal{M}_{virt}^\mu \equiv \mathcal{M}_{virt}^{Gauge}. \tag{4.4}$$

In order to check whether the gauge check works, we took the normalized quantity

$$log_{10}\left(|\mathcal{M}_{virt}^{gauge}/\mathcal{M}_{virt}|\right) \tag{4.5}$$

for 100,000 phase space points and made a histogram (left plots in figure 4.6 and 4.7). This approach can lead to numerical problems if $\mathcal{M}_{virt}$ is small.

Another approach to checking that $\mathcal{M}_{virt}^{gauge}$ is zero is to compare it to a part of itself. Since $\mathcal{M}_{virt}^{gauge} = \sum_i \mathcal{M}_{virt_i}^{gauge} = 0$, where i runs over all *Box*- and *Penline* contributions, one can subtract $\mathcal{M}_{virt_4}$ on both sides and then divide by it. After adding 1 on both sides and taking the logarithm, one obtains

$$log_{10}\left(\left|\frac{\mathcal{M}_{virt}^{gauge} - \mathcal{M}_{virt_4}^{gauge}}{\mathcal{M}_{virt_4}^{gauge}} + 1\right|\right). \tag{4.6}$$

$\mathcal{M}_{virt_4}$ corresponds to the topology on the right of figure 4.5, in which the photon is radiated off the W boson with a box correction to the upper line. The matrix element $\mathcal{M}_{virt_4}$ is usually rather big and therefore a good reference for comparing the size of $\mathcal{M}_{virt}^{gauge}$. The right plots in figure 4.6 and 4.7 show the quantity of equation (4.6).

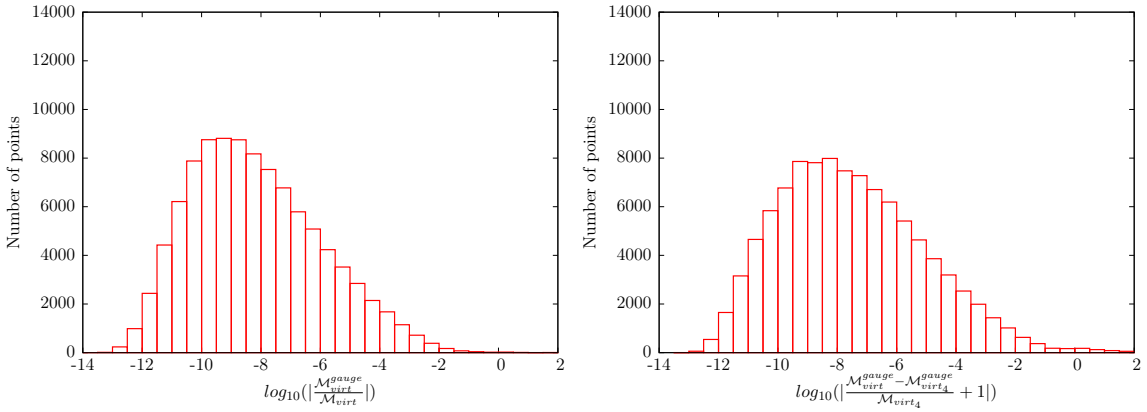

Figure 4.6: These two plots show histograms of the results of the gauge check. For these histograms, the internal Ward identity checks of the *Box*- and *Penlines* have not been applied.

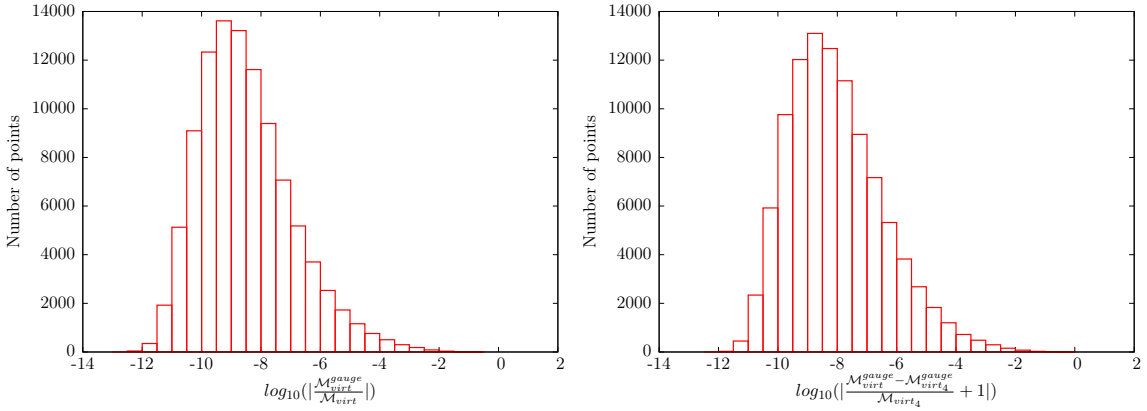

Figure 4.7: These two plots show again histograms of the result of the gauge check. But this time the internal Ward tests of the *Box*- and *Penlines* had to be passed, which eliminates the points close to zero. This shows that the internal Ward identity checks assure the conservation of gauge invariance.

For the plots in figure 4.6, the Ward identity test was not applied, which leads to violation of gauge invariance. For the plots in figure 4.7, we required that the Ward identity test is satisfied with a precision of $\epsilon = 10^{-2}$, which assures the conservation of gauge invariance. Moreover, the average of these histograms is shifted to the left, which represents a stronger satisfaction of the gauge test.

4.5. Virtual contributions

As described in section 3.6, the virtual contributions are calculated with the *Box*- and *Penline* functions created by Francisco Campanario [37]. The *Box*- and *Penline* routines provide a variety of possible checks.

4.5.1. Input

First of all, one has to assure that the input of these routines is correct. Since the *Box*- and *Penline* functions do not only calculate the matrix elements of the virtual contributions but also the Born ones, it is possible to check the output directly against the corresponding Born matrix element. The agreement was found to be on the order of $10^{-8} - 10^{-12}$ depending on the phase space points. This is well within the numerical accuracy.

4.5.2. Poles

The *Box-* and *Penline* routines are able to use the corresponding $1/\epsilon^i$ poles of the loop integrals to calculate the divergent parts of $\mathcal{M}_{V_1\dots V_n}$ in equation (3.58), which will be called $\mathcal{M}^{virt}_{V_1\dots V_n}(div = i)$ for $i = 1, 2$, respectively. This can be used to calculate the total matrix element using the *Box-* and *Penline* functions to numerically check the factorization of the poles given by equation (3.58) and (3.59)

$$\begin{aligned} \mathcal{M}^{virt}_{V_1\dots V_n}(div = 1) &= B * \mathcal{M}^{\mathcal{B}}_{V_1\dots V_n} = -3 * \mathcal{M}^{\mathcal{B}}_{V_1\dots V_n}, \\ \mathcal{M}^{virt}_{V_1\dots V_n}(div = 2) &= A * \mathcal{M}^{\mathcal{B}}_{V_1\dots V_n} = -2 * \mathcal{M}^{\mathcal{B}}_{V_1\dots V_n}. \end{aligned} \tag{4.7}$$

In figure 4.8, one can see the numerical precision of the factorization for 100,000 phase space points. For each of the phase space points, the normalized quantity

$$\left| \frac{\mathcal{M}^{virt}_{V_1\dots V_n}(div = i)}{const(i) * \mathcal{M}^{\mathcal{B}}_{V_1\dots V_n}} - 1 \right| \quad \text{with} \quad i = 1, 2 \quad \text{and} \quad const(i) = B, A, \tag{4.8}$$

has been calculated for each of the 4 channels in table 3.2. Then the log_{10} of these quantities was taken and the result was added to the corresponding histogram below.

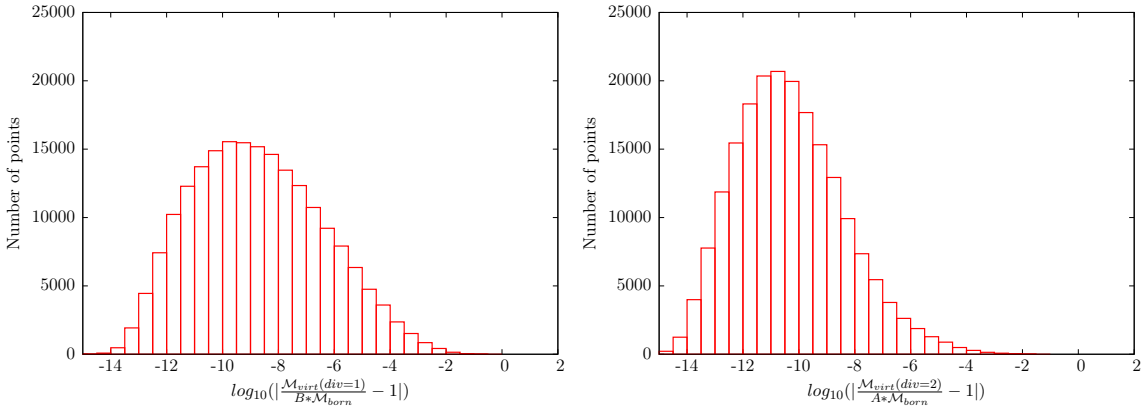

Figure 4.8: These two plots show histograms of the number of phase space points over the accuracy of the pole checks. The left plot represents the relation for the $1/\epsilon$ poles and the right one the relation for the $1/\epsilon^2$ poles. The numerical accuracy peaks at 10^{-10} for the $1/\epsilon$ poles and at 10^{-11} for the $1/\epsilon^2$ poles.

The accuracy is significantly better for the $1/\epsilon^2$ poles. The reason for this lies in the Passarino-Veltman tensor reduction, which is performed in the *Box-* and *Penlines*. There are less scalar integrals, and therefore less tensor integrals, that contribute to the $1/\epsilon$ poles than to the finite part and even less that contribute to the $1/\epsilon^2$ poles. The more integrals contribute with non-zero values, the more accuracy is lost through possibly small Gram determinants and thus the $1/\epsilon^2$ poles satisfy equation (4.7) better than the $1/\epsilon$ poles.

Equation (4.7) also holds, if the renormalization scale μ_{Ri} is chosen differently. This provides an additional possibility to check that the couplings of the individual diagrams and their summation have been implemented correctly.

4.5.3. Comparison with different implementation

Before the *Box-* and *Penline* functions were available in VBFNLO the loop corrections were calculated using an implementation by C. Oleari [43]. This implementation is able to calculate loop corrections to quark lines with massive gauge bosons or off-shell photons attached.
A final state photon as in $W^{\pm}\gamma$ production via VBF leads to an additional infrared divergence. This additional divergence could in principle change the factorization formula in equation (3.58).
However, it has been shown in [37] that this is not the case. Thus it was possible to check the results of the *Box-* and *Penlines* against the implementation by C. Oleari using the new scalar integrals. This was done at the level of the matrix elements $\mathcal{M}^{fin}_{V_1 \dots V_n}$. The agreement that was found was on the order of the numerical accuracy, which also confirms the correctness of the implementation of the *Box-* and *Penline* functions.

4.5.4. Dependence on intrinsic scale

We can use equation (3.58) for another check, which is described in [37] in more detail. Let's consider Q^2 as an independent energy scale and define it to be $Q^2 \equiv \mu_0$. Now, one can do a Taylor expansion of $(\mu_0)^{-\epsilon}$ in ϵ and one obtains a new finite term

$$\mathcal{M}'^{fin}_{V_1 \dots V_n} = \mathcal{M}^{fin}_{V_1 \dots V_n} + f(\mu_0) * \mathcal{M}_{\mathcal{B}} \quad \text{with} \quad f(\mu_0) = -B * \log(\mu_0) + \frac{1}{2} * A * \log^2(\mu_0). \tag{4.9}$$

The new quantity $\mathcal{M}'^{fin}_{V_1 \dots V_n}$ is now independent of the intrinsic scale μ_0 since the logarithms in $f(\mu_0)$ exactly cancel the log dependence of $\mathcal{M}^{fin}_{virt}$.

This can be checked by calculating equation (4.9) for a specific phase space point twice. The first time with the conventional choice of the intrinsic scale $\mu_0 = Q^2$ and the second time with $\mu_0 = 1$ GeV^2. Now the expression should be the same for both choices of the intrinsic scale μ_0. Once again this is satisfied within the numerical accuracy of 10 to 14 digits. This is a very strong check since it relates the calculation of the virtual corrections to the Born matrix element and directly checks the finite contributions.

4.5.5. Precision of the Ward test

The precision ϵ of the Ward identity test described in section 3.6.1 influences the number of phase space points that fail this check. It is important to check whether this affects the cross section of the virtual corrections. The share of unstable points in the *Boxlines* is very low, namely on the order of 10^{-6}, which is negligible for our purposes. Due to more Gram determinants we expect more instabilities with the *Penlines*, which will be investigated. Figure 4.9 shows the share of points that fail the Ward identity check over its precision.

With increasing precision of the Ward test, the share of points that fail the test rises significantly, which is expected. For the following calculations, the precision of the Ward test has been set to $\epsilon = 10^{-2}$. Actually, one needs to correct the result of the *Penlines* by the share of points that fail the Ward test. For $\epsilon = 10^{-2}$, the percentage of instabilities is 0.36%, so one has to multiply the pentagon cross section with a factor $1/(1 - 3.6 * 10^{-3}) \approx 1 + 3.6 * 10^{-3}$. Since the pentagons make up less than one percent of the total cross section this is completely negligible.

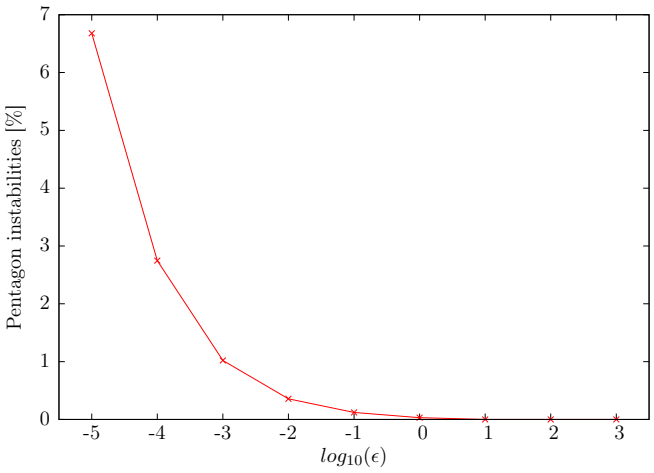

Figure 4.9: The share of phase space points identified as numerically unstable rises significantly with increasing precision of the Ward test.

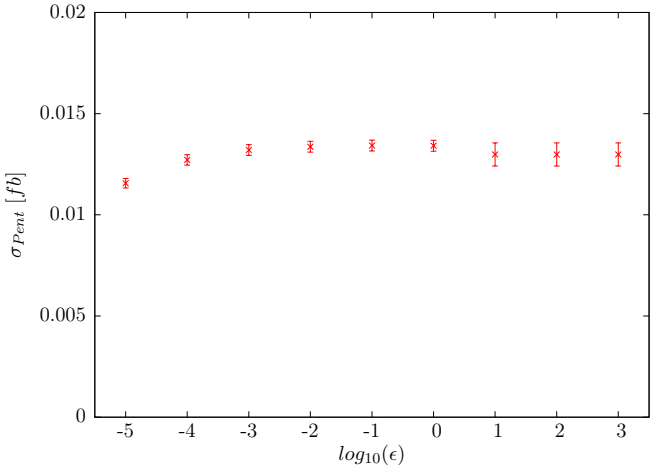

Figure 4.10: The precision of the Ward identity check affects the result of the *Penlines* only in the outer regions. This shows that $\epsilon = 10^{-2}$ is a reasonable choice for the precision of the Ward identity tests.

Figure 4.10 shows the result of the *Penlines* over the precision of the Ward identity test. For $\epsilon \in [10^{-3} : 10^{0}]$ the Pentagon cross section is stable within its errors. This means that the phase space regions that are removed by the rise of the precision do not contribute much to the cross section and therefore are kinematically suppressed. Thus the pentagons are very stable in this region. In the region $log_{10}(\epsilon) \geq 1$ the errors of the Pentagons become significantly larger since we are taking unstable phase space regions into account here. For $\epsilon < 10^{-3}$ the Ward identity tests are too strict and we loose too many phase space points, which lowers the pentagon cross section. This confirms that $\epsilon = 10^{-2}$ is a good choice.

4.6. Relation between real emission and virtual corrections

This check is based on the fact that it is possible to integrate terms proportional to $|\mathcal{M}_{\mathcal{B}}|^2$ either with the real emissions or the virtual corrections. The constants of proportionality are c_{real} and c_{virt} for the real emission and the virtual corrections, respectively. We take advantage of the fact that only the sum

$$c_{sum} = c_{real} + c_{virt} = \left(-\frac{2\pi^2}{3} + \frac{5}{2}\right) + \left(\frac{\pi^2}{3} - 7\right) = -\frac{\pi^2}{3} - \frac{9}{2}, \tag{4.10}$$

is fixed. c_{real} and c_{virt} can be varied but the NLO cross section should stay the same. This check relates the 6 particle phase space of the real emissions to the 5 particle phase space of the virtual corrections and is therefore very powerful. The results can be seen in table 4.7.

$W^+\gamma jj$

c_{real}	c_{virt}	c_{sum}	σ_{Real} [fb]	σ_{virt} [fb]	σ [fb]
$-\frac{2\pi^2}{3}+\frac{5}{2}$	$\frac{\pi^2}{3}-7$	$-\frac{\pi^2}{3}-\frac{9}{2}$	1.076 ± 0.010	6.746 ± 0.010	7.822 ± 0.014
$-\frac{\pi^2}{3}-\frac{19}{2}$	5	$-\frac{\pi^2}{3}-\frac{9}{2}$	-2.367 ± 0.013	10.180 ± 0.008	7.813 ± 0.015
$-\frac{\pi^2}{3}+\frac{1}{2}$	-5	$-\frac{\pi^2}{3}-\frac{9}{2}$	1.616 ± 0.029	6.221 ± 0.015	7.836 ± 0.033

$W^-\gamma jj$

c_{real}	c_{virt}	c_{sum}	σ_{Real} [fb]	σ_{virt} [fb]	σ [fb]
$-\frac{2\pi^2}{3}+\frac{5}{2}$	$\frac{\pi^2}{3}-7$	$-\frac{\pi^2}{3}-\frac{9}{2}$	0.621 ± 0.007	3.912 ± 0.005	4.533 ± 0.008
$-\frac{\pi^2}{3}-\frac{19}{2}$	5	$-\frac{\pi^2}{3}-\frac{9}{2}$	-1.397 ± 0.009	5.932 ± 0.005	4.535 ± 0.010
$-\frac{\pi^2}{3}+\frac{1}{2}$	-5	$-\frac{\pi^2}{3}-\frac{9}{2}$	0.937 ± 0.020	3.604 ± 0.009	4.542 ± 0.022

Table 4.7: This table gives the real emission, the virtual contributions and the total cross section for different values for c_{real} and c_{virt} while their sum c_{sum} is fixed.

The results agree within the numerical error of the Monte-Carlo. This confirms that the calculations of the finite parts of the real emission and the virtual contributions are correct.

4.7. Anomalous couplings

There are several possible checks for the implementation of anomalous gauge boson couplings. The Lorentz invariance and the comparison to other implementations have already been checked in the course of the diploma thesis of O. Schlimpert [44]. The only thing left to do in order to check the correctness of the implementation for a new processes is to switch on the anomalous couplings, set all of them to zero and compare the result to the one without anomalous couplings. Both results agree within the numerical accuracy of the Monte-Carlo.

CHAPTER 5

PHENOMENOLOGY

In this chapter, several phenomena will be examined starting with the differences between the LO and the NLO results, where the K-factor will be discussed. It will be shown that the scale dependence is significantly reduced by calculating the NLO QCD cross section. Then the energy dependence of the cross section will be shown briefly. We will discuss final state radiation, which is a phenomenon that occurs in processes with a charged lepton and a photon in the final state, as in $W^{\pm}\gamma jj$ production via weak boson scattering. Furthermore, different photon helicities and the effects of a jet veto will be examined. Finally, we will look at anomalous coupling effects.

5.1. Numerical results

Let us start with the numerical results for the LO and the NLO cross sections. The setup that was used here and in the following is given in table 5.1 and the cuts that we applied are given in table 5.2.

- Proton-proton collider, $E_{cm} = 14$ TeV
- PDFs: CTEQ6l1 [24] for LO and CT10 [25] for NLO calculation ($\alpha_S^{NLO}(m_W) = 0.120$)
- Jet definition: Anti-k_T algorithm [45]
- Scale of quark line i: $\mu_{F_i} = \mu_{R_i} = Q_i \equiv \sqrt{-(p_{q_i}^{out} - p_{q_i}^{in})^2}$
- Electroweak input parameters
  - $m_Z = 91.1876$ GeV
  - $m_W = 80.398$ GeV
  - $G_F = 1.16637 \cdot 10^{-5}$ GeV^{-2}
- Calculated electroweak parameters [1]
  - $\sin^2\Theta_W = 0.22264585$
  - $\Gamma_W = 2.097673$ GeV
  - $\alpha_{em} = 1/132.34070$
- All fermions occurring in this calculation are assumed to be massless.

Table 5.1: This table gives the setup that was used to obtain the results of this and the following analyses.

- VBF cuts on tagging jets
  - $|\eta_{j_1} - \eta_{j_2}| > 4, \quad \eta_{j_1} \times \eta_{j_2} < 0, \quad m_{j_1 j_2} > 600\text{GeV}$
- Inclusive cuts
  - jets: $p_T^j > 30\,\text{GeV}, \quad |\eta_j| < 4.5, \quad \Delta R_{jj} > 0.4$
  - leptons: $p_{T,l} > 20\,\text{GeV}, \quad |\eta_{l,\gamma}| < 2.5, \quad \Delta R_{j\,l} > 0.4$
  - photons: $p_{T,\gamma} > 30\,\text{GeV}, \quad \Delta R_{j\,\gamma} > 0.7, \quad \Delta R_{l\,\gamma} > 0.4$

Table 5.2: This table gives the cuts that were applied here and in the following calculations.

The numerical results for the LO and the NLO cross sections and the individual contributions given in table 5.3.

	$pp \to W^+\gamma jj$	$pp \to W^-\gamma jj$
σ_{LO} [fb]	$7.828 \pm 5 \cdot 10^{-3}$	$4.486 \pm 3 \cdot 10^{-3}$
$\sigma_{Born-types}$ [fb]	$6.750 \pm 5 \cdot 10^{-3}$	$3.934 \pm 3 \cdot 10^{-3}$
σ_{Box} [fb]	$(62.6 \pm 0.4) \cdot 10^{-3}$	$(12.7 \pm 0.2) \cdot 10^{-3}$
σ_{Pent} [fb]	$(12.2 \pm 0.7) \cdot 10^{-3}$	$(5.4 \pm 0.5) \cdot 10^{-3}$
σ_{Real} [fb]	$1.085 \pm 6 \cdot 10^{-3}$	$0.636 \pm 4 \cdot 10^{-3}$
σ_{NLO} [fb]	$7.910 \pm 7 \cdot 10^{-3}$	$4.588 \pm 5 \cdot 10^{-3}$
K-factor	1.013	1.021

Table 5.3: This table shows the numerical results for the LO and the NLO cross sections, the individual contributions and the K-factor.

Remember that the K-factor is defined as

$$K = \frac{\sigma_{NLO}}{\sigma_{LO}}. \tag{5.1}$$

The LO and the NLO cross section are close to each other, which is reflected in the K-factors that are very close to one. The reason for this is the scale choice of $\mu_{R_i} = \mu_{F_i} = Q_i$, where Q_i^2 is minus the square of the momentum transferred from quark line i to the EW process. The advantage of such a dynamical scale over a fixed scale such as for example the W mass m_W is that it adapts to the energy, which is present in the interaction and thus is a good fit in a large part of the phase space. The reason why the cross sections for $pp \to W^+\gamma jj$ are larger than for $pp \to W^-\gamma jj$ are the PDFs of the proton-proton collider, which enhance the production of positively charged final state particles.

The box and pentagon contributions, which already include the subtraction of $c_{virt} * \left|\mathcal{M}^B_{V_1 \ldots V_n}\right|^2$ are very small, so it is completely justified to evaluate them with lower statistics in the following. The dipoles were already subtracted from the real emission contribution, which also contains the finite collinear remainders. This contribution dominates the error of the total

[1] We use the three input parameters m_Z, m_W and G_F and the electroweak SM tree-level relations to determine all other relevant EW parameters.

cross section. For $c_{real} = -\frac{2\pi^2}{3} + \frac{5}{2}$ and $c_{virt} = \frac{\pi^2}{3} - 7$ the real emission accounts for 13.8% of the NLO cross sections. The s-channel contributions that we neglected (figure 2.10) were found to be approximately 1.5% for $W^+\gamma jjj$ production and 4% for $W^-\gamma jjj$ production (see section 4.2). Thus, the error that we make is on the order of a few per mille and well below the theoretical uncertainty, which we will see in section 5.2

5.2. Scale dependence

One of the key points of the motivation for calculating the NLO corrections was to reduce the scale dependence. The scale dependence of the cross section is usually taken to estimate the theoretical uncertainty of the calculation. The idea behind this approach is that the cross section must be independent of the factorization and renormalization scales if it was calculated to all orders of perturbation theory. But since we calculate only the order $\mathcal{O}(\alpha_{em}^5\alpha_S)$, our cross section will depend on these two unphysical scales. So, the higher orders must cancel this scale dependence and thus be on the same order of magnitude.
Therefore, the scale dependence of the cross section is a measure for the missing higher orders and thus for the theoretical error of the calculation. This is controversially discussed among theorists, since the choice of the scale and moreover, the choice of the interval, which is used to determine the scale variation, are almost completely arbitrary. Nevertheless, it can be seen as a lower limit for the theoretical error and thus gives us a feeling for the theoretical uncertainty.
The plots in figure 5.1 and 5.2 show the scale dependence of the leading order cross section, the next-to-leading-order cross section and all of its components for $W^+\gamma jj$ production. The NLO cross section depends on two different scales. Thus we can vary only the factorization scale μ_{Fi} (dotted blue lines), the renormalization scale μ_{Ri} (dashed green lines) or both scales together (solid red lines). The factorization scale is the energy scale of the PDFs and the renormalization scale describes the running of α_S, which affects all NLO diagrams and the NLO PDFs. The scale variation plots have been created for two different scales, namely $\mu_{0i} = Q_i$ and $\mu_{0i} = m_W$, that have been varied ($\xi\mu_{0i}$) over the interval $\xi \in [0.1, 10]$.

Figure 5.1 shows that the scale dependence of the next-to-leading-order cross section is significantly lower than the one of the leading order. Moreover, the scale dependence for the dynamical scale $\mu_{0i} = Q_i$ is lower than for the fixed scale $\mu_{0i} = m_W$. We can observe that the choice of the scale affects the total K-factor. Figure 5.2 shows that the scale variation of the real emission is negatively correlated with the scale variation of the Born-types. This decreases the scale dependence of the full NLO cross section. Again, the range of the scale variation is lower for $\mu_{0i} = Q_i$. We suspect that the scaling of the real emission is dominated by the gluon PDFs, whose scale behavior is depicted in figure 5.3. When one compares figure 5.3 to the scaling of the real emission in figure 5.2 one can see that the behavior is very similar. Thus it is likely that the initial state gluon channels make up a significant share of the real emission.

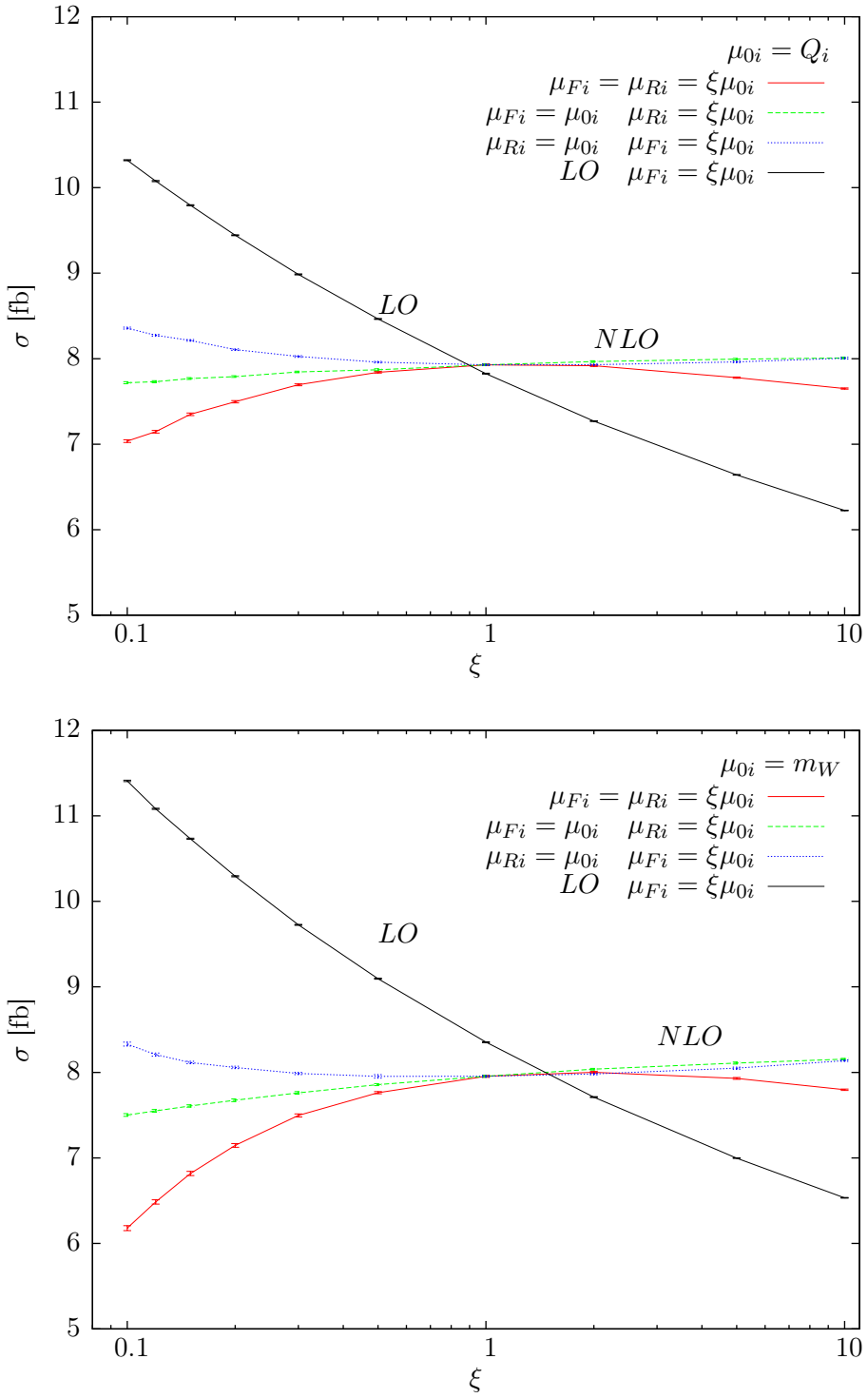

Figure 5.1: The upper plot shows the scale dependence of the cross section for $\mu_{0i} = Q_i$, the lower one for $\mu_{0i} = m_W$. Three different cases have been examined: variation of the renormalization scale μ_{Ri} (dashed green lines), variation of the factorization scale μ_{Fi} (dotted blue lines) and variation of both scales (solid red lines). The black line represents the leading order, which is only affected by the factorization scale.

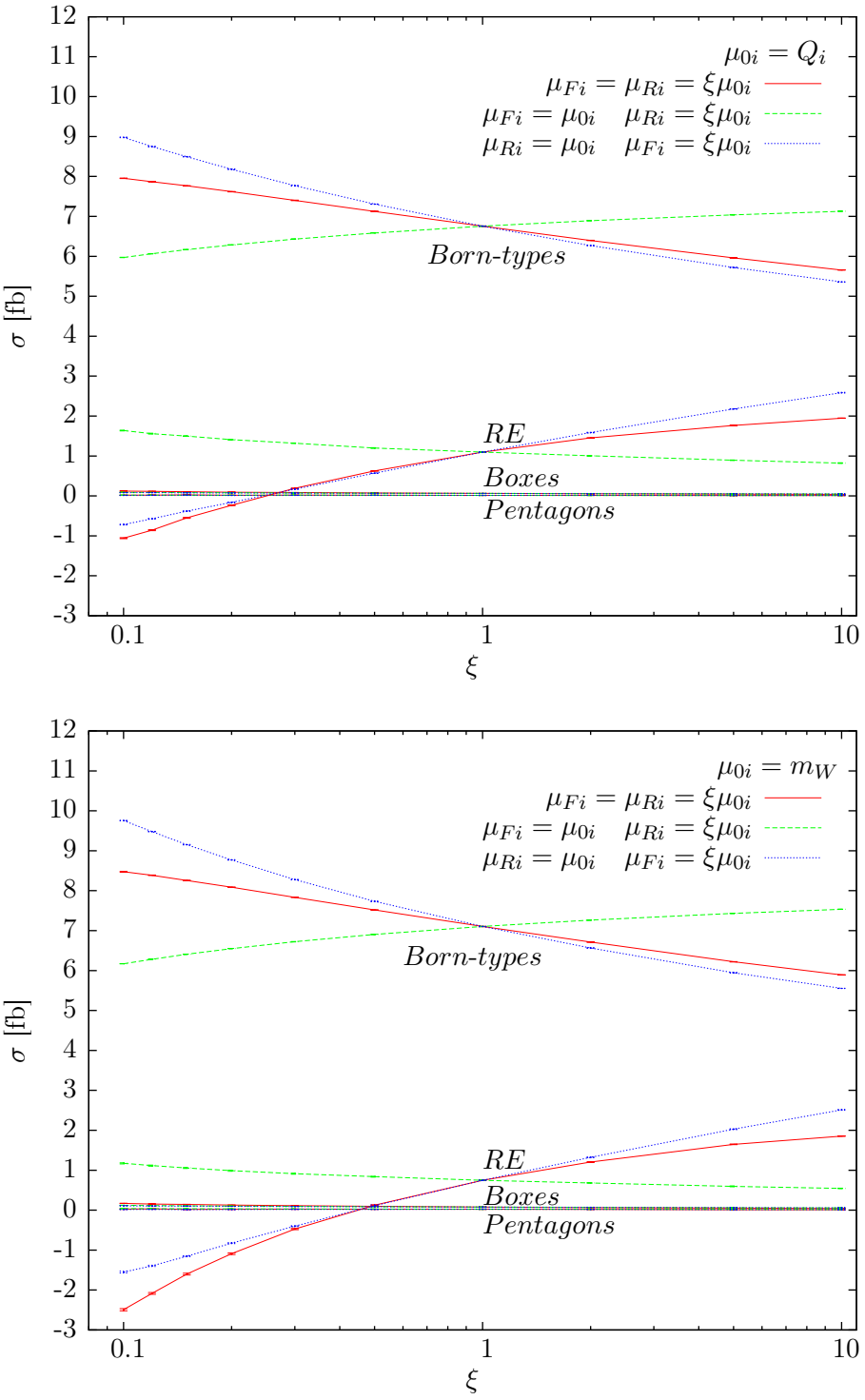

Figure 5.2: These two plots show the scale dependence of the remaining components. The colors are assigned as in figure 5.1. Boxes and pentagons represent the corresponding cross sections after the subtraction of c_{virt} times the corresponding born cross section as described in section 3.6.3. These contributions are included in the Born-types which also contain the vertex corrections. The real emission already includes the Catani-Seymour subtraction terms and the finite collinear remainders as described in section 3.5.1.

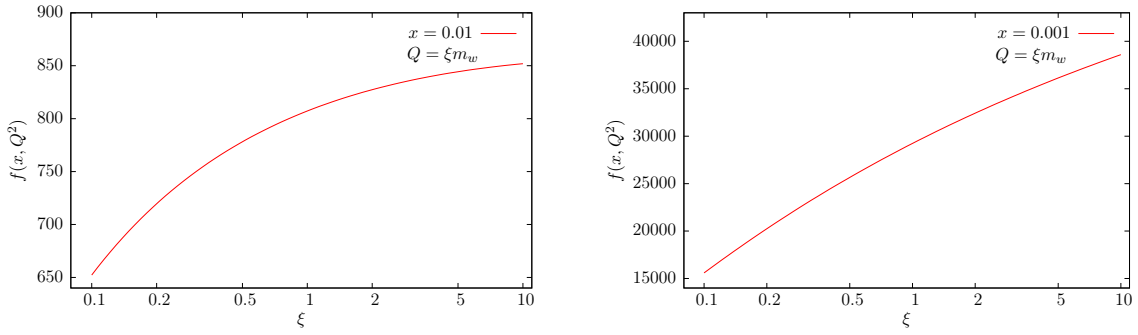

Figure 5.3: These two plots show the scaling of the gluon PDFs for $Q = \xi m_W$ and $\xi \in [0.1, 10]$.

To determine the theoretical uncertainty, one usually uses the scale variation in the interval $\xi \in [0.5, 2]$. Here, the maximum and the minimum cross section in this interval were taken since the cross sections for $\mu_{Ri} = \mu_{Fi} = 2^{\pm 1} Q_i$ are lower than the one for $\mu_{Ri} = \mu_{Fi} = Q_i$. The difference of the minimum and the maximum cross section defines the scale variation, which is given in table 5.4 for $\mu_{0i} = Q_i$.

$\mu_{0i} = Q_i$	σ [fb] at $\xi = 1$	Variation $\xi \in [0.5, 2]$ [fb]	Relative variation
LO	7.832 ± 0.005	1.19	15.2%
NLO	7.909 ± 0.012	0.13	1.7%

Table 5.4: This table shows the variation of the LO and the NLO cross sections for $\mu_{0i} = Q_i$.

The scale uncertainty of the cross section has been decreased from 15.2% to 1.7% by calculating the next-to-leading order. The corresponding scale variation for the fixed scale $\mu_{0i} = m_W$ are shown in table 5.5.

$\mu_{0i} = m_W$	σ [fb] at $\xi = 1$	Variation $\xi \in [0.5, 2]$ [fb]	Relative variation
LO	8.27 ± 0.006	1.37	16.6%
NLO	7.83 ± 0.012	0.28	3.6%

Table 5.5: This table gives the scale uncertainties for $\mu_{0i} = m_W$.

With this scale choice, the scale uncertainty decreases from 16.6% at leading order to 3.6% at next-to-leading order. This shows that the scale uncertainty actually depends on the scale we choose. Thus we can state that the scale dependence is only an estimation and not an exact value for the theoretical uncertainty of our calculation. The remaining scale uncertainty is partly due to the initial state gluon channels that arise in the real emission corrections at NLO. This channel is basically calculated at LO and has no virtual counterterm that could cancel its scale dependence.

So far, both scale choices are reasonable, since for $\xi = 1$ one is on the plateau of the NLO cross section as shown in figure 5.1. In the following, both, the renormalization and the factorization scale will be set to the absolute value of the momentum transferred from quark

line i to the EW process, $\mu_{Ri} = \mu_{Fi} = Q_i$, which is the common choice for vector boson fusion processes (see [33, 36]). Q_i^2 can be interpreted as a measure for the virtuality of the gauge boson emitted off quark line i and thus, it represents the kinematics of the process. This scale choice yields relatively flat differential K-factor distributions for most observables, which will be shown e.g. in figure 5.9.

Another point in favor of the dynamical scale Q_i is the reduced scale uncertainty as seen in tables 5.4 and 5.5. This is also observable in differential distributions. To demonstrate this, the following ratio needs to be defined

$$R(\mu_{0i}, \xi) \equiv \frac{d\sigma(\mu_{Ri} = \mu_{Fi} = \xi\mu_0)}{d\sigma(\mu_{Ri} = \mu_{Fi} = \mu_0)}. \tag{5.2}$$

In figure 5.4 this ratio is plotted over $p_T^{j_1}$ for the scales, $\mu_{0i} = Q_i$ and $\mu_{0i} = m_W$, and the canonical variations $\xi = 2^{\pm 1}$.

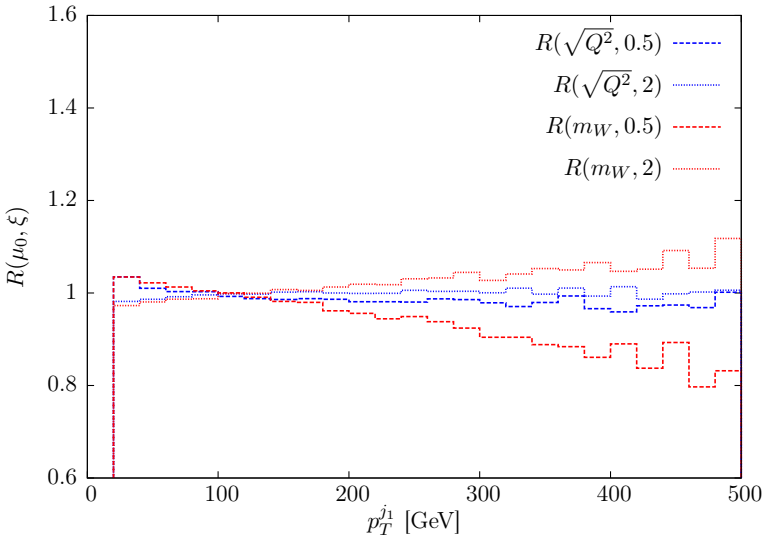

Figure 5.4: This plot shows the ratio defined in equation (5.2) for $\xi = 2^{\pm 1}$ and the two scales, $\mu_{0i} = Q_i$ and $\mu_{0i} = m_W$. For both scales the corresponding curves cross at $p_T^{j_1} \approx 120$ GeV.

The scale variation for $\mu_{0i} = Q_i$ is approximately constant over the whole range. But one can clearly see that above $p_T^{j_1} \approx 120$ GeV the spread between the curves for $R(m_W, 0.5)$ and $R(m_W, 2)$ widens with increasing $p_T^{j_1}$. Since the scale variation for $\xi = 2^{\pm 1}$ is used to determine the theoretical error in experimental analyses, the preferable scale choice is $\mu_{Ri} = \mu_{Fi} = Q_i$.

5.3. Energy dependence

In general, the cross section depends on the collider energy. To demonstrate this, the leading order and the next-to-leading-order cross sections were calculated for a range of collider energies and plotted in figure 5.5.

We can see that the LO and the NLO cross sections rise with increasing energy. The rising discrepancy between LO and NLO is caused by the application of the cut

$$\min(m_{j_1 j_3}, m_{j_2 j_3}) > 150 \text{ GeV}. \tag{5.3}$$

This cut was applied to remove the s-channel contributions described in section 2.6.1, which we do not include in our calculation. These contributions get larger at higher energies and therefore, we need this cut to remove them. This cut only affects the identified jets, namely well separated partons with $p_T > 30$ GeV.

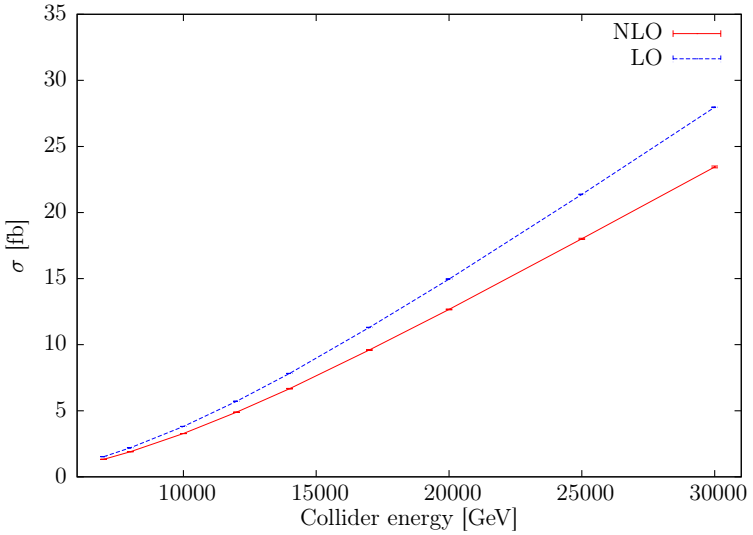

Figure 5.5: This plot shwos that the LO and the NLO cross sections for $W^+\gamma jj$ production rise with increasing energy. The increasing discrepancy between LO and NLO is due to the additional cut on $m_{j_i j_3}$ that is applied here.

5.4. LO vs NLO distributions

Here and in the following, the analysis will focus on the process $pp \to W^+\gamma jj$. The results for $pp \to W^-\gamma jj$ are very similar and therefore not presented.
To examine the differences between the leading order and the next-to leading order result, it is useful to look at differential distributions. Taking into account the cuts and input parameters given in table 5.1 and 5.2, respectively, the total K-factor for $W^+\gamma jj$ production is very close to one, namely $K \approx 1.01$. However, differences between LO and NLO results are in general not just a constant factor, i.e. a rescaling of the differential distribution by the K-factor of the integrated cross section can lead to under- or overestimating the NLO corrections in different phase space regions. This can be observed in the differential distribution of the leading jet $d\sigma/dp_T^{j_1}$ and its differential K-factor distribution $K_\partial(p_T^{j_1})$ shown in figure 5.6. The differential K-factor of an observable $\mathcal{O}$ is defined as

$$K_\partial(\mathcal{O}) = \frac{d\sigma_{NLO}}{d\mathcal{O}} \left(\frac{d\sigma_{LO}}{d\mathcal{O}}\right)^{-1} . \tag{5.4}$$

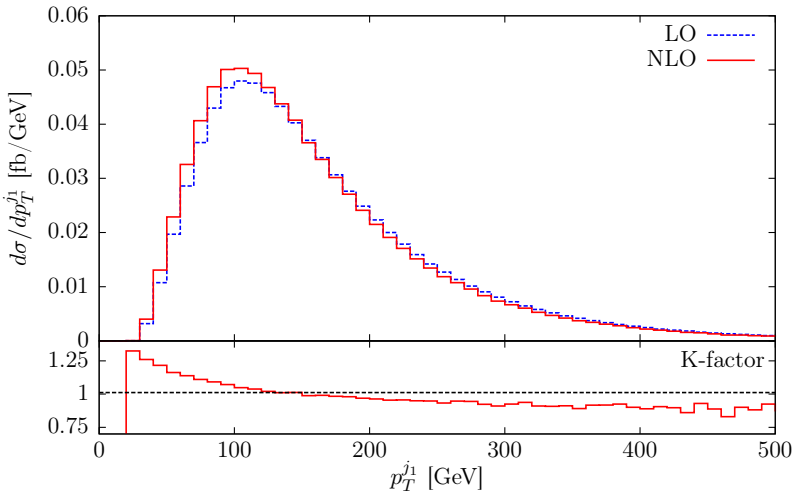

Figure 5.6: This plot shows the transverse momentum distribution of the hardest jet $d\sigma/dp_T^{j_1}$. In the region below $p_T^{j_1} \approx 150$ GeV, the NLO result (solid red line) is larger than the LO result (dashed blue line). For high $p_T^{j_1}$, it is the exact opposite. This is reflected in the decrease of the differential K-factor in the lower part of the plot where the dashed line represents the total K-factor of the integrated cross section for the cuts listed in appendix.

In figure 5.6 We can see that the LO result is smaller for low $p_T^{j_1}$, which is reflected in the K-factor that is greater than one for $p_T^{j_1} \lesssim 150$ GeV and smaller than one for $p_T^{j_1} \gtrsim 150$ GeV.

A distribution that shows a similar behavior is the invariant mass distribution of the tagging jets $d\sigma/dm_{j_1j_2}$ depicted in figure 5.7.

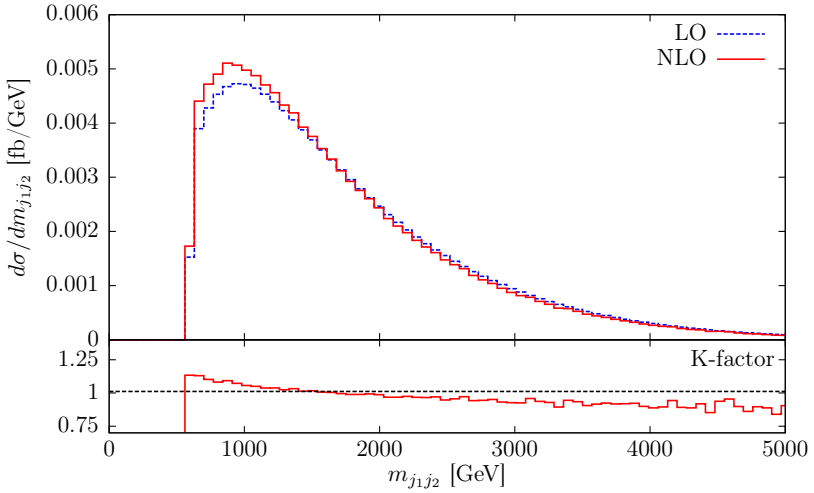

Figure 5.7: The invariant mass distribution of the tagging jets $d\sigma/dm_{j_1j_2}$ shows a crossing of the LO and the NLO results. The K-factor is larger than one in the region where $m_{j_1j_2} \lesssim 1500$ GeV is small and lower than one for $m_{j_1j_2} \gtrsim 1500$ GeV.

Again, the K-factor is above 1 for small $m_{j_1j_2}$ values and decreases with rising $m_{j_1j_2}$. Since the differential K-factor is not flat in general, one can conclude that it is not possible to obtain NLO distributions from LO ones by multiplying them with a total K-factor.

5.5. Final state radiation

Final state radiation occurs in processes with a final state photon and another gauge boson that decays into charged particles. In those processes, the photon can be radiated off the final state decay leptons as depicted in figure 5.8. This is called final state radiation or Bremsstrahlung.

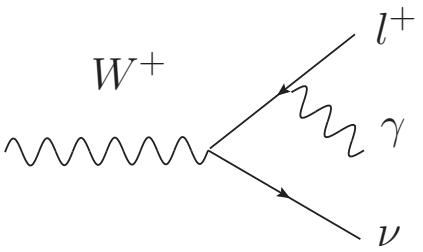

Figure 5.8: In processes with photons and charged leptons in the final state, the photon can be radiated off the lepton. This is called final state radiation.

The coupling of the photon to the lepton is a simple QED coupling and those couplings have been measured with very high accuracy. We want to examine anomalous effects in triple and quartic gauge boson couplings. Therefore, we want to suppress the final state radiation to increase the sensitivity to anomalous gauge boson couplings.

For this purpose, one can introduce a cut on the transverse mass cluster of the $W\gamma$ system [46]

$$m_T(W\gamma) = \left(\left[(m_{l\gamma}^2 + p_{T_{l\gamma}}^2)^{\frac{1}{2}} + \not{p}_T \right]^2 - (\boldsymbol{p_{T l\gamma}} + \not{\boldsymbol{p}}_{\boldsymbol{T}})^2 \right)^{\frac{1}{2}}. \tag{5.5}$$

Here, $m_{l\gamma}$ and $p_{T_{l\gamma}}$ are the invariant mass and the transverse momentum of the $l\gamma$ system respectively. $\not{p}_T$ denotes the missing transverse momentum, which corresponds to the transverse momentum of the neutrino.
The differential cross section plotted over $m_T(W\gamma)$ shows a final state radiation peak at m_W.

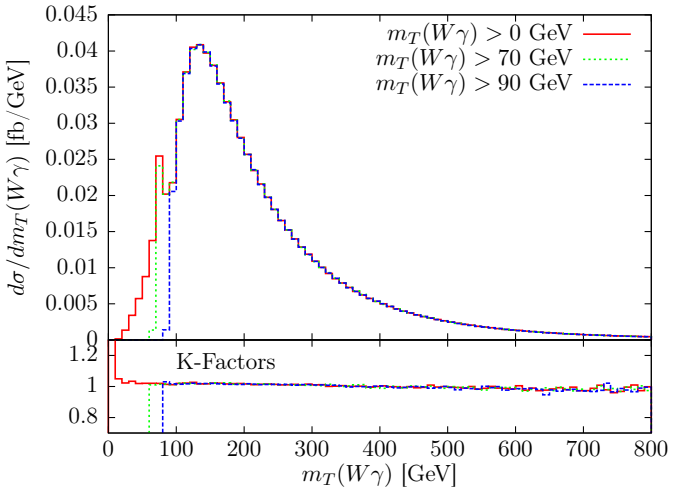

Figure 5.9: This plot shows the differential cross section over the transverse mass cluster of the $W\gamma$ system. The cut $m_T(W\gamma) > 70$ GeV does not remove the final state radiation peak at m_W yet, but $m_T(W\gamma) > 90$ GeV does.

Figure 5.9 demonstrates that this peak can be removed with the cut $m_T(W\gamma)$ >90 GeV. Table 5.6 shows that this cut reduces the total cross section only by approximately 10%.

$m_T(W\gamma)_{min}$	σ_{NLO} [fb]	Deviation	K-Factor
0 GeV	7.916 ± 0.005	0.0%	1.01
70 GeV	7.593 ± 0.005	-4.1%	1.01
90 GeV	7.133 ± 0.005	-9.9%	1.01

Table 5.6: This table shows the effect of the $m_T(W\gamma)$ on the NLO QCD cross section and the K-factor.

Another distribution, in which final state radiation is observable, is the $R_{l\gamma}$ distribution. The peak at low $R_{l\gamma}$ that is observable in figure 5.10 is caused by final state radiation. It can be reduced significantly by applying the cut on $m_T(W\gamma)$. Without the $R_{l\gamma} > 0.4$ cut the cross section would be logarithmically divergent for $R_{l\gamma} \to 0$. The peak at $R_{l\gamma} = \pi$ is the back-to-back peak. It arises from back-to-back $W\gamma$ scattering, which is enhanced by the phase space. The two peaks in figure 5.10 are dominated by different helicities, which will be examined in section 5.6.

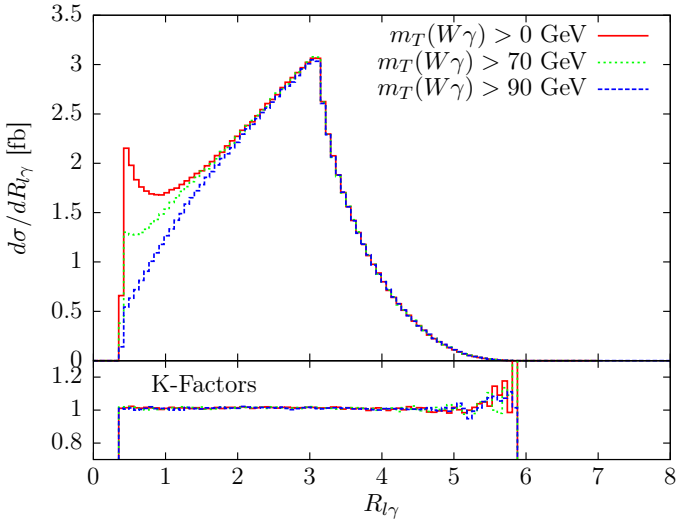

Figure 5.10: This plot of the different cross section over the R-separation of lepton and photon shows an interesting behavior. The peak for small $R_{l\gamma}$ becomes smaller the larger the cut on $m_T(W\gamma)$ gets. This means that the majority of final state radiation is emitted in a small cone around the lepton.

5.6. Helicity correlations

For final state photon processes, it is interesting to look at different photon helicities, since in some distributions of differential cross sections one can see, that different regions are dominated by different helicities. The reason for this are helicity correlations that arise from the fermion chirality conservation in the vertices.

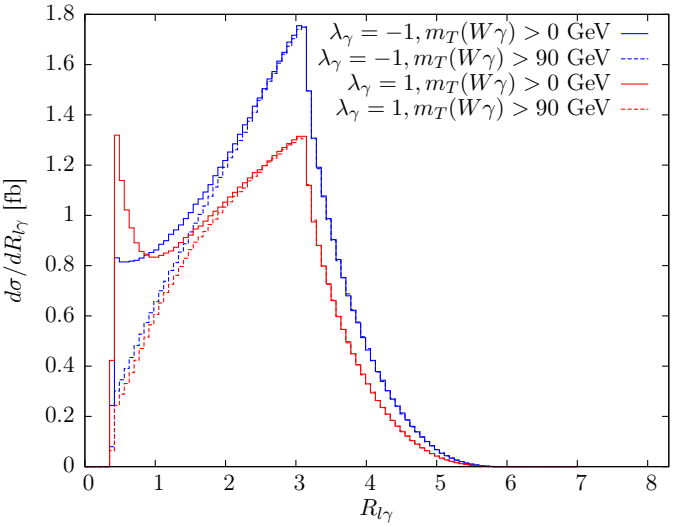

Figure 5.11: This plot shows the $R_{l\gamma}$ distribution for the two helicities separately. The red lines represent the right-handed photons ($\lambda_\gamma = 1$) and the blue lines the left-handed ones ($\lambda_\gamma = -1$). The final state radiation peak at small $R_{l\gamma}$ is clearly dominated by right-handed photons. By applying the cut $m_T(W\gamma) > 90$ GeV this peak can be removed completely (dashed lines).

The $R_{l\gamma}$ distribution in figure 5.11 shows a back-to-back peak at $R_{l\gamma} \approx \pi$ for both photon helicities. The final state radiation peak at $R_{l\gamma} \approx 0.5$ is dominated by right-handed photons.

In the $\Phi_{l\gamma}$ distribution in figure 5.12 one can see back-to-back peaks for both helicities and again, that the back-to-back region is dominated by left-handed photons. This distribution shows final state radiation peaks for both helicities, which are removed by the $m_T(W\gamma) > 90$ GeV cut.

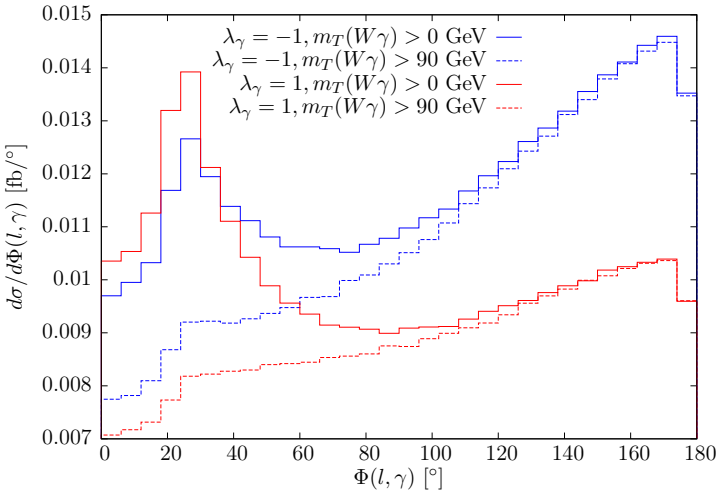

Figure 5.12: The differential cross section over the azimuthal angle between photon and lepton $\Phi_{l\gamma}$ shows two different phenomena. The region of large $\Phi_{l\gamma}$ is dominated by left-handed photons, which one can also see in the $d\sigma/dR_{l\gamma}$ plot in figure 5.11. We can observe final state radiation peaks at small $\Phi_{l\gamma}$ for both helicities, which are removed by applying the $m_T(W\gamma) > 90$ GeV cut. The labeling is analogous to figure 5.11.

5.7. Jet veto

At next-to-leading order an additional parton emerges from the real emission contribution. This additional parton can be identified as a jet if it is well separated from the other partons and has a minimum transverse momentum $p_T^j > 30$ GeV. In this work, the anti-k_T algorithm [45] was used for the jet definition. The term jet veto describes an additional cut on the transverse momentum of this third jet that can occur at NLO. The jet veto cuts away events where the third jet is 'central' and its transverse momentum is higher than a given threshold $p_T^{j_3} > p_T^{j^{veto}}$. Here 'central' means that the rapidity of the third jet must lie between the rapidities of the tagging jets. For this analysis the threshold was set to $p_T^{j^{veto}} = 50$ GeV.
A jet veto is usually applied to remove the QCD background in experimental analyses. Table 5.7 shows that the effect of the veto is rather small for $W\gamma jj$ production, independently of the application of the $m_T(W\gamma) > 90$ GeV cut.

$p_{T,veto}^j$	$m_T(W\gamma)_{min}$	σ_{NLO} [fb]	Deviation	K-Factor
—	0 GeV	7.916 ± 0.005	0.0%	1.01
50 GeV	0 GeV	7.588 ± 0.006	-4.1%	0.97
—	90 GeV	7.133 ± 0.005	-9.9%	1.01
50 GeV	90 GeV	6.834 ± 0.005	-13.7%	0.97

Table 5.7: This table shows the behavior of the NLO QCD cross section and the K-factor depending on the jet veto and the $m_T(W\gamma) > 90$ GeV cut.

This behavior is desired since the jet veto is intended to reduce the QCD background and to affect the electroweak process as little as possible. The η_{j_3} distribution in figure 5.13 demonstrates the effect of the jet veto very well. The $m_T(W\gamma) > 90$ GeV cut reduces $d\sigma/d\eta_{j_3}$ mainly in the outer region, where $|\eta_{j_3}| \in [2,3]$. The jet veto however, causes an almost constant reduction of $d\sigma/d\eta_{j_3}$ in $\eta_{j_3} \in [-3,3]$, leading to strong suppression of the central region, $\eta_{j_3} \in [-1,1]$. The main background to vector boson scattering processes are the corresponding QCD processes, depicted in figure 1.2 for $W^+\gamma jj$ production. Since these processes usually have a peak in the central region of the η_{j_3} distribution, the jet veto is a powerful method to reduce this background.

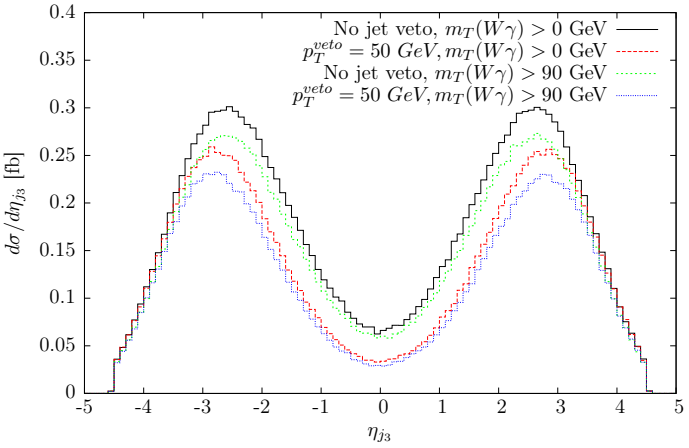

Figure 5.13: The $d\sigma/d\eta_{j_3}$ distributions for the four cases of table 5.7. As desired, the jet veto affects mostly the central region of the distribution.

A jet veto reduces the NLO cross section and leaves the LO cross section unchanged, which reduces the K-factor. Therefore, it is interesting to look at differential K-factor distributions. In figure 5.14, one can observe that for small values of $p_T^{j_1}$ the K-factor is not affected by the

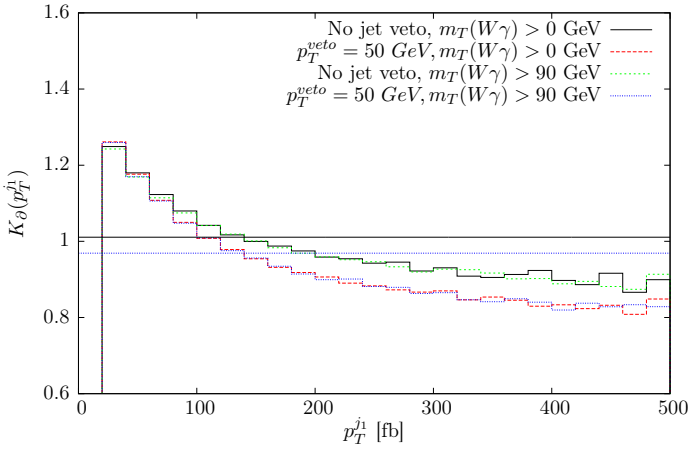

Figure 5.14: The differential K-factor distribution $K_\partial(p_T^{j_1})$ shows no relevant deviations at small $p_T^{j_1}$. But for larger values of $p_T^{j_1}$ the jet veto lowers the K-factors. The horizontal lines represent the total K-factors for the jet veto results (dashed blue line) and the normal results (solid black line).

jet veto. But in the region of larger $p_T^{j_1}$ the jet veto reduces the K-factor. The reason for this is that the hardest jet j_1 can not recoil against a hard third jet anymore if the jet veto is applied. $K_\partial(p_T^{j_1})$ is the only K-factor distribution, which shows a significant deviation for the jet veto result. For all other distributions, the differential K-factors are just shifted to lower values by the jet veto.

The application of a jet veto has only a very small impact on this process. However, it makes the estimation of the theoretical uncertainty more difficult due to correlations and cancellations between different phase space regions of the different contributions to the NLO cross section. This has been shown e.g. in the diploma thesis of J. Bellm [47] or in [48] and extensively discussed in the framework of Higgs physics. For those reasons, no jet veto has been applied in the following analyses of anomalous couplings.

5.8. Anomalous couplings

5.8.1. Differential distributions

For the examination of effects of anomalous gauge boson couplings, the $m_T(W\gamma) > 90$ GeV cut has been applied to remove final state radiation. Hence, the processes $W^{\pm}\gamma jj$ are more sensitive to triple and quartic gauge boson couplings. Here, the analysis will focus on quartic gauge boson couplings (QGC), since triple gauge boson couplings (TGC) occur already in QCD diboson production such as $pp \to W\gamma$. The QCD diboson production processes result in significantly larger cross section than diboson VBF processes and are therefore much more sensitive to anomalous TGC.
For the whole examination of anomalous couplings the form factor from equation (2.61) has been used with an exponent $n = 2$. The mass scale of the form factor Λ_{FF} is set depending on the size of the parameters of the operators according to table B.1 in appendix B.
Since there are 14 operators that affect the $WWZ\gamma$ and $WW\gamma\gamma$ couplings, the first step was to determine the operators with the largest impact. For this purpose, the NLO cross section was calculated for all 14 operators for the parameter values 100 TeV^{-4} and 800 TeV^{-4}. Here and in the following, we will omit the $/\Lambda^{-4}$ in f_i/Λ^{-4} for the sake of clarity.

	f_i [TeV^{-4}]	σ [fb]	Δ_{SM}	f_i [TeV^{-4}]	σ [fb]	Δ_{SM}
SM	0	7.137 ± 0.004	0.00%			
$f_{M,0}$	100	7.136 ± 0.009	-0.04%	800	7.294 ± 0.014	2.2%
$f_{M,1}$	100	7.213 ± 0.012	1.04%	800	7.799 ± 0.014	9.2%
$f_{M,2}$	100	7.154 ± 0.009	0.22%	800	7.401 ± 0.009	3.7%
$f_{M,3}$	100	7.163 ± 0.016	0.33%	800	7.585 ± 0.009	6.2%
$f_{M,4}$	100	7.219 ± 0.009	1.13%	800	8.002 ± 0.011	12.1%
$f_{M,5}$	100	7.201 ± 0.010	0.86%	800	7.912 ± 0.012	10.8%
$f_{M,6}$	100	7.164 ± 0.011	0.35%	800	7.207 ± 0.011	0.9%
$f_{M,7}$	100	7.158 ± 0.010	0.27%	800	7.394 ± 0.014	3.6%
$f_{T,0}$	100	7.245 ± 0.011	1.48%	800	8.449 ± 0.022	18.4%
$f_{T,1}$	100	7.290 ± 0.012	2.11%	800	8.669 ± 0.016	21.4%
$f_{T,2}$	100	7.067 ± 0.012	-1.00%	800	7.247 ± 0.011	1.5%
$f_{T,5}$	100	7.333 ± 0.015	2.72%	800	9.933 ± 0.018	39.1%
$f_{T,6}$	100	7.288 ± 0.010	2.09%	800	9.508 ± 0.014	33.2%
$f_{T,7}$	100	7.204 ± 0.011	0.91%	800	7.934 ± 0.013	11.1%

Table 5.8: This table shows the cross sections for all operators that affect the $WWZ\gamma$ and $WW\gamma\gamma$ couplings evaluated at $f_i = 100$ TeV^{-4} and $f_i = 800$ TeV^{-4}.

Table 5.8 shows that the operators with the largest influence on the cross section are $\mathcal{L}_{T,5}$, $\mathcal{L}_{T,6}$, $\mathcal{L}_{T,1}$ and $\mathcal{L}_{T,0}$. For the following analyses we will focus on these four operators. First, we want to look at anomalous coupling effects in differential distribution. Figures 5.15 to 5.17, 5.19 and 5.20 show a selection of distributions taking as an example the following parameters:

- $f_{T,0} = 400$ TeV^{-4}, $\Lambda_{FF} = 600$ GeV (dot dot dashed magenta line)
- $f_{T,1} = -400$ TeV^{-4}, $\Lambda_{FF} = 645$ GeV (dashed black line)
- $f_{T,5} = 100$ TeV^{-4}, $\Lambda_{FF} = 3475$ GeV (dot dashed green line)
- $f_{T,6} = 800$ TeV^{-4}, $\Lambda_{FF} = 1700$ GeV (dotted blue line)

The SM values (solid red line) and the estimated theoretical uncertainty (short dashed red lines) were included as well. For the estimation, the SM values were calculated for the canonical scale variations $\mu_{Fi} = \mu_{Ri} = \xi Q_i$ with $\xi = 0.5, 2$. All the following plots show results at NLO QCD.

A very promising distribution to look for effects of anomalous gauge boson couplings is $d\sigma/d\Phi_{j_1 j_2}$ where $\Phi_{j_1 j_2}$ is the azimuthal angle between the two hardest jets, which are in the case of VBF the tagging jets.

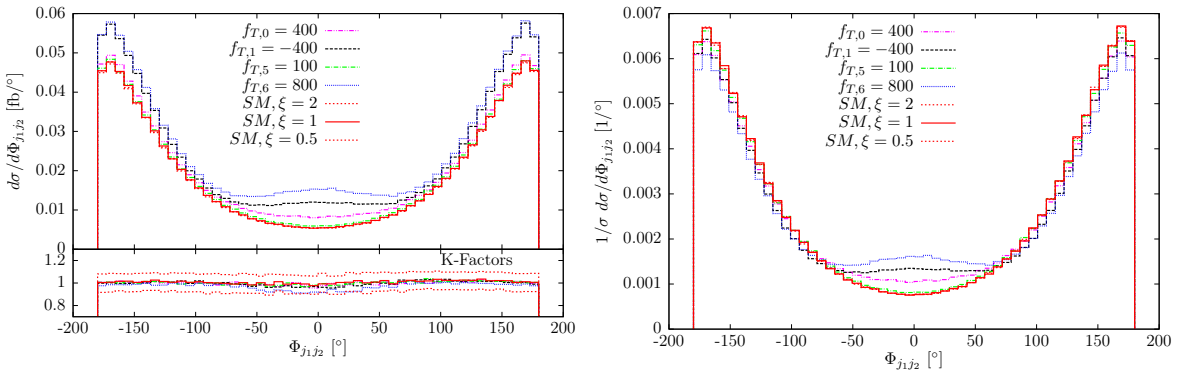

Figure 5.15: The left plot shows the $d\sigma/d\Phi_{j_1 j_2}$ distribution. The right plot shows the normalized $1/\sigma\ d\sigma/d\Phi_{j_1 j_2}$ distribution. This distribution shows a significant change in its shape due to anomalous couplings.

In the left plot of figure 5.15, which shows the $d\sigma/d\Phi_{j_1 j_2}$ distribution, we can see that with higher values of the parameters of the operators the cross section gets higher. The enhancements are visible especially in the central region and in the outer regions. The K-factor decreases in the central region for strong anomalous couplings. In the normalized distribution, $1/\sigma\ d\sigma/d\Phi_{j_1 j_2}$, in the right panel of figure 5.15, one can see that the shape of the distribution actually changes. For anomalous couplings, the central region is enhanced and the outer regions are reduced compared to the SM distribution.

Another common observable to look for effects of anomalous couplings is the transverse momentum distribution of the photon $d\sigma/dp_T^\gamma$. The plot of figure 5.16 shows this distribution with a logarithmic scale on the y-axis. This plot illustrates very well that deviations from the SM occur at high p_T^γ, i.e. high energies. The K-factor is stable over the whole range of p_T^γ. It is interesting to see that the curves for $f_{T,1} = -400$ TeV^{-4} and $f_{T,6} = 800$ TeV^{-4} cross at $p_T^\gamma \approx 375$ GeV. This is partly due to the form factor scale, which is lower for $f_{T,1}$, leading to a stronger suppression.

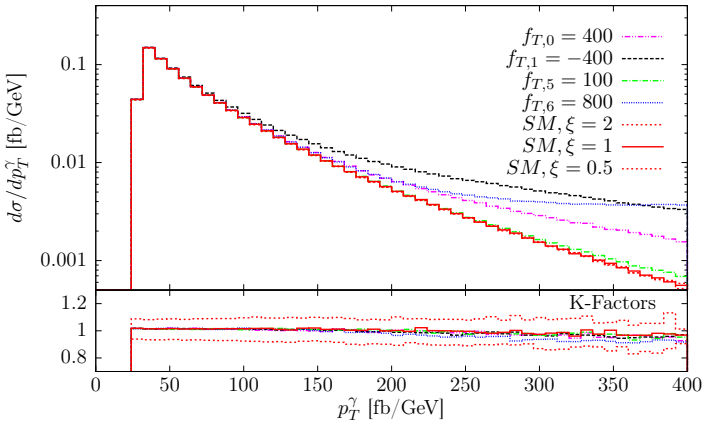

Figure 5.16: This plot shows the $d\sigma/dp_T^\gamma$ distribution with a logarithmic scale on the y-axis.

Two more observable, that show effects of anomalous couplings at high energies, are $d\sigma/dm_T(W\gamma)$ and $d\sigma/d\text{min}(p_T^W, p_T^\gamma)$.

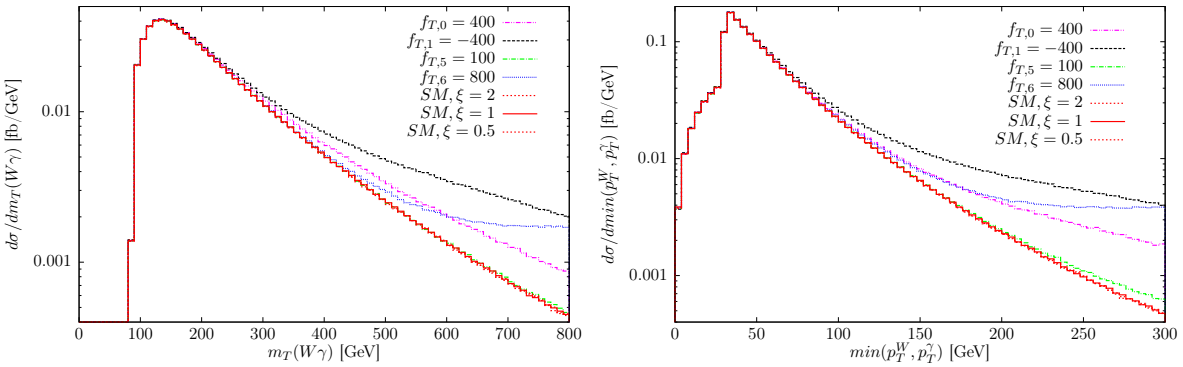

Figure 5.17: The distributions $d\sigma/dm_T(W\gamma)$ and $d\sigma/d\text{min}(p_T^W, p_T^\gamma)$ show anomalous coupling effects at high energies.

Again, we can see clear deviations from the SM values in both plots of figure 5.17, if we use a logarithmic scale on the y-axis. The curve for $f_{T,6} = 800$ TeV^{-4} becomes flat for high energies again while all the other operators and the SM are continuously declining.

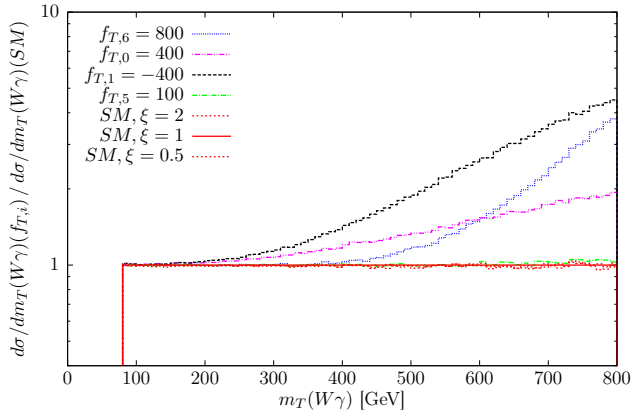

Figure 5.18: This figure shows the $d\sigma/dm_T(W\gamma)$ distributions normalized to the SM values.

In order to illustrate the high energy behavior of anomalous couplings, figure 5.18 shows the $d\sigma/dm_T(W\gamma)$ distributions normalized to the SM values. This figure demonstrates that the deviations from the Standard Model rise with increasing energy.

Since we are examining a final state photon process, another promising observable is the pseudo rapidity distribution of the photon $d\sigma/d\eta_\gamma$.

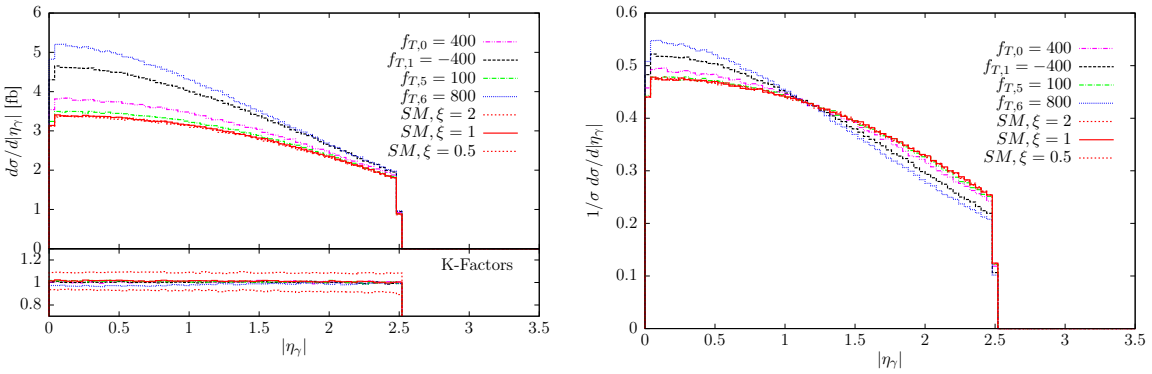

Figure 5.19: The $d\sigma/d\eta_\gamma$ distribution shows a larger cross section for smaller photon rapidities η_γ. The normalized photon rapidity distribution $1/\sigma\ d\sigma/d\eta_\gamma$ (right plot) shows significant changes in shape for anomalous couplings.

The left plot of figure 5.19 shows that anomalous couplings increase the $d\sigma/d\eta_\gamma$ distribution for small pseudo rapidities. This means that more photons are emitted perpendicularly to the beam axis. In the right plot, where the normalized pseudo rapidity distribution $1/\sigma\ d\sigma/d\eta_\gamma$ is shown, we can see that the shape of this distribution changes significantly, if anomalous couplings are applied.

The azimuthal angle between the photon and the lepton $\Phi_{l\gamma}$ provides another possibility to see effects of anomalous couplings. The corresponding differential distribution is depicted in figure 5.20.

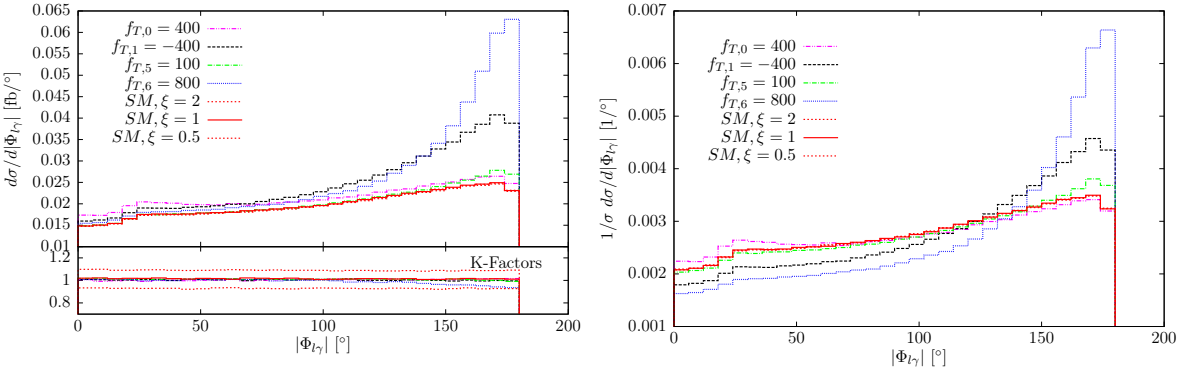

Figure 5.20: In the $d\sigma/d\Phi_{l\gamma}$ plot on the left hand side we can see that anomalous couplings become visible for large values of $\Phi_{l\gamma}$. This distribution changes its shape significantly for large anomalous coupling parameters (right plot).

We can see that the region of large azimuthal angles, $\Phi_{l\gamma} > 130°$, is strongly enhanced for $f_{T,1} = -400$ TeV^{-4} and $f_{T,6} = 800$ TeV^{-4}. For these two setups, the shape of the distribution

changes significantly. This can be seen in the right plot showing the normalized distributions. Although, the $d\sigma/d\Phi_{l\gamma}$ distribution looks very promising for $f_{T,1} = -400$ TeV^{-4} and $f_{T,6} = 800$ TeV^{-4}, the effects of $f_{T,0} = 400$ TeV^{-4} and $f_{T,5} = 100$ TeV^{-4} are barely visible in this distribution. Notice that the K-factor here slightly decreases for $f_{T,6} = 800$ TeV^{-4} and $\Phi_{l\gamma} > 130°$.

In conclusion, it can be stated that the we can see significant effects for $f_{T,1} = -400$ TeV^{-4} and $f_{T,6} = 800$ TeV^{-4} in all distributions. $f_{T,0} = 400$ TeV^{-4} leads to smaller effects but they are still visible in most of the presented plots. The curves for $f_{T,5} = 100$ TeV^{-4} usually show no significant deviations from the SM values since parameter values of 100 TeV^{-4} lead to significant deviations only at energies much higher than the ones that were examined here.

5.8.2. Two dimensional cross sections analysis

So far, we have only examined one non-zero operator at a time. But there are correlations between the operators since they affect the same couplings, namely $WW\gamma\gamma$ and $WWZ\gamma$. For the analysis of these correlations all possible combinations of the four operators $\mathcal{L}_{T,0}$, $\mathcal{L}_{T,1}$, $\mathcal{L}_{T,5}$ and $\mathcal{L}_{T,6}$ were examined. Both coupling parameters were varied over the range $[-1500, 1500]$ TeV^{-4} in 11 steps. The scale of the form factor Λ_{FF} was always set to the lower value of the two possible scales. That way the form factor also suppresses the contribution of the operator with the larger scale at high energies. Figure 5.21 shows the two dimensional projection of the cross section depending on two operators.

The correlations are different for each pair of operators. The only plot, which looks symmetric is the $(f_{T,5}, f_{T,6})$ plot on the bottom right of figure 5.21. This is also the plot, in which we can see the largest effects, so there must be a strong, positive correlations between $\mathcal{L}_{T,5}$ and $\mathcal{L}_{T,6}$. The upper left plot shows the cross sections for $(f_{T,0}, f_{T,1})$. This plot is not symmetric but the cross section rises significantly for high negative values of both operators indicating a positive correlation of the operators $(\mathcal{L}_{T,0}, \mathcal{L}_{T,1})$.
The remaining plots showing $(f_{T,0}, f_{T,5})$,$(f_{T,0}, f_{T,6})$, $(f_{T,1}, f_{T,5})$ and $(f_{T,1}, f_{T,6})$ look very similar. The correlations between the corresponding operators are small and the change in the cross section is dominated by $f_{T,0}$ or $f_{T,1}$, respectively while $f_{T,5}$ or $f_{T,6}$ only have a small effect. In these four plots, negative values of the parameters on the x-axis have a stronger influence on the cross section than positive ones.

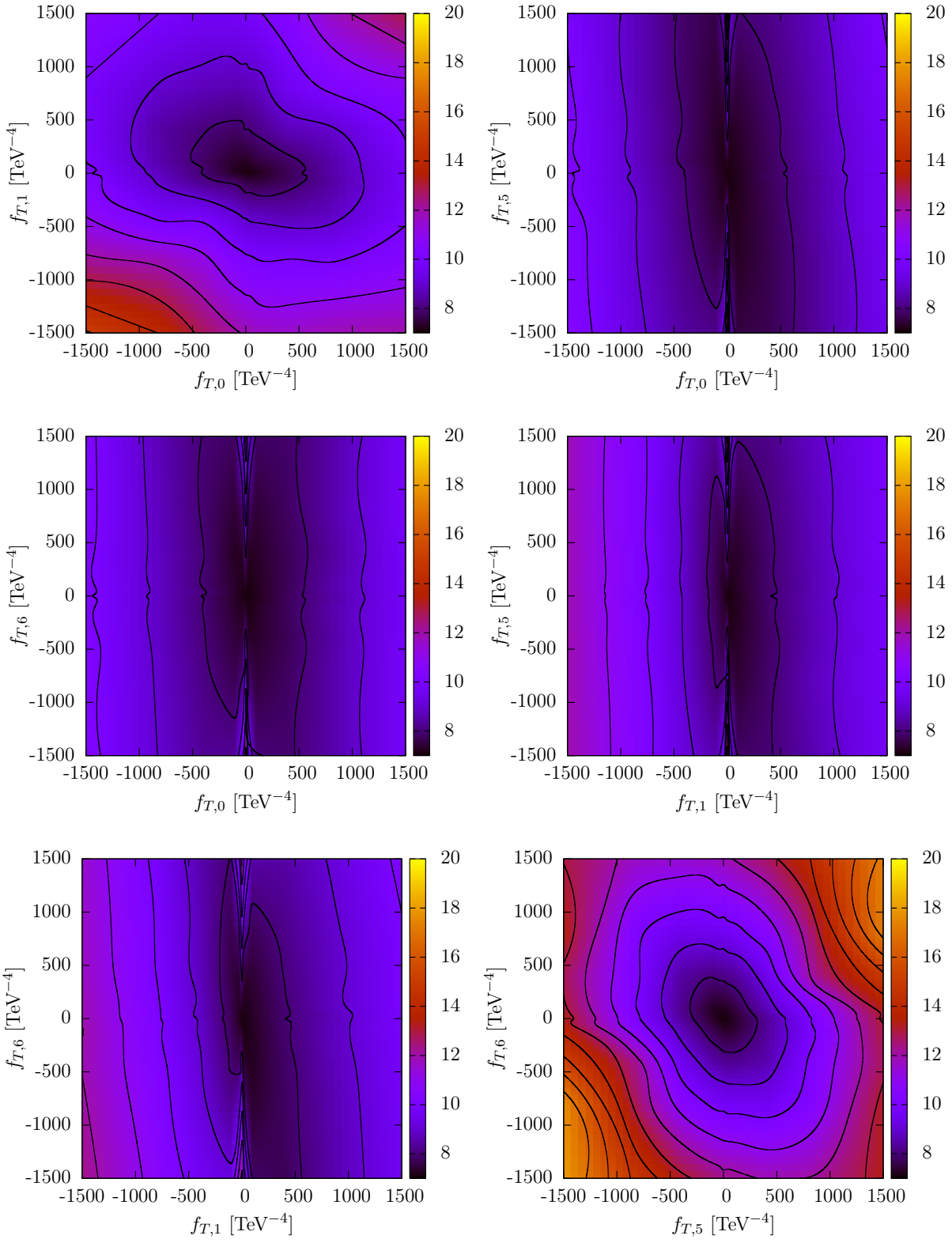

Figure 5.21: These plots show the NLO cross section depending on two coupling parameters. The correlations are different for each pair of operators since the operators affect different helicities. The black contours indicate integer values of the cross section in [fb].

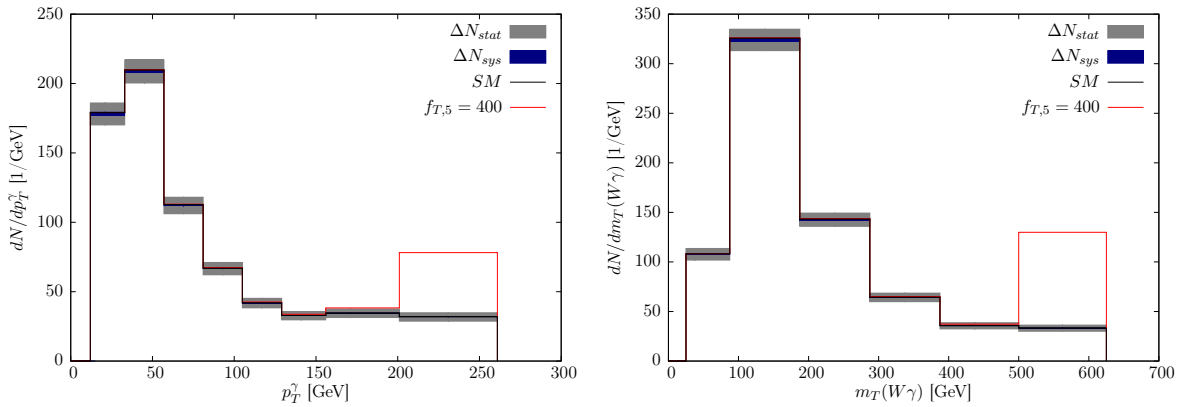

Figure 5.22: This figure shows the histograms dN/dp_T^γ (left plot) and $dN/dm_T(W\gamma)$ (right plot) with the new binning. The parameters that were used to obtain this new binning are $N_{min} = 30$ and $N_{min}^{bin} = 3$. The original widths of the histograms were $p_T^\gamma \in [0, 600]$ GeV and $dm_T(W\gamma) \in [0, 2500]$ GeV.

5.8.3. Sensitivity analysis

So far, we have only examined qualitative effects of anomalous gauge boson couplings. The goal of this section is to calculate possible exclusion limits for the operators $\mathcal{L}_{T,0}$, $\mathcal{L}_{T,1}$, $\mathcal{L}_{T,5}$ and $\mathcal{L}_{T,6}$. For this purpose, we took all possible pairs of operators and calculated a variety of histograms varying each parameter over the following values in TeV^{-4}

$$0,\ \pm 25,\ \pm 100,\ \pm 400,\ \pm 800,\ \pm 1500. \tag{5.6}$$

We point out that a pre-optimized grid and only one iteration was used, so the phase space points are the same for all setups. We assumed a collider energy of $E_{cm} = 14$ TeV and a luminosity of $L = 100\ \text{fb}^{-1}$.

The first step was to make a new binning of a given histogram. The number of events in the i-th bin of a histogram of the observable $\mathcal{O}$ is

$$N_i = L \left(\frac{d\sigma_{NLO}}{d\mathcal{O}} \right)_i \Delta_{bin,\mathcal{O}}. \tag{5.7}$$

Here, $\Delta_{bin,\mathcal{O}}$ is the width of a bin in the histogram of the observable $\mathcal{O}$ and $(d\sigma_{NLO}/d\mathcal{O})_i$ is the cross section that lies in bin i. For the histograms with and without anomalous couplings, these bins were combined until the number of SM events in the new bin, $N_k^{SM,new}$, exceeded a lower limit N_{min}. Since the size of the bins can lead to experimental uncertainties, we also required that a minimum number of bins N_{min}^{bin} were combined

$$N_k^{SM,new} = \sum_i^n N_i \ > N_{min}, \qquad n \geq N_{min}^{bin}. \tag{5.8}$$

This procedure was started from the right end of the histogram, where the effects of anomalous couplings are usually visible as shown in section 5.8.1. Figure 5.22 shows the histograms dN/dp_T^γ and $dN/dm_T(W\gamma)$ with the new binning for $N_{min} = 30$. One can see that the significant deviation from the SM values is located in the last bin. The number of SM events in this bin is close to $N_{min} = 30$ as required. For the estimation of the theoretical uncertainty we took again the scale variation in the interval $\xi \in [0.5, 2]$

$$\Delta N_k^{sys} = \frac{1}{2} \left| N_k(\mu_{Ri} = \mu_{Fi} = 2Q_i) - N_k(\mu_{Ri} = \mu_{Fi} = \frac{1}{2} Q_i) \right|. \tag{5.9}$$

However, the statistical error is the dominant one. For its estimation it was assumed that the number of events follows a Poisson distribution

$$\Delta N_k^{stat} = \sqrt{N_k}. \tag{5.10}$$

In the next step we want to determine a function that describes the number of events $N_k^{AC}(f_x, f_y)$ in one new bin k, depending on the values of two coupling parameters f_x and f_y. We know that the matrix element $\mathcal{M}$ is linear in the quartic couplings, hence it is linear in f_x and f_y. The number of events is proportional to the cross section, which depends on the matrix element squared $|\mathcal{M}|^2$. Therefore, we choose the following ansatz

$$N_k^{AC}(f_x, f_y) = N_k^{SM} + a_k f_x + b_k f_y + c_k f_x^2 + d_k f_y^2 + e_k f_x f_y. \tag{5.11}$$

The parameters $a_k, \ldots, e_k$ were fitted to the calculated N_k^{AC} values using the 'fit' function of GNUPLOT. [2] With this paraboloid it is possible to determine confidence levels (CLs) in the $f_x - f_y$ plane. This was done by scanning this plane in steps of $\Delta f_i = 5$ TeV^{-4} and calculating the χ^2 value for each point, which is given by

$$\chi^2 = \sum_k^{k_{max}} \frac{(N_k^{SM} - N_k^{AC}(f_x, f_y))^2}{\left(\Delta N_k^{sys}\right)^2 + \left(\Delta N_k^{stat}\right)^2} + k_{max} - 1, \tag{5.12}$$

where k_{max} denotes the maximum number of new bins. The function *chisqprob*, included in the PYTHON module *scipy.stats.stats*, was used to calculate the corresponding probability for each point in the plane. Several examples for confidence levels are shown in figure 5.23. The shape of the CLs reflects again the correlations between the operators, which have been examined already in section 5.8.2. From the plots in the first row of figure 5.23 one can see that the size of the confidence levels depend strongly on the observable we choose.

In appendix C, several tables with the detailed results of this analysis are presented. Those tables give the setup that was used for the new binning and the exclusion limits that were reached. To obtain a measure for the correlation between the operators, the area of the confidence levels is given in those tables. The observables that yield the strongest constraints on the operators are $m_T(W\gamma)$ and p_T^γ. Depending on the observable and the pair of operators that was examined, we reached exclusion limits of a few hundred TeV^{-4}. In the analysis of $\mathcal{L}_{T,5}$ with $\mathcal{L}_{T,6}$ the limit reached for $f_{T,5}$ was -225 – 250 TeV^{-4} at 95% CL. Since this looks very promising, it can be concluded that $W\gamma$ production via VBF will be an interesting process in the search for new physics at the LHC.

[2] The 'fit' function of GNUPLOT uses the nonlinear least-squares (NLLS) Marquardt-Levenberg algorithm.

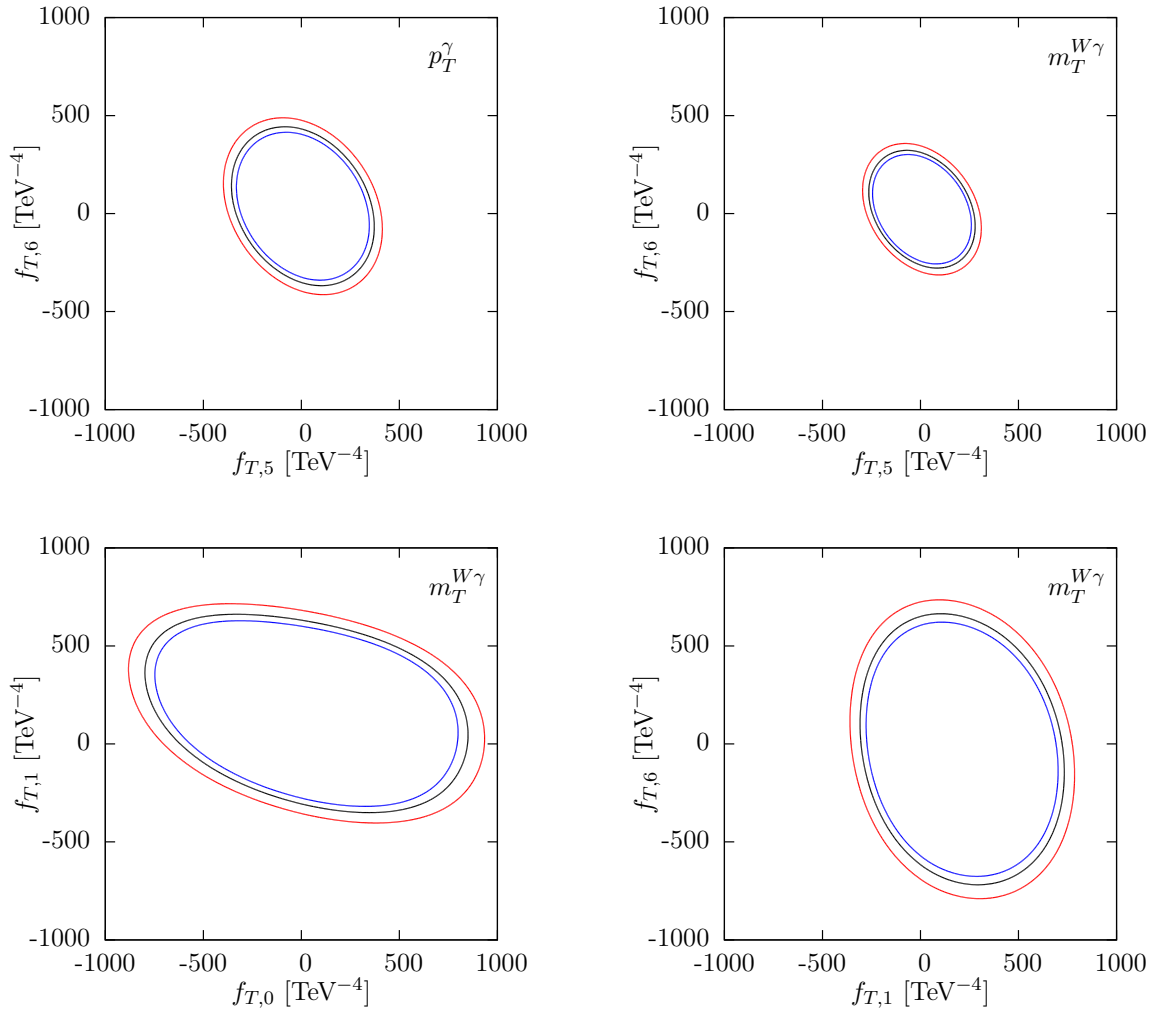

Figure 5.23: The plots in this figure show 90% (blue lines), 95% (black lines) and 99% (red lines) confidence levels for a selection of operators and histograms. In the plots in the upper row the CLs in the $(f_{T,5} - f_{T,6})$ plane are presented for the observables p_T^γ and $m_T(W\gamma)$. The plots in the lower row show the CLs for $m_T(W\gamma)$ and the operators $(f_{T,0} - f_{T,1})$ and $(f_{T,1} - f_{T,6})$. The parameters that were used for the new binning are $N_{min} = 30$ and $N_{min}^{bin} = 3$.

CHAPTER 6

CONCLUSION

For this purpose, this process was implemented in the fully flexible parton-level Monte-Carlo program VBFNLO. We included all off-shell effects and spin correlations. The Catani-Seymour subtraction formalism [34] was used to calculate the real emission corrections. The poles of the $\boldsymbol{I}$ operator were canceled analytically against the poles of the virtual loop corrections. This allowed us to calculate only the finite part of the virtual corrections using the *Box*- and *Penline* functions created by F. Campanario [37].
Two major advantages of VBFNLO are the use of leptonic tensors and the shift of all Born-type contributions to one iteration in the calculation of the virtual corrections. This yields a tremendous decrease in run time compared to other Monte-Carlo programs.

To assure the correctness of the calculation, the leading-order and the 3-jet-LO cross sections were checked against the Monte-Carlo program SHERPA [42]. Our implementation comprises only t-channel Feynman diagrams. This would lead to deviations from the SHERPA results, which also take s- and u-channel diagrams and interference terms into account. Due to VBF cuts, complete agreement was found at LO. However, in the case of the 3 jet LO and the real emission calculation s-channel contributions can pass the VBF cuts. These contributions lead to deviations from the SHERPA results but it has been explicitly shown that they are small.

When calculating final state photon processes at NLO QCD, one has to separate the photon properly from the partons in the final state. In this calculation, this is done by imposing the photon isolation cut by S. Frixione [26]. So far, no independent program is able to calculate the electroweak process $pp \to W^{\pm}\gamma jj$ at NLO QCD. Therefore, the calculation of the virtual corrections was checked very carefully.
The *Box*- and *Penline* functions are able to calculate the poles of the virtual matrix elements, which are proportional to the corresponding Born diagrams. This allows us to calculate the total matrix element using those functions and compare it to the result of the LO calculation, which has been checked against MADGRAPH [41]. An expansion of the analytic form of the virtual contributions in the scale leads to additional terms that cancel the scale dependence of the finite virtual matrix elements. This was used to check the finite parts, which contribute to the cross section. Furthermore, this check assures that the scale used for the calculation of the virtual contributions is correct.

The virtual corrections and the real emission contain terms that are proportional to the born matrix element squared. These terms can be integrated over either of these two phase spaces. We shifted parts of these terms from one phase space to the other and still found agreement within the numerical accuracy. Due to all those checks, we are very confident that our calculation is correct.

The main motivation for calculating the NLO QCD corrections was to reduce the scale dependence of the cross section, which is usually used to estimate the theoretical error of a calculation. It was found that the NLO QCD corrections are small, i.e. the K-factor is close to 1, for $\mu_{Fi} = \mu_{Ri} = Q_i$. We obtained $\sigma_{LO} = 7.828 \pm 5 \cdot 10^{-3}$ fb and $\sigma_{NLO} = 7.910 \pm 7 \cdot 10^{-3}$ fb for $W^+\gamma jj$ production and $\sigma_{LO} = 4.486 \pm 3 \cdot 10^{-3}$ fb and $\sigma_{NLO} = 4.588 \pm 5 \cdot 10^{-3}$ fb for $W^-\gamma jj$ production. Q_i is the absolute value of the momentum transferred from quark line i to the electroweak part of the process. It can be interpreted as a measure for the virtuality of the corresponding emitted gauge boson. This is the optimal scale for VBF and WBS processes since it reflects their kinematics.
It was indeed possible to reduce the scale uncertainty significantly by calculating the NLO QCD corrections. The scale variation in the interval $\xi \in [0.5, 2]$ decreased from 15% at LO to 2% at NLO for $\mu_{0i} = \xi Q_i$.

Besides QCD triboson production, weak boson scattering processes will be used at the LHC to probe quartic couplings of weak gauge bosons. For the simulation of effects of anomalous triple and quartic couplings, a framework based on [19] was implemented into VBFNLO by O. Schlimpert [44]. With this framework it was possible to include anomalous couplings in $W^\pm\gamma$ production via weak boson scattering.

In processes with a lepton and a photon in the final state, the photon can be radiated off the lepton, which is called final state radiation. This is a simple QED process, which is very well known. By imposing a cut on the transverse mass cluster of the $W\gamma$ system $m_T(W\gamma) > 90$ GeV, it is possible to remove final state radiation, which increases the sensitivity to anomalous couplings.

Effects from anomalous couplings were shown in differential distributions for a selection of parameters. The differential cross section for anomalous couplings increases with the center of mass energy, which leads to violation of the unitarity of the S matrix at high energies. The reason for this is that our EFT approach comprises only dimension 6 and 8 operators. But effects from higher order operators become important in the high energy region. In order to avoid the unitarity violation, we apply a form factor that suppresses the effects from anomalous couplings in the high energy region. Since there are 14 operators that affect the $WWZ\gamma$ and $WW\gamma\gamma$ couplings, the first step was to determine the operators with the largest effect on the cross section. 4 operators were chosen for a more detailed examination.
Some operators affect the same helicities of the four bosons in the quartic couplings, which leads to correlations between different operators. These correlations were shown for pairs of two operators at the level of the total cross section.

Finally, the sensitivity of $W^\pm\gamma$ production via weak boson scattering to anomalous couplings was examined. For this, the histograms were newly binned such that the last bin, where usually the biggest deviation from the SM occurs, contains a minimum number of events. A paraboloid was fitted to the calculated number of events for different values of a pair of parameters. With this paraboloid, it was possible to determine confidence levels using a χ^2 test. The most sensitive observables were found to be the transverse mass cluster of the $W\gamma$ system $m_T(W\gamma)$, and the transverse momentum of the photon p_T^γ.

Assuming an integrated luminosity of $L = 100$ fb^{-1} and a collider energy of $E_{CM} = 14$ TeV, the limits on the parameters that we obtained were relatively strict for some operator pairs. Depending on the setup of the new binning we reached limits on the couplings of the operators down to -215 – 250 TeV^{-4} at 95% CL. Since this setup seems realistic for the next LHC run scheduled for 2014, $W\gamma$ production via VBF will soon play an important role in the search for new physics.

CHAPTER 7

ZUSAMMENFASSUNG

Gegenwärtig basiert unser Verständnis des Universums auf zwei Theorien. Die allgemeine Relativitätstheorie von Albert Einstein beschreibt die Gravitation und das Standardmodell (SM) die Wechselwirkungen der Elementarteilchen. Das SM ist eine lokale Eichtheorie, die in den 1970er Jahren entwickelt wurde und die starke, die schwache und die elektromagnetische Wechselwirkung mittels einer $SU(3)_c \times SU(2)_L \times U(1)_Y$ Eichgruppe beschreibt.
Die Materieteilchen werden durch Fermionfelder beschrieben und die Wechselwirkungen zwischen ihnen werden durch Eichbosonen vermittelt. Die $SU(3)_c$ Eichgruppe beschreibt die Quantenchromodynamik, die Wechselwirkung der Partonen. Quarks und Gluonen werden zusammen als Partonen bezeichnet und sind die Bestandteile von Protonen und Neutronen, der sichtbaren, baryonischen Materie, die uns umgibt.
Der elektroschwache Sektor des Standardmodells wird durch die Gruppe $SU(2)_L \times U(1)_Y$ beschrieben. Diese Eichsymmetrie wird durch den Vakuumerwartungswert des Higgs-Feldes zur $U(1)_{em}$ gebrochen, welche die Quantenelektrodynamik beschreibt, die Wechselwirkung zwischen Photonen und elektrisch geladenen Teilchen. Durch diese sogenannte spontane Symmetriebrechung ist es möglich Massenterme für die schwachen Eichbosonen, die W- und Z-Bosonen, zu konstruieren. Die schwache Wechselwirkung vermittelt beispielsweise den β-Zerfall.

Obwohl die Vorhersagen des Standardmodells bisher mit beeindruckender Präzision experimentell bestätigt wurden, gibt es mehrere Phänomene, die das Standardmodell nicht oder nicht korrekt beschreibt. So ist es beispielsweise im Standardmodell nicht möglich die Kopplungen der drei Wechselwirkungen zu vereinigen oder dunkle Materie zu beschreiben. Auch die Vorhersage des Standardmodells für den g-Faktor des Myons stimmt nicht mit dem experimentell gemessenen Wert überein [2]. Darüber hinaus gibt es noch zahlreiche, weitere Hinweise auf Physik jenseits des Standardmodells.

Mit dem „Large Hadron Collider“ (LHC) am CERN steht der Teilchenphysik ein Beschleuniger zur Verfügung, der es erlaubt, das Standardmodell bei noch nie erreichten Energien zu untersuchen. Im Juli 2012 wurde bereits die Entdeckung eines skalaren Bosons bekannt gegeben, bei dem es sich allem Anschein nach um das SM-Higgs-Boson handelt [3, 4]. Eine weitere Möglichkeit die Vorhersagen des Standardmodells zu überprüfen, ist die Untersuchung von sogenannten anomalen Kopplungen. Da die Theorie der elektroschwache Wechselwirkung eine nicht-abelsche Eichtheorie ist, treten im Standardmodell Kopplungen von drei und vier

schwachen Eichbosonen in einem Vertex auf. Würde die Stärke dieser Kopplungen von den Vorhersagen des Standardmodells abweichen, wäre dies ein starker Hinweis auf Physik jenseits des Standardmodells.
Die möglichen Abweichungen der Dreierkopplungen von ihren SM-Werten wurden bereits durch die Analyse der Daten aus den 7 und 8 TeV Läufen des LHCs relativ stark eingeschränkt [6]. Die Parameter der Operatoren, die Abweichungen der Viererkopplungen von den SM-Vorhersagen modellieren, konnten jedoch nur leicht eingeschränkt werden [7]. Diese Kopplungen treten bei der QCD-Produktion von drei Eichbosonen und in Dibosonproduktion in Vektorbosonstreuung auf. $pp \to W^{\pm}\gamma jj$ zählt zu diesen Prozessen und empfiehlt sich besonders durch den relativ großen Wirkungsquerschnitt, der typisch für Prozesse mit einem Photon im Endzustand ist.

Ziel dieser Arbeit war es, diesen Prozess auf nächst-führender Ordnung QCD zu berechnen. Im Vergleich zur führenden Ordnung (engl. leading order, LO) wird die Skalenabhängigkeit des Wirkungsquerschnitts auf nächst-führender Ordnung (engl. next-to-leading order, NLO) deutlich verringert. Würde man alle Ordnungen der Störungstheorie berechnen, wäre der Wirkungsquerschnitt unabhängig von der Renormierungs- und Faktorisierungsskala. Daher wird die Skalenunsicherheit oft zur Abschätzung des theoretischen Fehlers einer Rechnung verwendet. In dieser Arbeit werden nur die QCD-Korrekturen der nächst-führenden Ordnung berechnet und die QED-Korrekturen vernachlässigt, da die starke Kopplung bei der Energieskala des Prozesses ungefähr 15 mal größer ist als die elektromagnetische.

Zur Berechnung der $W\gamma$-Produktion in Vektorbosonstreuung wurde dieser Prozess in das Monte-Carlo-Programm VBFNLO[1] [8] implementiert. Das im Allgemeinen hochdimensionale Integral, das zur Berechnung des Wirkungsquerschnitts zu lösen ist, wird durch numerische Integration mit Hilfe des Vegas-Algorithmus [28] berechnet. Zur Berechnung der Matrixelemente wird der HELAS-Formalismus [31] verwendet. Die Streureaktionen der schwachen Eichbosonen und der Zerfall des W-Bosons werden in sogenannte leptonische Tensoren zusammengefasst, die für jeden Phasenraumpunkt nur einmal berechnet werden müssen. Diese modulare Struktur beschleunigt die Berechnung des Wirkungsquerschnitts nicht nur, sondern macht das Programm auch leicht zugänglich für Modifikationen der Kopplungen der Eichbosonen.

Zur Berechnung des Wirkungsquerschnitts in nächst-führender Ordnung müssen die reelle Emission und die virtuellen Schleifenkorrekturen berechnet werden. Diese beiden Anteile sind divergent und nur ihre Summe ist endlich. Um eine numerische Integration über die beiden unterschiedlich dimensionalen Phasenräume zu ermöglichen, wird daher der Dipol-Formalismus von Catani und Seymour [34] verwendet. Dabei werden Subtraktionsmatrixelemente konstruiert, welche die divergente Struktur der reellen Emission wegheben und diese somit numerisch integrierbar machen. Die entsprechenden Pole dieser Subtraktionsterme heben sich genau mit den Polen der virtuellen Korrekturen weg.
Die Berechnung der Box- und Pentagonkorrekturen erfolgt mit Hilfe der *Box*- und *Penline*-Funktionen, die von F. Campanario entwickelt wurden [37]. Die Anteile der Box- und Pentagonkorrekturen, die proportional zum entsprechenden Born-Matrixelement sind, werden von den endlichen Anteilen der virtuellen Korrekturen subtrahiert und zusammen mit den Vertexorrekturen in einer getrennten Iteration berechnet. Die numerische Stabilität der Berechnung der virtuellen Korrekturen wird durch Überprüfung von Ward-Identitäten sichergestellt.

[1] VBFNLO wird am Institut für theoretische Physik in der Gruppe von Professor Zeppenfeld entwickelt.

Um die Ergebnisse unserer Berechnung zu verifizieren, wurden die Wirkungsquerschnitte der führenden Ordnung für die Prozesse $pp \to W^{\pm}\gamma jj$ und $pp \to W^{\pm}\gamma jjj$ mit dem unabhängigen Monte-Carlo-Programm SHERPA [42] verglichen. Die Implementierung in VBFNLO umfasst nur t-Kanal-Beiträge, während SHERPA auch s- und u-Kanal-Beiträge, sowie Interferenzterme berechnet.
Experimentell werden Ereignisse, die durch Vektorbosonfusion (VBF) entstehen, durch die zwei „tagging jets“ identifiziert, die in fast genau entgegengesetzte Richtung zeigen. Bei einer theoretischen Rechnung wird dies durch spezielle VBF-Phasenraumschnitte simuliert. Diese Phasenraumschnitte sorgen dafür, dass die t-Kanal-Diagramme den dominanten Beitrag liefern.
Somit finden wir für den Prozess $pp \to W^{\pm}\gamma jj$ Übereinstimmung mit den SHERPA-Ergebnissen, für $pp \to W^{\pm}\gamma jjj$ jedoch Abweichungen von bis zu 4%. Diese Abweichungen kommen durch s-Kanal-Diagramme, die in manchen Bereichen des Phasenraums nicht durch die VBF-Phasenraumschnitte eliminiert werden. Es wurde jedoch explizit gezeigt, dass diese Beiträge klein sind.

Um die Berechnung der Schleifenkorrekturen zu überprüfen wurden verschiedene Tests durchgeführt. Insbesondere ist es mit den *Box*- und *Penline*-Funktionen möglich, auch die Polterme der virtuellen Korrekturen zu berechnen. Diese sind proportional zu den entsprechenden Born-Matrixelementen. Somit war es möglich das Matrixelement mit den *Box*- und *Penline*-Funktionen zu berechnen und mit dem Ergebnis der führenden Ordnung, das schon mit MADGRAPH [41] überprüft wurde, zu verifizieren.

In Eichtheorien wie dem Standardmodell lässt sich die Eichinvarianz bei Prozessen mit einem masselosen Eichboson im Endzustand direkt überprüfen. Ersetzt man den Polarisationsvektor des masselosen Eichbosons durch seinen Impuls, ist das Matrixelement identisch null. Dieser Test wurde für alle möglichen Beiträge durchgeführt und hat gezeigt, dass die Eichinvarianz im Rahmen der numerischen Genauigkeit erhalten ist.

Als Ergebnis für die Wirkungsquerschnitte erhielten wir $\sigma_{LO} = 7.828 \pm 5 \cdot 10^{-3}$ fb und $\sigma_{NLO} = 7.910 \pm 7 \cdot 10^{-3}$ fb für den Prozess $pp \to W^{+}\gamma jj$ und $\sigma_{LO} = 4.486 \pm 3 \cdot 10^{-3}$ fb und $\sigma_{NLO} = 4.588 \pm 5 \cdot 10^{-3}$ fb für den Prozess $pp \to W^{-}\gamma jj$. Der Wirkungsquerschnitt in führender Ordnung hängt nur von der Faktorisierungsskala ab, die die Energieskala der PDFs darstellt. Die PDFs geben die Wahrscheinlichkeit an, ein Parton mit einem bestimmten „Flavor“ und dem Impulsanteil x des Protons zu finden. Auf nächst-führender Ordnung kommt durch die zusätzlichen starken Kopplungen eine Abhängigkeit von der Renormierungsskala hinzu.
Für die folgenden Analysen wurde für beide Skalen der Impulstransfer der entsprechenden Quarklinie gewählt. Da dieser auch als Maß für die Virtualität des emittierten Eichbosons interpretiert werden kann und diese Größe somit die Kinematik des Prozesses widerspiegelt, ist diese Skalenwahl sehr gut für VBF-Prozesse geeignet. Bei der Untersuchung der Skalenabhängigkeit wurde gefunden, dass diese durch die Berechnung der nächst-führenden Ordnung von 15% auf 2% reduziert werden konnte. Die Werte beziehen sich hier auf die relative Variation des Wirkungsquerschnitts im Bereich von einhalb bis zweimal der Skala.

Bei Prozessen mit einem geladenen Lepton und einem Photon im Endzustand kann das Photon vom Lepton abgestrahlt werden, was als Bremsstrahlung bezeichnet wird. Da es sich hierbei um einen reinen QED-Prozess handelt, wir aber an der Untersuchung der Kopplungen der schwachen Eichbosonen interessiert sind, soll dieser Beitrag unterdrückt werden. Dies kann bei der $W^{\pm}\gamma$-Produktion in Vektorbosonstreuung durch Einführung einer Untergrenze von 90 GeV an das transversalen Massenclusters des $W\gamma$-Systems, $m_T(W\gamma)$, erreicht werden.

Zur Simulation von anomalen Kopplungen der schwachen Eichbosonen wurde im Rahmen der Diplomarbeit von O. Schlimpert [44] die entsprechende Grundstruktur in VBFNLO implementiert. Diese basiert auf einer effektiven Feldtheorie, die die Lagrangedichte des Standardmodells um Operatoren der Dimension 6 und 8 erweitert. Somit konnte die Simulation von anomalen Kopplungen in die $W^{\pm}\gamma$-Produktion in Vektorbosonstreuung implementiert werden. Dabei werden nur die leptonischen Tensoren modifiziert, die die Selbstkopplungen der schwachen Eichbosonen enthalten. QCD-Dibosonprozesse wie beispielsweise $pp \to W^{\pm}\gamma$ haben einen signifikant größeren Wirkungsquerschnitt als die entsprechenden Diboson-VBF-Prozesse, beinhalten aber bereits Dreierkopplungen von schwachen Eichbosonen. Daher sind sie wesentlich sensitiver auf Abweichungen von den Standardmodellwerten dieser Kopplungen. Aus diesem Grund wurden in der Analyse der Effekte durch anomale Kopplung nur Operatoren betrachtet die Viererkopplungen von schwachen Eichbosonen modifizieren.

Die Effekte der Anomalen Kopplungen steigen mit der Schwerpunktsenergie des elektroschwachen Prozesses an. Dies führt oberhalb einer gewissen Schwelle zur Verletzung der Unitarität der S-Matrix. Um dies zu verhindern, wurde bei der Berechnung von $pp \to W^{\pm}\gamma jj$ mit anomalen Kopplungen stets ein Formfaktor verwendet.

Die Effekte der anomalen Kopplungen lassen sich abhängig vom Operator und der Stärke seiner Kopplung in verschiedenen differentiellen Verteilungen beobachten. Die Abweichungen von den SM-Werten lassen sich besonders gut im Hochenergiebereich der $m_T(W\gamma)$- oder der p_T^{γ}-Verteilungen beobachten. Da die einzelnen Operatoren nur spezielle Helizitäten der Eichboson beeinflussen, treten Korrelationen zwischen verschiedenen Operatoren auf. Betrachtet man die zweidimensionale Projektion des Wirkungsquerschnitts in Abhängigket von den Parametern zweier Operatoren, werden diese Korrelationen sichtbar.

Um nun auch quantitative Ergebnisse für die Sensitivität von $W^{\pm}\gamma$-Produktion in Vektorbosonstreuung angeben zu können, wurde folgendes Verfahren angewendet. Zuerst wurden Paare von zwei Operatoren gebildet und für bestimmten Werte der Parameter Histogramme berechnet. Unter der Annahme einer Luminosität von $L = 100$ fb^{-1} wurden die Bins dieser Histogramme so lange zusammengefasst, bis sie eine Mindestanzahl an Ereignissen enthielten. Dabei wurde vom rechten Ende der Histogramme begonnen, da hier die Abweichungen von den Standardmodellwerten am größten ist.
Nun wurde ein Paraboloid an die für bestimmte Werte der Kopplungsparameter berechneten Ereigniszahlen gefittet. Mit diesem Paraboloid und einem χ^2-Test konnten dann Konfidenzintervalle für die Parameter der verschiedenen Operatoren bestimmt werden. Diese hängen natürlich von den Histogrammen und den Details des Vorgehens bei der Zusammenfassung der Bins ab. Für bestimmte Parameter und Observablen konnten jedoch schon sehr vielversprechende Ausschlussgrenzen bestimmt werden.
Da bei dieser Analyse eine Beschleunigerenergie von $E_{CM} = 14$ TeV angenommen wurde, welche auch für den nächsten Lauf des LHCs im Jahr 2014 geplant ist, wird die $W^{\pm}\gamma$-Produktion in Vektorbosonstreuung schon bald eine wichtige Rolle bei der Suche nach „neuer Physik“ spielen.

APPENDIX

A. Dimension 8 operators

In this appendix all possible dimension 8 operators are listed. The parametrization of the operators follows the one proposed in [19]. All operators but $\mathcal{L}_{S,0}$, $\mathcal{L}_{S,1}$, $\mathcal{L}_{T,8}$ and $\mathcal{L}_{T,9}$ affect the $WW\gamma\gamma$ and $WWZ\gamma$ couplings that occur in $W\gamma$ production via VBF.

1. Operators containing only $D_\mu\phi$:

$$\mathcal{L}_{S,0} = \left[(D_\mu\phi)^\dagger D_\nu\phi\right] \times \left[(D^\mu\phi)^\dagger D^\nu\phi\right] \tag{7.1a}$$
$$\mathcal{L}_{S,1} = \left[(D_\mu\phi)^\dagger D^\mu\phi\right] \times \left[(D_\nu\phi)^\dagger D^\nu\phi\right] \tag{7.1b}$$

2. Operators containing $D_\mu\phi$, $\hat{W}_{\mu\nu}$ and $\hat{B}_{\mu\nu}$:

$$\mathcal{L}_{M,0} = \mathrm{Tr}\left[\hat{W}_{\mu\nu}\hat{W}^{\mu\nu}\right] \times \left[(D_\beta\phi)^\dagger D^\beta\phi\right] \tag{7.2a}$$
$$\mathcal{L}_{M,1} = \mathrm{Tr}\left[\hat{W}_{\mu\nu}\hat{W}^{\nu\beta}\right] \times \left[(D_\beta\phi)^\dagger D^\mu\phi\right] \tag{7.2b}$$
$$\mathcal{L}_{M,2} = \left[\hat{B}_{\mu\nu}\hat{B}^{\mu\nu}\right] \times \left[(D_\beta\phi)^\dagger D^\beta\phi\right] \tag{7.2c}$$
$$\mathcal{L}_{M,3} = \left[\hat{B}_{\mu\nu}\hat{B}^{\nu\beta}\right] \times \left[(D_\beta\phi)^\dagger D^\mu\phi\right] \tag{7.2d}$$
$$\mathcal{L}_{M,4} = \left[(D_\mu\phi)^\dagger \hat{W}_{\beta\nu} D^\mu\phi\right] \times \hat{B}^{\beta\nu} \tag{7.2e}$$
$$\mathcal{L}_{M,5} = \left[(D_\mu\phi)^\dagger \hat{W}_{\beta\nu} D^\nu\phi\right] \times \hat{B}^{\beta\mu} \tag{7.2f}$$
$$\mathcal{L}_{M,6} = \left[(D_\mu\phi)^\dagger \hat{W}_{\beta\nu}\hat{W}^{\beta\nu} D^\mu\phi\right] \tag{7.2g}$$
$$\mathcal{L}_{M,7} = \left[(D_\mu\phi)^\dagger \hat{W}_{\beta\nu}\hat{W}^{\beta\mu} D^\nu\phi\right] \tag{7.2h}$$

3. Operators containing $\hat{W}_{\mu\nu}$ and $\hat{B}_{\mu\nu}$:

$$\mathcal{L}_{T,0} = \mathrm{Tr}\left[\hat{W}_{\mu\nu}\hat{W}^{\mu\nu}\right] \times \mathrm{Tr}\left[\hat{W}_{\alpha\beta}\hat{W}^{\alpha\beta}\right] \tag{7.3a}$$

$$\mathcal{L}_{T,1} = \mathrm{Tr}\left[\hat{W}_{\alpha\nu}\hat{W}^{\mu\beta}\right] \times \mathrm{Tr}\left[\hat{W}_{\mu\beta}\hat{W}^{\alpha\nu}\right] \tag{7.3b}$$

$$\mathcal{L}_{T,2} = \mathrm{Tr}\left[\hat{W}_{\alpha\mu}\hat{W}^{\mu\beta}\right] \times \mathrm{Tr}\left[\hat{W}_{\beta\nu}\hat{W}^{\nu\alpha}\right] \tag{7.3c}$$

$$\mathcal{L}_{T,5} = \mathrm{Tr}\left[\hat{W}_{\mu\nu}\hat{W}^{\mu\nu}\right] \times \hat{B}_{\alpha\beta}\hat{B}^{\alpha\beta} \tag{7.3d}$$

$$\mathcal{L}_{T,6} = \mathrm{Tr}\left[\hat{W}_{\alpha\nu}\hat{W}^{\mu\beta}\right] \times \hat{B}_{\mu\beta}\hat{B}^{\alpha\nu} \tag{7.3e}$$

$$\mathcal{L}_{T,7} = \mathrm{Tr}\left[\hat{W}_{\alpha\mu}\hat{W}^{\mu\beta}\right] \times \hat{B}_{\beta\nu}\hat{B}^{\nu\alpha} \tag{7.3f}$$

$$\mathcal{L}_{T,8} = \hat{B}_{\mu\nu}\hat{B}^{\mu\nu}\hat{B}_{\alpha\beta}\hat{B}^{\alpha\beta} \tag{7.3g}$$

$$\mathcal{L}_{T,9} = \hat{B}_{\alpha\mu}\hat{B}^{\mu\beta}\hat{B}_{\beta\nu}\hat{B}^{\nu\alpha} \tag{7.3h}$$

B. Form factors

To prevent the anomalous couplings from violating unitarity, the form factor described in section 2.4.1 with an exponent of $n = 2$ and the following form factor mass scales has been used. These scales were determined in the diploma thesis of O. Schlimpert [44].

f_i	**25**	**50**	**100**	**200**	**400**	**600**	**800**	**1000**	**1500**	**2000**
$\mathcal{L}_{S,0}$	1310	1100	925	775	650	590	545	515	465	435
$\mathcal{L}_{S,1}$	1100	920	775	650	545	495	460	435	390	365
$\mathcal{L}_{M,0}$	1480	1240	1045	875	735	665	620	585	530	490
$\mathcal{L}_{M,1}$	2105	1765	1480	1240	1045	940	875	830	750	695
$\mathcal{L}_{M,2}$	3595	2995	2500	2095	1755	1585	1470	1390	1255	1170
$\mathcal{L}_{M,3}$	5260	4335	3595	2995	2500	2255	2095	1980	1785	1660
$\mathcal{L}_{M,4}$	3005	2510	2100	1760	1475	1330	1240	1170	1055	985
$\mathcal{L}_{M,5}$	4350	3605	3005	2510	2100	1895	1760	1660	1500	1395
$\mathcal{L}_{M,6}$	1765	1480	1240	1045	875	790	735	695	630	585
$\mathcal{L}_{M,7}$	2515	2105	1765	1480	1245	1120	1045	985	890	830
$\mathcal{L}_{T,0}$	1200	1010	850	710	600	540	500	475	430	400
$\mathcal{L}_{T,1}$	1295	1085	910	765	645	580	540	510	460	430
$\mathcal{L}_{T,2}$	1450	1215	1020	860	720	650	605	575	515	480
$\mathcal{L}_{T,5}$	5075	4185	3475	2895	2420	2180	2025	1915	1725	1605
$\mathcal{L}_{T,6}$	4185	3475	2895	2420	2025	1825	1700	1605	1450	1345
$\mathcal{L}_{T,7}$	5910	4845	4005	3330	2775	2500	2320	2190	1975	1835
$\mathcal{L}_{T,8}$	7115	5770	4740	3920	3260	2930	2720	2565	2310	2145
$\mathcal{L}_{T,9}$	9290	7360	5955	4880	4035	3615	3350	3160	2840	2635

f_i	**-25**	**-50**	**-100**	**-200**	**-400**	**-600**	**-800**	**-1000**	**-1500**	**-2000**
$\mathcal{L}_{S,0}$	1335	1120	940	790	665	600	560	530	475	445
$\mathcal{L}_{S,1}$	1120	940	790	665	560	505	470	445	400	370
$\mathcal{L}_{M,0}$	1480	1240	1045	875	735	665	620	585	530	490
$\mathcal{L}_{M,1}$	2105	1765	1480	1240	1045	940	875	830	750	695
$\mathcal{L}_{M,2}$	3595	2995	2500	2095	1755	1585	1470	1390	1255	1170
$\mathcal{L}_{M,3}$	5260	4335	3595	2995	2500	2255	2095	1980	1785	1660
$\mathcal{L}_{M,4}$	3005	2510	2100	1760	1475	1330	1240	1170	1055	985
$\mathcal{L}_{M,5}$	4350	3605	3005	2510	2100	1895	1760	1660	1500	1395
$\mathcal{L}_{M,6}$	1765	1480	1240	1045	875	790	735	695	630	585
$\mathcal{L}_{M,7}$	2515	2105	1765	1480	1245	1120	1045	985	890	830
$\mathcal{L}_{T,0}$	1200	1010	850	710	600	540	500	475	430	400
$\mathcal{L}_{T,1}$	1295	1085	910	765	645	580	540	510	460	430
$\mathcal{L}_{T,2}$	1620	1355	1140	955	805	725	675	640	575	535
$\mathcal{L}_{T,5}$	5075	4185	3475	2895	2420	2180	2025	1915	1725	1605
$\mathcal{L}_{T,6}$	4150	3445	2875	2400	2010	1815	1685	1590	1435	1335
$\mathcal{L}_{T,7}$	5030	4150	3445	2875	2400	2165	2010	1900	1715	1590
$\mathcal{L}_{T,8}$	7115	5770	4740	3920	3260	2930	2720	2565	2310	2145
$\mathcal{L}_{T,9}$	9290	7360	5955	4880	4035	3615	3350	3160	2840	2635

Table B.1: This table shows form factor scales for different parameters of the dimension 8 operators f_i in TeV^{-4}.

C. Sensitivity analysis

The tables in this sections give the exclusion limits for the parameters of the dimension 8 operators, that have been reached in the analysis described in section 5.8.3. The observables that were examined are listed in table C.2. Moreover, this table gives the range and the bin width $\Delta_{bin,\mathcal{O}}$ of the original histograms.

Observable $\mathcal{O}$	Range	Bin width $\Delta_{bin,\mathcal{O}}$
η_γ	0 – 4	0.04
η_l	0 – 4	0.04
η_{miss}	0 – 4	0.04
$min(p_T^l, p_T^\gamma)$	0 GeV – 300 GeV	3 GeV
$min(p_T^W, p_T^\gamma)$	0 GeV – 300 GeV	3 GeV
$m_{j_1 j_2}$	0 GeV – 7000 GeV	70 GeV
$m_{l\gamma}$	0 GeV – 2000 GeV	20 GeV
$m_T(W\gamma)$	0 GeV – 2500 GeV	25 GeV
$\phi_{l\gamma}$	0° – 180°	18°
p_T^γ	0 GeV – 600 GeV	6 GeV
$p_T^{j_1}$	0 GeV – 1000 GeV	10 GeV
$p_T^{j_2}$	0 GeV – 600 GeV	6 GeV
p_T^l	0 GeV – 600 GeV	6 GeV
p_T^{miss}	0 GeV – 600 GeV	6 GeV

Table C.2: This table gives the observables, for which the sensitivity analysis has been conducted and the range and bin width of the original histograms.

For each pair of operators that have been examined the results are given for two setups: $N_{min} = 20$, $N_{min}^{bin} = 4$ and $N_{min} = 30$, $N_{min}^{bin} = 3$. The exclusion limits are given at the 90%, 95% and 99% confidence levels. Empty fields indicate that it was not possible to determine an exclusion limit within the examined range of $f_x \in [-1500, 1500]\,\mathrm{TeV}^{-4}$.

C.1. $\mathcal{L}_{T,0} - \mathcal{L}_{T,1}$

N_{min}	N_{min}^{bin}	Observable	CL	Bins	Area [TeV^{-8}]	$f_{T,0}$ [TeV^{-4}]	$f_{T,1}$ [TeV^{-4}]
20	4	η_γ	90.0%	13	35325325.0	-790.0 – 950.0	-485.0 – 985.0
20	4	η_γ	95.0%	13	40151800.0	-855.0 – 1015.0	-535.0 – 1030.0
20	4	η_γ	99.0%	13	48251800.0	-955.0 – 1115.0	-610.0 – 1110.0
20	4	η_l	90.0%	13	36882925.0	-795.0 – 950.0	-495.0 – 1000.0
20	4	η_l	95.0%	13	41836025.0	-860.0 – 1015.0	-545.0 – 1045.0
20	4	η_l	99.0%	13	50156575.0	-960.0 – 1115.0	-625.0 – 1125.0
20	4	η_{miss}	90.0%	13	36882925.0	-795.0 – 950.0	-495.0 – 1000.0
20	4	η_{miss}	95.0%	13	41836025.0	-860.0 – 1015.0	-545.0 – 1045.0
20	4	η_{miss}	99.0%	13	50156575.0	-960.0 – 1115.0	-625.0 – 1125.0
20	4	$min(p_T^l, p_T^\gamma)$	90.0%	8	41476675.0	-460.0 – 565.0	-300.0 – 575.0
20	4	$min(p_T^l, p_T^\gamma)$	95.0%	8	44375150.0	-495.0 – 605.0	-330.0 – 605.0
20	4	$min(p_T^l, p_T^\gamma)$	99.0%	8	48665800.0	-560.0 – 665.0	-375.0 – 655.0
20	4	$min(p_T^W, p_T^\gamma)$	90.0%	11	72979525.0	-500.0 – 635.0	-300.0 – 665.0
20	4	$min(p_T^W, p_T^\gamma)$	95.0%	11	75432350.0	-540.0 – 675.0	-330.0 – 700.0
20	4	$min(p_T^W, p_T^\gamma)$	99.0%	11	78917950.0	-610.0 – 740.0	-380.0 – 750.0
20	4	$m_{j_1 j_2}$	90.0%	11	45997100.0	-700.0 – 790.0	-475.0 – 930.0
20	4	$m_{j_1 j_2}$	95.0%	11	49645450.0	-755.0 – 845.0	-520.0 – 980.0
20	4	$m_{j_1 j_2}$	99.0%	11	55609700.0	-845.0 – 935.0	-595.0 – 1055.0
20	4	$m_{l\gamma}$	90.0%	7	30152725.0	-600.0 – 830.0	-325.0 – 590.0
20	4	$m_{l\gamma}$	95.0%	7	31925750.0	-655.0 – 885.0	-355.0 – 625.0
20	4	$m_{l\gamma}$	99.0%	7	34895250.0	-745.0 – 975.0	-410.0 – 680.0
20	4	$m_T(W\gamma)$	90.0%	6	23588025.0	-570.0 – 795.0	-275.0 – 590.0
20	4	$m_T(W\gamma)$	95.0%	6	25367325.0	-620.0 – 850.0	-305.0 – 620.0
20	4	$m_T(W\gamma)$	99.0%	6	28087950.0	-705.0 – 935.0	-355.0 – 670.0
20	4	$\phi_{l\gamma}$	90.0%	13	52932375.0	-885.0 – 875.0	-590.0 – 1120.0
20	4	$\phi_{l\gamma}$	95.0%	13	59487075.0	-950.0 – 940.0	-645.0 – 1180.0
20	4	$\phi_{l\gamma}$	99.0%	13	69760375.0	-1060.0 – 1050.0	-735.0 – 1275.0
20	4	p_T^γ	90.0%	8	10419300.0	-420.0 – 500.0	-260.0 – 530.0
20	4	p_T^γ	95.0%	8	12073450.0	-455.0 – 535.0	-285.0 – 560.0
20	4	p_T^γ	99.0%	8	15011575.0	-515.0 – 590.0	-330.0 – 605.0
20	4	$p_T^{j_1}$	90.0%	9	45510700.0	-495.0 – 530.0	-310.0 – 450.0
20	4	$p_T^{j_1}$	95.0%	9	48295775.0	-530.0 – 570.0	-335.0 – 475.0
20	4	$p_T^{j_1}$	99.0%	9	52517275.0	-595.0 – 630.0	-380.0 – 525.0
20	4	$p_T^{j_2}$	90.0%	8	24385450.0	-710.0 – 875.0	-455.0 – 945.0
20	4	$p_T^{j_2}$	95.0%	8	27444325.0	-765.0 – 935.0	-505.0 – 990.0
20	4	$p_T^{j_2}$	99.0%	8	32569525.0	-865.0 – 1030.0	-580.0 – 1065.0
20	4	p_T^l	90.0%	7	26886775.0	-555.0 – 630.0	-350.0 – 580.0
20	4	p_T^l	95.0%	7	29599025.0	-600.0 – 675.0	-380.0 – 615.0
20	4	p_T^l	99.0%	7	33910675.0	-670.0 – 745.0	-435.0 – 675.0
20	4	p_T^{miss}	90.0%	8	27060375.0	-625.0 – 700.0	-360.0 – 820.0
20	4	p_T^{miss}	95.0%	8	30709525.0	-675.0 – 750.0	-400.0 – 860.0
20	4	p_T^{miss}	99.0%	8	36562925.0	-755.0 – 830.0	-460.0 – 920.0

N_{min}	N_{min}^{bin}	Observable	CL	Bins	Area [TeV^{-8}]	$f_{T,0}$ [TeV^{-4}]	$f_{T,1}$ [TeV^{-4}]
30	3	η_γ	90.0%	16	47611200.0	-810.0 – 970.0	-500.0 – 1000.0
30	3	η_γ	95.0%	16	53705525.0	-875.0 – 1035.0	-550.0 – 1045.0
30	3	η_γ	99.0%	16	63940350.0	-975.0 – 1135.0	-625.0 – 1125.0
30	3	η_l	90.0%	15	42947475.0	-810.0 – 965.0	-505.0 – 1010.0
30	3	η_l	95.0%	15	48779650.0	-875.0 – 1030.0	-555.0 – 1055.0
30	3	η_l	99.0%	15	58567950.0	-975.0 – 1130.0	-635.0 – 1135.0
30	3	η_{miss}	90.0%	15	42947475.0	-810.0 – 965.0	-505.0 – 1010.0
30	3	η_{miss}	95.0%	15	48779650.0	-875.0 – 1030.0	-555.0 – 1055.0
30	3	η_{miss}	99.0%	15	58567950.0	-975.0 – 1130.0	-635.0 – 1135.0
30	3	$min(p_T^l, p_T^\gamma)$	90.0%	8	45382275.0	-480.0 – 595.0	-310.0 – 610.0
30	3	$min(p_T^l, p_T^\gamma)$	95.0%	8	48293850.0	-520.0 – 635.0	-340.0 – 640.0
30	3	$min(p_T^l, p_T^\gamma)$	99.0%	8	52393600.0	-585.0 – 700.0	-390.0 – 695.0
30	3	$min(p_T^W, p_T^\gamma)$	90.0%	11	78818275.0	-515.0 – 660.0	-310.0 – 695.0
30	3	$min(p_T^W, p_T^\gamma)$	95.0%	11	80872425.0	-555.0 – 700.0	-340.0 – 730.0
30	3	$min(p_T^W, p_T^\gamma)$	99.0%	11	83718375.0	-625.0 – 770.0	-390.0 – 780.0
30	3	$m_{j_1 j_2}$	90.0%	11	47492475.0	-700.0 – 790.0	-475.0 – 930.0
30	3	$m_{j_1 j_2}$	95.0%	11	51507425.0	-755.0 – 845.0	-520.0 – 980.0
30	3	$m_{j_1 j_2}$	99.0%	11	57790575.0	-845.0 – 935.0	-595.0 – 1055.0
30	3	$m_{l\gamma}$	90.0%	7	31625475.0	-605.0 – 840.0	-325.0 – 600.0
30	3	$m_{l\gamma}$	95.0%	7	33609200.0	-660.0 – 890.0	-360.0 – 635.0
30	3	$m_{l\gamma}$	99.0%	7	36854950.0	-745.0 – 980.0	-410.0 – 690.0
30	3	$m_T(W\gamma)$	90.0%	6	26206400.0	-570.0 – 800.0	-280.0 – 605.0
30	3	$m_T(W\gamma)$	95.0%	6	27964775.0	-620.0 – 850.0	-310.0 – 635.0
30	3	$m_T(W\gamma)$	99.0%	6	30583125.0	-705.0 – 935.0	-360.0 – 685.0
30	3	$\phi_{l\gamma}$	90.0%	11	40368625.0	-875.0 – 865.0	-575.0 – 1110.0
30	3	$\phi_{l\gamma}$	95.0%	11	45961875.0	-940.0 – 930.0	-630.0 – 1165.0
30	3	$\phi_{l\gamma}$	99.0%	11	55131875.0	-1045.0 – 1035.0	-725.0 – 1260.0
30	3	p_T^γ	90.0%	8	13934150.0	-440.0 – 530.0	-265.0 – 565.0
30	3	p_T^γ	95.0%	8	16139825.0	-475.0 – 565.0	-295.0 – 595.0
30	3	p_T^γ	99.0%	8	20055425.0	-535.0 – 625.0	-340.0 – 640.0
30	3	$p_T^{j_1}$	90.0%	9	48406600.0	-520.0 – 550.0	-320.0 – 475.0
30	3	$p_T^{j_1}$	95.0%	9	51186825.0	-560.0 – 590.0	-350.0 – 505.0
30	3	$p_T^{j_1}$	99.0%	9	55319100.0	-625.0 – 655.0	-395.0 – 555.0
30	3	$p_T^{j_2}$	90.0%	8	25657400.0	-715.0 – 890.0	-460.0 – 950.0
30	3	$p_T^{j_2}$	95.0%	8	28900200.0	-775.0 – 950.0	-505.0 – 995.0
30	3	$p_T^{j_2}$	99.0%	8	34271100.0	-870.0 – 1045.0	-580.0 – 1075.0
30	3	p_T^l	90.0%	8	38912125.0	-570.0 – 655.0	-360.0 – 610.0
30	3	p_T^l	95.0%	8	41853575.0	-620.0 – 700.0	-395.0 – 650.0
30	3	p_T^l	99.0%	8	46336075.0	-690.0 – 775.0	-455.0 – 705.0
30	3	p_T^{miss}	90.0%	8	29084700.0	-640.0 – 720.0	-365.0 – 830.0
30	3	p_T^{miss}	95.0%	8	32997150.0	-690.0 – 775.0	-405.0 – 870.0
30	3	p_T^{miss}	99.0%	8	39189950.0	-770.0 – 855.0	-470.0 – 935.0

C.2. $\mathcal{L}_{T,0} - \mathcal{L}_{T,5}$

N_{min}	N_{min}^{bin}	Observable	CL	Bins	Area [TeV^{-8}]	$f_{T,0}$ [TeV^{-4}]	$f_{T,5}$ [TeV^{-4}]
20	4	η_γ	90.0%	13	58133175.0	-755.0 – 905.0	-1370.0 – 1420.0
20	4	η_γ	95.0%	13		-815.0 – 965.0	
20	4	η_γ	99.0%	13		-915.0 – 1060.0	
20	4	η_l	90.0%	13	58607950.0	-765.0 – 910.0	-1370.0 – 1420.0
20	4	η_l	95.0%	13		-825.0 – 970.0	
20	4	η_l	99.0%	13		-920.0 – 1070.0	
20	4	η_{miss}	90.0%	13	58607950.0	-765.0 – 910.0	-1370.0 – 1420.0
20	4	η_{miss}	95.0%	13		-825.0 – 970.0	
20	4	η_{miss}	99.0%	13		-920.0 – 1070.0	
20	4	$min(p_T^l, p_T^\gamma)$	90.0%	8	16641750.0	-405.0 – 480.0	-575.0 – 595.0
20	4	$min(p_T^l, p_T^\gamma)$	95.0%	8	17832625.0	-440.0 – 515.0	-620.0 – 640.0
20	4	$min(p_T^l, p_T^\gamma)$	99.0%	8	19950600.0	-495.0 – 565.0	-690.0 – 710.0
20	4	$min(p_T^W, p_T^\gamma)$	90.0%	11	31364300.0	-450.0 – 545.0	-665.0 – 690.0
20	4	$min(p_T^W, p_T^\gamma)$	95.0%	11	33404950.0	-485.0 – 585.0	-710.0 – 735.0
20	4	$min(p_T^W, p_T^\gamma)$	99.0%	11	36992225.0	-545.0 – 645.0	-790.0 – 815.0
20	4	$m_{j_1 j_2}$	90.0%	11	63509750.0	-680.0 – 770.0	-1290.0 – 1330.0
20	4	$m_{j_1 j_2}$	95.0%	11	67888350.0	-735.0 – 825.0	-1390.0 – 1430.0
20	4	$m_{j_1 j_2}$	99.0%	11		-820.0 – 910.0	
20	4	$m_{l\gamma}$	90.0%	7	15932575.0	-480.0 – 575.0	-605.0 – 620.0
20	4	$m_{l\gamma}$	95.0%	7	17024750.0	-520.0 – 615.0	-650.0 – 665.0
20	4	$m_{l\gamma}$	99.0%	7	18976625.0	-585.0 – 685.0	-725.0 – 745.0
20	4	$m_T(W\gamma)$	90.0%	6	13576450.0	-435.0 – 515.0	-550.0 – 560.0
20	4	$m_T(W\gamma)$	95.0%	6	14305125.0	-475.0 – 550.0	-590.0 – 605.0
20	4	$m_T(W\gamma)$	99.0%	6	15613950.0	-535.0 – 615.0	-660.0 – 675.0
20	4	$\phi_{l\gamma}$	90.0%	13		-865.0 – 870.0	
20	4	$\phi_{l\gamma}$	95.0%	13		-930.0 – 935.0	
20	4	$\phi_{l\gamma}$	99.0%	13		-1035.0 – 1040.0	
20	4	p_T^γ	90.0%	8	9187150.0	-395.0 – 465.0	-570.0 – 590.0
20	4	p_T^γ	95.0%	8	10627900.0	-430.0 – 500.0	-615.0 – 635.0
20	4	p_T^γ	99.0%	8	13185950.0	-480.0 – 550.0	-685.0 – 705.0
20	4	$p_T^{j_1}$	90.0%	9	59726225.0	-465.0 – 505.0	-755.0 – 795.0
20	4	$p_T^{j_1}$	95.0%	9	62729225.0	-505.0 – 545.0	-815.0 – 850.0
20	4	$p_T^{j_1}$	99.0%	9	66638150.0	-565.0 – 605.0	-905.0 – 945.0
20	4	$p_T^{j_2}$	90.0%	8	13058225.0	-590.0 – 675.0	-740.0 – 765.0
20	4	$p_T^{j_2}$	95.0%	8	15103000.0	-640.0 – 720.0	-800.0 – 820.0
20	4	$p_T^{j_2}$	99.0%	8	18737750.0	-715.0 – 800.0	-890.0 – 910.0
20	4	p_T^l	90.0%	7	39492850.0	-525.0 – 600.0	-920.0 – 955.0
20	4	p_T^l	95.0%	7	42255500.0	-570.0 – 645.0	-990.0 – 1025.0
20	4	p_T^l	99.0%	7	46309150.0	-640.0 – 715.0	-1105.0 – 1140.0
20	4	p_T^{miss}	90.0%	8	42282800.0	-600.0 – 670.0	-1095.0 – 1130.0
20	4	p_T^{miss}	95.0%	8	46437950.0	-645.0 – 720.0	-1180.0 – 1210.0
20	4	p_T^{miss}	99.0%	8	52442875.0	-725.0 – 795.0	-1315.0 – 1345.0

N_{min}	N_{min}^{bin}	Observable	CL	Bins	Area [TeV^{-8}]	$f_{T,0}$ [TeV^{-4}]	$f_{T,5}$ [TeV^{-4}]
30	3	η_γ	90.0%	16	76619400.0	-775.0 – 920.0	-1400.0 – 1450.0
30	3	η_γ	95.0%	16		-835.0 – 985.0	
30	3	η_γ	99.0%	16		-935.0 – 1080.0	
30	3	η_l	90.0%	15	68876625.0	-775.0 – 925.0	-1395.0 – 1445.0
30	3	η_l	95.0%	15		-835.0 – 985.0	
30	3	η_l	99.0%	15		-935.0 – 1085.0	
30	3	η_{miss}	90.0%	15	68876625.0	-775.0 – 925.0	-1395.0 – 1445.0
30	3	η_{miss}	95.0%	15		-835.0 – 985.0	
30	3	η_{miss}	99.0%	15		-935.0 – 1085.0	
30	3	$min(p_T^l, p_T^\gamma)$	90.0%	8	17650175.0	-425.0 – 505.0	-610.0 – 630.0
30	3	$min(p_T^l, p_T^\gamma)$	95.0%	8	18997475.0	-460.0 – 540.0	-655.0 – 675.0
30	3	$min(p_T^l, p_T^\gamma)$	99.0%	8	21396500.0	-520.0 – 600.0	-730.0 – 755.0
30	3	$min(p_T^W, p_T^\gamma)$	90.0%	11	37738050.0	-475.0 – 595.0	-795.0 – 825.0
30	3	$min(p_T^W, p_T^\gamma)$	95.0%	11	40751800.0	-515.0 – 635.0	-855.0 – 885.0
30	3	$min(p_T^W, p_T^\gamma)$	99.0%	11	46056775.0	-580.0 – 695.0	-950.0 – 985.0
30	3	$m_{j_1 j_2}$	90.0%	11	66346125.0	-680.0 – 770.0	-1295.0 – 1335.0
30	3	$m_{j_1 j_2}$	95.0%	11	70821175.0	-735.0 – 825.0	-1390.0 – 1430.0
30	3	$m_{j_1 j_2}$	99.0%	11		-820.0 – 910.0	
30	3	$m_{l\gamma}$	90.0%	7	14933350.0	-450.0 – 515.0	-555.0 – 570.0
30	3	$m_{l\gamma}$	95.0%	7	15867725.0	-490.0 – 555.0	-595.0 – 615.0
30	3	$m_{l\gamma}$	99.0%	7	17535900.0	-550.0 – 615.0	-665.0 – 685.0
30	3	$m_T(W\gamma)$	90.0%	6	14108475.0	-450.0 – 540.0	-570.0 – 590.0
30	3	$m_T(W\gamma)$	95.0%	6	14921625.0	-490.0 – 580.0	-615.0 – 635.0
30	3	$m_T(W\gamma)$	99.0%	6	16383375.0	-555.0 – 645.0	-690.0 – 705.0
30	3	$\phi_{l\gamma}$	90.0%	11		-855.0 – 860.0	
30	3	$\phi_{l\gamma}$	95.0%	11		-920.0 – 925.0	
30	3	$\phi_{l\gamma}$	99.0%	11		-1025.0 – 1025.0	
30	3	p_T^γ	90.0%	8	10895525.0	-410.0 – 490.0	-605.0 – 630.0
30	3	p_T^γ	95.0%	8	12601675.0	-445.0 – 525.0	-655.0 – 675.0
30	3	p_T^γ	99.0%	8	15634475.0	-495.0 – 580.0	-730.0 – 750.0
30	3	$p_T^{j_1}$	90.0%	9	62855825.0	-490.0 – 525.0	-800.0 – 835.0
30	3	$p_T^{j_1}$	95.0%	9	65598575.0	-530.0 – 565.0	-860.0 – 895.0
30	3	$p_T^{j_1}$	99.0%	9	69091800.0	-590.0 – 625.0	-960.0 – 995.0
30	3	$p_T^{j_2}$	90.0%	8	13202425.0	-595.0 – 680.0	-745.0 – 765.0
30	3	$p_T^{j_2}$	95.0%	8	15269475.0	-640.0 – 725.0	-800.0 – 820.0
30	3	$p_T^{j_2}$	99.0%	8	18943550.0	-720.0 – 805.0	-890.0 – 910.0
30	3	p_T^l	90.0%	8	51713975.0	-545.0 – 625.0	-965.0 – 1005.0
30	3	p_T^l	95.0%	8	54556925.0	-590.0 – 670.0	-1040.0 – 1080.0
30	3	p_T^l	99.0%	8	58441250.0	-660.0 – 740.0	-1160.0 – 1200.0
30	3	p_T^{miss}	90.0%	8	44822125.0	-610.0 – 690.0	-1110.0 – 1145.0
30	3	p_T^{miss}	95.0%	8	49018500.0	-660.0 – 740.0	-1195.0 – 1230.0
30	3	p_T^{miss}	99.0%	8	54967575.0	-735.0 – 820.0	-1330.0 – 1370.0

C.3. $\mathcal{L}_{T,0} - \mathcal{L}_{T,6}$

N_{min}	N_{min}^{bin}	Observable	CL	Bins	Area [TeV^{-8}]	$f_{T,0}$ [TeV^{-4}]	$f_{T,6}$[TeV^{-4}]
20	4	η_γ	90.0%	13	54113200.0	-770.0 – 925.0	-1190.0 – 1360.0
20	4	η_γ	95.0%	13	61332725.0	-830.0 – 985.0	-1280.0 – 1450.0
20	4	η_γ	99.0%	13		-930.0 – 1085.0	
20	4	η_l	90.0%	13	55506100.0	-775.0 – 925.0	-1205.0 – 1375.0
20	4	η_l	95.0%	13	62726850.0	-835.0 – 990.0	-1300.0 – 1470.0
20	4	η_l	99.0%	13		-935.0 – 1085.0	
20	4	η_{miss}	90.0%	13	55506100.0	-775.0 – 925.0	-1205.0 – 1375.0
20	4	η_{miss}	95.0%	13	62726850.0	-835.0 – 990.0	-1300.0 – 1470.0
20	4	η_{miss}	99.0%	13		-935.0 – 1085.0	
20	4	$min(p_T^l, p_T^\gamma)$	90.0%	8	16597300.0	-410.0 – 485.0	-555.0 – 595.0
20	4	$min(p_T^l, p_T^\gamma)$	95.0%	8	17781950.0	-445.0 – 520.0	-595.0 – 635.0
20	4	$min(p_T^l, p_T^\gamma)$	99.0%	8	19887650.0	-500.0 – 570.0	-665.0 – 705.0
20	4	$min(p_T^W, p_T^\gamma)$	90.0%	11	31352275.0	-450.0 – 550.0	-640.0 – 695.0
20	4	$min(p_T^W, p_T^\gamma)$	95.0%	11	33390050.0	-490.0 – 585.0	-690.0 – 745.0
20	4	$min(p_T^W, p_T^\gamma)$	99.0%	11	36976525.0	-545.0 – 645.0	-765.0 – 820.0
20	4	$m_{j_1 j_2}$	90.0%	11	61649925.0	-685.0 – 775.0	-1155.0 – 1310.0
20	4	$m_{j_1 j_2}$	95.0%	11	66245325.0	-740.0 – 830.0	-1245.0 – 1400.0
20	4	$m_{j_1 j_2}$	99.0%	11		-825.0 – 915.0	
20	4	$m_{l\gamma}$	90.0%	7	14494050.0	-440.0 – 500.0	-520.0 – 545.0
20	4	$m_{l\gamma}$	95.0%	7	15358875.0	-480.0 – 535.0	-560.0 – 585.0
20	4	$m_{l\gamma}$	99.0%	7	16903475.0	-540.0 – 595.0	-625.0 – 655.0
20	4	$m_T(W\gamma)$	90.0%	6	13565450.0	-440.0 – 515.0	-525.0 – 555.0
20	4	$m_T(W\gamma)$	95.0%	6	14293200.0	-480.0 – 550.0	-565.0 – 600.0
20	4	$m_T(W\gamma)$	99.0%	6	15599050.0	-540.0 – 615.0	-635.0 – 665.0
20	4	$\phi_{l\gamma}$	90.0%	13		-865.0 – 860.0	
20	4	$\phi_{l\gamma}$	95.0%	13		-930.0 – 925.0	
20	4	$\phi_{l\gamma}$	99.0%	13		-1030.0 – 1030.0	
20	4	p_T^γ	90.0%	8	9168500.0	-400.0 – 475.0	-540.0 – 590.0
20	4	p_T^γ	95.0%	8	10605050.0	-430.0 – 505.0	-580.0 – 630.0
20	4	p_T^γ	99.0%	8	13159000.0	-485.0 – 560.0	-650.0 – 700.0
20	4	$p_T^{j_1}$	90.0%	9	58208525.0	-475.0 – 515.0	-685.0 – 730.0
20	4	$p_T^{j_1}$	95.0%	9	61544325.0	-510.0 – 550.0	-735.0 – 785.0
20	4	$p_T^{j_1}$	99.0%	9	65944300.0	-570.0 – 610.0	-820.0 – 870.0
20	4	$p_T^{j_2}$	90.0%	8	12849975.0	-595.0 – 680.0	-720.0 – 750.0
20	4	$p_T^{j_2}$	95.0%	8	14862975.0	-640.0 – 725.0	-775.0 – 805.0
20	4	$p_T^{j_2}$	99.0%	8	18439675.0	-720.0 – 805.0	-865.0 – 895.0
20	4	p_T^l	90.0%	7	38670275.0	-535.0 – 610.0	-820.0 – 920.0
20	4	p_T^l	95.0%	7	41622850.0	-580.0 – 655.0	-885.0 – 985.0
20	4	p_T^l	99.0%	7	45865000.0	-650.0 – 725.0	-990.0 – 1090.0
20	4	p_T^{miss}	90.0%	8	40252875.0	-620.0 – 680.0	-815.0 – 855.0
20	4	p_T^{miss}	95.0%	8	44228525.0	-670.0 – 730.0	-880.0 – 915.0
20	4	p_T^{miss}	99.0%	8	50130450.0	-750.0 – 810.0	-985.0 – 1020.0

N_{min}	N_{min}^{bin}	Observable	CL	Bins	Area [TeV^{-8}]	$f_{T,0}$ [TeV^{-4}]	$f_{T,6}$ [TeV^{-4}]
30	3	η_γ	90.0%	16	71866150.0	-785.0 – 940.0	-1215.0 – 1385.0
30	3	η_γ	95.0%	16	80600450.0	-850.0 – 1005.0	-1310.0 – 1480.0
30	3	η_γ	99.0%	16		-950.0 – 1105.0	
30	3	η_l	90.0%	15	65207350.0	-785.0 – 940.0	-1225.0 – 1395.0
30	3	η_l	95.0%	15	73615525.0	-850.0 – 1000.0	-1320.0 – 1490.0
30	3	η_l	99.0%	15		-950.0 – 1100.0	
30	3	η_{miss}	90.0%	15	65207350.0	-785.0 – 940.0	-1225.0 – 1395.0
30	3	η_{miss}	95.0%	15	73615525.0	-850.0 – 1000.0	-1320.0 – 1490.0
30	3	η_{miss}	99.0%	15		-950.0 – 1100.0	
30	3	$min(p_T^l, p_T^\gamma)$	90.0%	8	17600100.0	-430.0 – 510.0	-585.0 – 630.0
30	3	$min(p_T^l, p_T^\gamma)$	95.0%	8	18942150.0	-465.0 – 545.0	-630.0 – 675.0
30	3	$min(p_T^l, p_T^\gamma)$	99.0%	8	21325025.0	-525.0 – 605.0	-705.0 – 750.0
30	3	$min(p_T^W, p_T^\gamma)$	90.0%	11	33876250.0	-470.0 – 580.0	-685.0 – 750.0
30	3	$min(p_T^W, p_T^\gamma)$	95.0%	11	36299050.0	-505.0 – 615.0	-740.0 – 805.0
30	3	$min(p_T^W, p_T^\gamma)$	99.0%	11	40562975.0	-570.0 – 680.0	-825.0 – 890.0
30	3	$m_{j_1 j_2}$	90.0%	11	64451450.0	-685.0 – 775.0	-1155.0 – 1310.0
30	3	$m_{j_1 j_2}$	95.0%	11	69244250.0	-740.0 – 830.0	-1245.0 – 1400.0
30	3	$m_{j_1 j_2}$	99.0%	11		-825.0 – 915.0	
30	3	$m_{l\gamma}$	90.0%	7	14928125.0	-455.0 – 520.0	-540.0 – 570.0
30	3	$m_{l\gamma}$	95.0%	7	15860950.0	-490.0 – 555.0	-580.0 – 610.0
30	3	$m_{l\gamma}$	99.0%	7	17529925.0	-555.0 – 620.0	-650.0 – 680.0
30	3	$m_T(W\gamma)$	90.0%	6	14094650.0	-455.0 – 540.0	-545.0 – 585.0
30	3	$m_T(W\gamma)$	95.0%	6	14907175.0	-495.0 – 580.0	-590.0 – 625.0
30	3	$m_T(W\gamma)$	99.0%	6	16364600.0	-560.0 – 645.0	-660.0 – 700.0
30	3	$\phi_{l\gamma}$	90.0%	11		-850.0 – 850.0	
30	3	$\phi_{l\gamma}$	95.0%	11		-915.0 – 915.0	
30	3	$\phi_{l\gamma}$	99.0%	11		-1020.0 – 1015.0	
30	3	p_T^γ	90.0%	8	10873575.0	-415.0 – 495.0	-570.0 – 630.0
30	3	p_T^γ	95.0%	8	12576575.0	-445.0 – 530.0	-615.0 – 675.0
30	3	p_T^γ	99.0%	8	15604250.0	-500.0 – 585.0	-690.0 – 750.0
30	3	$p_T^{j_1}$	90.0%	9	61509100.0	-500.0 – 535.0	-720.0 – 775.0
30	3	$p_T^{j_1}$	95.0%	9	64620425.0	-535.0 – 570.0	-775.0 – 830.0
30	3	$p_T^{j_1}$	99.0%	9	68519550.0	-600.0 – 635.0	-865.0 – 920.0
30	3	$p_T^{j_2}$	90.0%	8	12992650.0	-595.0 – 685.0	-720.0 – 750.0
30	3	$p_T^{j_2}$	95.0%	8	15027850.0	-645.0 – 730.0	-775.0 – 805.0
30	3	$p_T^{j_2}$	99.0%	8	18647000.0	-725.0 – 810.0	-865.0 – 895.0
30	3	p_T^l	90.0%	8	51109850.0	-550.0 – 635.0	-855.0 – 965.0
30	3	p_T^l	95.0%	8	54111775.0	-595.0 – 680.0	-925.0 – 1035.0
30	3	p_T^l	99.0%	8	58119525.0	-670.0 – 750.0	-1035.0 – 1145.0
30	3	p_T^{miss}	90.0%	8	44298550.0	-620.0 – 710.0	-920.0 – 1085.0
30	3	p_T^{miss}	95.0%	8	48477950.0	-670.0 – 760.0	-995.0 – 1160.0
30	3	p_T^{miss}	99.0%	8	54479725.0	-750.0 – 840.0	-1115.0 – 1280.0

C.4. $\mathcal{L}_{T,1} - \mathcal{L}_{T,5}$

N_{min}	N_{min}^{bin}	Observable	CL	Bins	Area [TeV^{-8}]	$f_{T,1}$ [TeV^{-4}]	$f_{T,5}$ [TeV^{-4}]
20	4	η_γ	90.0%	13	51299000.0	-490.0 – 1060.0	-1230.0 – 1275.0
20	4	η_γ	95.0%	13	57155350.0	-535.0 – 1110.0	-1320.0 – 1365.0
20	4	η_γ	99.0%	13		-615.0 – 1190.0	
20	4	η_l	90.0%	13	53587825.0	-500.0 – 1080.0	-1230.0 – 1280.0
20	4	η_l	95.0%	13	59554650.0	-550.0 – 1130.0	-1325.0 – 1370.0
20	4	η_l	99.0%	13		-630.0 – 1210.0	
20	4	η_{miss}	90.0%	13	53587825.0	-500.0 – 1080.0	-1230.0 – 1280.0
20	4	η_{miss}	95.0%	13	59554650.0	-550.0 – 1130.0	-1325.0 – 1370.0
20	4	η_{miss}	99.0%	13		-630.0 – 1210.0	
20	4	$min(p_T^l, p_T^\gamma)$	90.0%	8	48358375.0	-295.0 – 605.0	-755.0 – 800.0
20	4	$min(p_T^l, p_T^\gamma)$	95.0%	8	50568825.0	-325.0 – 640.0	-815.0 – 860.0
20	4	$min(p_T^l, p_T^\gamma)$	99.0%	8	54028500.0	-375.0 – 690.0	-910.0 – 955.0
20	4	$min(p_T^W, p_T^\gamma)$	90.0%	11	79338625.0	-290.0 – 690.0	-905.0 – 965.0
20	4	$min(p_T^W, p_T^\gamma)$	95.0%	11	81225375.0	-320.0 – 725.0	-970.0 – 1035.0
20	4	$min(p_T^W, p_T^\gamma)$	99.0%	11	84038550.0	-370.0 – 775.0	-1080.0 – 1145.0
20	4	$m_{j_1 j_2}$	90.0%	11	54401875.0	-475.0 – 1000.0	-1165.0 – 1205.0
20	4	$m_{j_1 j_2}$	95.0%	11	58761275.0	-525.0 – 1045.0	-1255.0 – 1290.0
20	4	$m_{j_1 j_2}$	99.0%	11	65402650.0	-600.0 – 1125.0	-1395.0 – 1435.0
20	4	$m_{l\gamma}$	90.0%	7	38300050.0	-320.0 – 660.0	-645.0 – 690.0
20	4	$m_{l\gamma}$	95.0%	7	39814825.0	-355.0 – 695.0	-695.0 – 740.0
20	4	$m_{l\gamma}$	99.0%	7	42228075.0	-410.0 – 755.0	-780.0 – 820.0
20	4	$m_T(W\gamma)$	90.0%	6	31902075.0	-270.0 – 665.0	-590.0 – 630.0
20	4	$m_T(W\gamma)$	95.0%	6	33408625.0	-300.0 – 695.0	-640.0 – 675.0
20	4	$m_T(W\gamma)$	99.0%	6	35086950.0	-350.0 – 745.0	-715.0 – 750.0
20	4	$\phi_{l\gamma}$	90.0%	13	89658925.0	-595.0 – 1200.0	-1370.0 – 1450.0
20	4	$\phi_{l\gamma}$	95.0%	13		-655.0 – 1265.0	
20	4	$\phi_{l\gamma}$	99.0%	13		-750.0 – 1365.0	
20	4	p_T^γ	90.0%	8	10898900.0	-255.0 – 560.0	-575.0 – 600.0
20	4	p_T^γ	95.0%	8	12642950.0	-280.0 – 590.0	-620.0 – 645.0
20	4	p_T^γ	99.0%	8	15737025.0	-325.0 – 640.0	-690.0 – 715.0
20	4	$p_T^{j_1}$	90.0%	9	47879575.0	-310.0 – 475.0	-625.0 – 650.0
20	4	$p_T^{j_1}$	95.0%	9	50870575.0	-340.0 – 505.0	-675.0 – 700.0
20	4	$p_T^{j_1}$	99.0%	9	55117625.0	-385.0 – 555.0	-750.0 – 775.0
20	4	$p_T^{j_2}$	90.0%	8	31868325.0	-455.0 – 1005.0	-1175.0 – 1225.0
20	4	$p_T^{j_2}$	95.0%	8	35652150.0	-505.0 – 1055.0	-1265.0 – 1315.0
20	4	$p_T^{j_2}$	99.0%	8	41532575.0	-580.0 – 1130.0	-1415.0 – 1460.0
20	4	p_T^l	90.0%	7	34333900.0	-350.0 – 630.0	-745.0 – 775.0
20	4	p_T^l	95.0%	7	36704000.0	-385.0 – 665.0	-805.0 – 830.0
20	4	p_T^l	99.0%	7	40337850.0	-440.0 – 725.0	-895.0 – 925.0
20	4	p_T^{miss}	90.0%	8	36271200.0	-360.0 – 905.0	-930.0 – 955.0
20	4	p_T^{miss}	95.0%	8	39854450.0	-395.0 – 940.0	-1000.0 – 1025.0
20	4	p_T^{miss}	99.0%	8	45243675.0	-460.0 – 1005.0	-1115.0 – 1140.0

N_{min}	N_{min}^{bin}	Observable	CL	Bins	Area [TeV^{-8}]	$f_{T,1}$ [TeV^{-4}]	$f_{T,5}$ [TeV^{-4}]
30	3	η_γ	90.0%	16	67645950.0	-505.0 – 1075.0	-1255.0 – 1305.0
30	3	η_γ	95.0%	16	74755300.0	-550.0 – 1125.0	-1350.0 – 1395.0
30	3	η_γ	99.0%	16		-630.0 – 1205.0	
30	3	η_l	90.0%	15	62617375.0	-510.0 – 1090.0	-1250.0 – 1300.0
30	3	η_l	95.0%	15	69602575.0	-560.0 – 1140.0	-1345.0 – 1390.0
30	3	η_l	99.0%	15		-645.0 – 1220.0	
30	3	η_{miss}	90.0%	15	62617375.0	-510.0 – 1090.0	-1250.0 – 1300.0
30	3	η_{miss}	95.0%	15	69602575.0	-560.0 – 1140.0	-1345.0 – 1390.0
30	3	η_{miss}	99.0%	15		-645.0 – 1220.0	
30	3	$min(p_T^l, p_T^\gamma)$	90.0%	8	51244375.0	-305.0 – 640.0	-805.0 – 855.0
30	3	$min(p_T^l, p_T^\gamma)$	95.0%	8	53398625.0	-335.0 – 675.0	-865.0 – 915.0
30	3	$min(p_T^l, p_T^\gamma)$	99.0%	8	56649025.0	-385.0 – 730.0	-970.0 – 1015.0
30	3	$min(p_T^W, p_T^\gamma)$	90.0%	11	83611800.0	-300.0 – 720.0	-950.0 – 1020.0
30	3	$min(p_T^W, p_T^\gamma)$	95.0%	11	85147500.0	-330.0 – 755.0	-1025.0 – 1090.0
30	3	$min(p_T^W, p_T^\gamma)$	99.0%	11	87507400.0	-380.0 – 805.0	-1140.0 – 1205.0
30	3	$m_{j_1 j_2}$	90.0%	11	55821875.0	-475.0 – 1000.0	-1165.0 – 1205.0
30	3	$m_{j_1 j_2}$	95.0%	11	60218950.0	-525.0 – 1050.0	-1255.0 – 1290.0
30	3	$m_{j_1 j_2}$	99.0%	11	66808075.0	-600.0 – 1130.0	-1395.0 – 1430.0
30	3	$m_{l\gamma}$	90.0%	7	40582250.0	-325.0 – 670.0	-670.0 – 710.0
30	3	$m_{l\gamma}$	95.0%	7	42143100.0	-355.0 – 705.0	-720.0 – 765.0
30	3	$m_{l\gamma}$	99.0%	7	44559575.0	-410.0 – 765.0	-805.0 – 850.0
30	3	$m_T(W\gamma)$	90.0%	6	34695025.0	-275.0 – 675.0	-620.0 – 660.0
30	3	$m_T(W\gamma)$	95.0%	6	35767750.0	-305.0 – 710.0	-670.0 – 710.0
30	3	$m_T(W\gamma)$	99.0%	6	37542550.0	-355.0 – 760.0	-750.0 – 790.0
30	3	$\phi_{l\gamma}$	90.0%	11	72547300.0	-580.0 – 1190.0	-1350.0 – 1425.0
30	3	$\phi_{l\gamma}$	95.0%	11		-640.0 – 1250.0	
30	3	$\phi_{l\gamma}$	99.0%	11		-735.0 – 1350.0	
30	3	p_T^γ	90.0%	8	14537900.0	-260.0 – 600.0	-630.0 – 660.0
30	3	p_T^γ	95.0%	8	16849200.0	-290.0 – 630.0	-680.0 – 710.0
30	3	p_T^γ	99.0%	8	20954975.0	-335.0 – 675.0	-755.0 – 785.0
30	3	$p_T^{j_1}$	90.0%	9	50169300.0	-320.0 – 505.0	-665.0 – 685.0
30	3	$p_T^{j_1}$	95.0%	9	53172950.0	-350.0 – 535.0	-715.0 – 735.0
30	3	$p_T^{j_1}$	99.0%	9	57318300.0	-400.0 – 590.0	-795.0 – 820.0
30	3	$p_T^{j_2}$	90.0%	8	33001500.0	-460.0 – 1015.0	-1185.0 – 1230.0
30	3	$p_T^{j_2}$	95.0%	8	36897725.0	-505.0 – 1060.0	-1275.0 – 1325.0
30	3	$p_T^{j_2}$	99.0%	8	42814900.0	-585.0 – 1140.0	-1420.0 – 1470.0
30	3	p_T^l	90.0%	8	46210575.0	-360.0 – 660.0	-795.0 – 825.0
30	3	p_T^l	95.0%	8	48523325.0	-400.0 – 700.0	-855.0 – 885.0
30	3	p_T^l	99.0%	8	52042575.0	-455.0 – 760.0	-950.0 – 985.0
30	3	p_T^{miss}	90.0%	8	38316675.0	-365.0 – 915.0	-945.0 – 975.0
30	3	p_T^{miss}	95.0%	8	41983750.0	-405.0 – 950.0	-1020.0 – 1045.0
30	3	p_T^{miss}	99.0%	8	47468675.0	-465.0 – 1015.0	-1135.0 – 1160.0

C.5. $\mathcal{L}_{T,1} - \mathcal{L}_{T,6}$

N_{min}	N_{min}^{bin}	Observable	CL	Bins	Area [TeV^{-8}]	$f_{T,1}$ [TeV^{-4}]	$f_{T,6}$ [TeV^{-4}]
20	4	η_γ	90.0%	13	47899375.0	-495.0 – 1090.0	-1065.0 – 1200.0
20	4	η_γ	95.0%	13	53747650.0	-545.0 – 1140.0	-1150.0 – 1280.0
20	4	η_γ	99.0%	13	63288100.0	-625.0 – 1220.0	-1280.0 – 1415.0
20	4	η_l	90.0%	13	51040500.0	-505.0 – 1100.0	-1085.0 – 1220.0
20	4	η_l	95.0%	13	57029050.0	-555.0 – 1155.0	-1170.0 – 1305.0
20	4	η_l	99.0%	13	66722250.0	-640.0 – 1235.0	-1305.0 – 1440.0
20	4	η_{miss}	90.0%	13	51040500.0	-505.0 – 1100.0	-1085.0 – 1220.0
20	4	η_{miss}	95.0%	13	57029050.0	-555.0 – 1155.0	-1170.0 – 1305.0
20	4	η_{miss}	99.0%	13	66722250.0	-640.0 – 1235.0	-1305.0 – 1440.0
20	4	$min(p_T^l, p_T^\gamma)$	90.0%	8	47874650.0	-295.0 – 610.0	-705.0 – 780.0
20	4	$min(p_T^l, p_T^\gamma)$	95.0%	8	50231950.0	-325.0 – 645.0	-765.0 – 835.0
20	4	$min(p_T^l, p_T^\gamma)$	99.0%	8	53727900.0	-375.0 – 695.0	-855.0 – 925.0
20	4	$min(p_T^W, p_T^\gamma)$	90.0%	11	79364950.0	-290.0 – 695.0	-835.0 – 970.0
20	4	$min(p_T^W, p_T^\gamma)$	95.0%	11	81244100.0	-320.0 – 725.0	-905.0 – 1040.0
20	4	$min(p_T^W, p_T^\gamma)$	99.0%	11	83978550.0	-370.0 – 775.0	-1010.0 – 1145.0
20	4	$m_{j_1 j_2}$	90.0%	11	52856750.0	-480.0 – 1015.0	-1045.0 – 1170.0
20	4	$m_{j_1 j_2}$	95.0%	11	57232650.0	-530.0 – 1065.0	-1125.0 – 1250.0
20	4	$m_{j_1 j_2}$	99.0%	11	64182575.0	-605.0 – 1145.0	-1255.0 – 1380.0
20	4	$m_{l\gamma}$	90.0%	7	37769575.0	-325.0 – 675.0	-615.0 – 645.0
20	4	$m_{l\gamma}$	95.0%	7	39298275.0	-360.0 – 710.0	-660.0 – 695.0
20	4	$m_{l\gamma}$	99.0%	7	41852950.0	-415.0 – 770.0	-740.0 – 770.0
20	4	$m_T(W\gamma)$	90.0%	6	31866800.0	-275.0 – 685.0	-550.0 – 575.0
20	4	$m_T(W\gamma)$	95.0%	6	33321025.0	-305.0 – 715.0	-595.0 – 620.0
20	4	$m_T(W\gamma)$	99.0%	6	35036450.0	-355.0 – 765.0	-665.0 – 690.0
20	4	$\phi_{l\gamma}$	90.0%	13	89656675.0	-600.0 – 1210.0	-1185.0 – 1320.0
20	4	$\phi_{l\gamma}$	95.0%	13	95312800.0	-660.0 – 1275.0	-1275.0 – 1415.0
20	4	$\phi_{l\gamma}$	99.0%	13		-760.0 – 1375.0	
20	4	p_T^γ	90.0%	8	10880900.0	-255.0 – 565.0	-550.0 – 585.0
20	4	p_T^γ	95.0%	8	12621550.0	-280.0 – 600.0	-590.0 – 630.0
20	4	p_T^γ	99.0%	8	15709750.0	-325.0 – 645.0	-660.0 – 695.0
20	4	$p_T^{j_1}$	90.0%	9	46379950.0	-315.0 – 480.0	-580.0 – 605.0
20	4	$p_T^{j_1}$	95.0%	9	49593225.0	-340.0 – 510.0	-625.0 – 650.0
20	4	$p_T^{j_1}$	99.0%	9	54062200.0	-390.0 – 560.0	-695.0 – 720.0
20	4	$p_T^{j_2}$	90.0%	8	30330850.0	-460.0 – 1020.0	-1040.0 – 1180.0
20	4	$p_T^{j_2}$	95.0%	8	34037625.0	-505.0 – 1065.0	-1125.0 – 1265.0
20	4	$p_T^{j_2}$	99.0%	8	40119175.0	-585.0 – 1145.0	-1260.0 – 1400.0
20	4	p_T^l	90.0%	7	33656175.0	-350.0 – 635.0	-705.0 – 750.0
20	4	p_T^l	95.0%	7	36105300.0	-385.0 – 675.0	-760.0 – 805.0
20	4	p_T^l	99.0%	7	39966500.0	-445.0 – 735.0	-850.0 – 895.0
20	4	p_T^{miss}	90.0%	8	36107700.0	-360.0 – 930.0	-805.0 – 885.0
20	4	p_T^{miss}	95.0%	8	39618850.0	-400.0 – 970.0	-865.0 – 945.0
20	4	p_T^{miss}	99.0%	8	44950150.0	-465.0 – 1035.0	-970.0 – 1050.0

N_{min}	N_{min}^{bin}	Observable	CL	Bins	Area [TeV^{-8}]	$f_{T,1}$ [TeV^{-4}]	$f_{T,6}$ [TeV^{-4}]
30	3	η_γ	90.0%	16	63433475.0	-510.0 – 1105.0	-1090.0 – 1225.0
30	3	η_γ	95.0%	16	70718725.0	-560.0 – 1155.0	-1175.0 – 1310.0
30	3	η_γ	99.0%	16	82464075.0	-640.0 – 1235.0	-1305.0 – 1440.0
30	3	η_l	90.0%	15	59602075.0	-515.0 – 1110.0	-1100.0 – 1240.0
30	3	η_l	95.0%	15	66666550.0	-565.0 – 1165.0	-1185.0 – 1325.0
30	3	η_l	99.0%	15	77945700.0	-650.0 – 1245.0	-1320.0 – 1460.0
30	3	η_{miss}	90.0%	15	59602075.0	-515.0 – 1110.0	-1100.0 – 1240.0
30	3	η_{miss}	95.0%	15	66666550.0	-565.0 – 1165.0	-1185.0 – 1325.0
30	3	η_{miss}	99.0%	15	77945700.0	-650.0 – 1245.0	-1320.0 – 1460.0
30	3	$min(p_T^l, p_T^\gamma)$	90.0%	8	50817625.0	-305.0 – 650.0	-745.0 – 830.0
30	3	$min(p_T^l, p_T^\gamma)$	95.0%	8	53113725.0	-335.0 – 680.0	-805.0 – 890.0
30	3	$min(p_T^l, p_T^\gamma)$	99.0%	8	56430775.0	-390.0 – 735.0	-900.0 – 985.0
30	3	$min(p_T^W, p_T^\gamma)$	90.0%	11	83571225.0	-300.0 – 720.0	-880.0 – 1035.0
30	3	$min(p_T^W, p_T^\gamma)$	95.0%	11	85150300.0	-330.0 – 755.0	-950.0 – 1105.0
30	3	$min(p_T^W, p_T^\gamma)$	99.0%	11	87466375.0	-380.0 – 805.0	-1065.0 – 1215.0
30	3	$m_{j_1 j_2}$	90.0%	11	54104350.0	-480.0 – 1015.0	-1045.0 – 1170.0
30	3	$m_{j_1 j_2}$	95.0%	11	58664850.0	-530.0 – 1065.0	-1125.0 – 1250.0
30	3	$m_{j_1 j_2}$	99.0%	11	65639850.0	-605.0 – 1145.0	-1255.0 – 1380.0
30	3	$m_{l\gamma}$	90.0%	7	40201225.0	-325.0 – 685.0	-630.0 – 665.0
30	3	$m_{l\gamma}$	95.0%	7	41854050.0	-360.0 – 720.0	-675.0 – 715.0
30	3	$m_{l\gamma}$	99.0%	7	44296525.0	-415.0 – 780.0	-755.0 – 795.0
30	3	$m_T(W\gamma)$	90.0%	6	34708375.0	-275.0 – 695.0	-575.0 – 605.0
30	3	$m_T(W\gamma)$	95.0%	6	35768525.0	-305.0 – 725.0	-620.0 – 655.0
30	3	$m_T(W\gamma)$	99.0%	6	37524325.0	-355.0 – 775.0	-695.0 – 725.0
30	3	$\phi_{l\gamma}$	90.0%	11	72588000.0	-585.0 – 1195.0	-1165.0 – 1300.0
30	3	$\phi_{l\gamma}$	95.0%	11	77727675.0	-645.0 – 1260.0	-1255.0 – 1390.0
30	3	$\phi_{l\gamma}$	99.0%	11		-745.0 – 1365.0	
30	3	p_T^γ	90.0%	8	14514800.0	-260.0 – 605.0	-590.0 – 645.0
30	3	p_T^γ	95.0%	8	16822750.0	-290.0 – 635.0	-640.0 – 690.0
30	3	p_T^γ	99.0%	8	20921825.0	-335.0 – 685.0	-715.0 – 765.0
30	3	$p_T^{j_1}$	90.0%	9	48764625.0	-325.0 – 510.0	-615.0 – 640.0
30	3	$p_T^{j_1}$	95.0%	9	51958450.0	-355.0 – 545.0	-660.0 – 690.0
30	3	$p_T^{j_1}$	99.0%	9	56376950.0	-405.0 – 595.0	-735.0 – 765.0
30	3	$p_T^{j_2}$	90.0%	8	31416125.0	-460.0 – 1025.0	-1045.0 – 1185.0
30	3	$p_T^{j_2}$	95.0%	8	35256075.0	-510.0 – 1075.0	-1130.0 – 1270.0
30	3	$p_T^{j_2}$	99.0%	8	41456675.0	-590.0 – 1155.0	-1265.0 – 1405.0
30	3	p_T^l	90.0%	8	45643700.0	-365.0 – 665.0	-745.0 – 800.0
30	3	p_T^l	95.0%	8	48048350.0	-400.0 – 705.0	-800.0 – 860.0
30	3	p_T^l	99.0%	8	51721925.0	-460.0 – 765.0	-895.0 – 950.0
30	3	p_T^{miss}	90.0%	8	38220800.0	-365.0 – 940.0	-820.0 – 905.0
30	3	p_T^{miss}	95.0%	8	41821475.0	-405.0 – 980.0	-885.0 – 970.0
30	3	p_T^{miss}	99.0%	8	47217075.0	-470.0 – 1045.0	-990.0 – 1075.0

C.6. $\mathcal{L}_{T,5} - \mathcal{L}_{T,6}$

N_{min}	N_{min}^{bin}	Observable	CL	Bins	Area [TeV^{-8}]	$f_{T,5}$ [TeV^{-4}]	$f_{T,6}$ [TeV^{-4}]
20	4	η_γ	90.0%	13	18980325.0	-535.0 – 565.0	-570.0 – 655.0
20	4	η_γ	95.0%	13	21849800.0	-575.0 – 605.0	-615.0 – 700.0
20	4	η_γ	99.0%	13	26871625.0	-640.0 – 665.0	-690.0 – 770.0
20	4	η_l	90.0%	13	20249000.0	-535.0 – 565.0	-590.0 – 675.0
20	4	η_l	95.0%	13	23309050.0	-575.0 – 605.0	-635.0 – 720.0
20	4	η_l	99.0%	13	28667150.0	-640.0 – 670.0	-710.0 – 795.0
20	4	η_{miss}	90.0%	13	20249000.0	-535.0 – 565.0	-590.0 – 675.0
20	4	η_{miss}	95.0%	13	23309050.0	-575.0 – 605.0	-635.0 – 720.0
20	4	η_{miss}	99.0%	13	28667150.0	-640.0 – 670.0	-710.0 – 795.0
20	4	$min(p_T^l, p_T^\gamma)$	90.0%	8	15870400.0	-340.0 – 375.0	-360.0 – 420.0
20	4	$min(p_T^l, p_T^\gamma)$	95.0%	8	16995250.0	-365.0 – 400.0	-385.0 – 450.0
20	4	$min(p_T^l, p_T^\gamma)$	99.0%	8	18915525.0	-410.0 – 445.0	-435.0 – 495.0
20	4	$min(p_T^W, p_T^\gamma)$	90.0%	11	31314850.0	-445.0 – 490.0	-470.0 – 580.0
20	4	$min(p_T^W, p_T^\gamma)$	95.0%	11	33343450.0	-480.0 – 525.0	-510.0 – 615.0
20	4	$min(p_T^W, p_T^\gamma)$	99.0%	11	36914400.0	-535.0 – 580.0	-570.0 – 680.0
20	4	$m_{j_1 j_2}$	90.0%	11	27707750.0	-505.0 – 530.0	-570.0 – 650.0
20	4	$m_{j_1 j_2}$	95.0%	11	30559950.0	-540.0 – 565.0	-610.0 – 690.0
20	4	$m_{j_1 j_2}$	99.0%	11	35446150.0	-605.0 – 630.0	-685.0 – 765.0
20	4	$m_{l\gamma}$	90.0%	7	14336050.0	-230.0 – 255.0	-255.0 – 295.0
20	4	$m_{l\gamma}$	95.0%	7	15174400.0	-245.0 – 270.0	-275.0 – 315.0
20	4	$m_{l\gamma}$	99.0%	7	16671350.0	-275.0 – 300.0	-310.0 – 350.0
20	4	$m_T(W\gamma)$	90.0%	6	13429725.0	-210.0 – 235.0	-225.0 – 270.0
20	4	$m_T(W\gamma)$	95.0%	6	14134600.0	-225.0 – 250.0	-245.0 – 290.0
20	4	$m_T(W\gamma)$	99.0%	6	15397600.0	-255.0 – 280.0	-275.0 – 320.0
20	4	$\phi_{l\gamma}$	90.0%	13	82747525.0	-525.0 – 565.0	-575.0 – 665.0
20	4	$\phi_{l\gamma}$	95.0%	13	87278125.0	-565.0 – 605.0	-620.0 – 710.0
20	4	$\phi_{l\gamma}$	99.0%	13	92889050.0	-630.0 – 665.0	-695.0 – 780.0
20	4	p_T^γ	90.0%	8	8826675.0	-290.0 – 320.0	-305.0 – 375.0
20	4	p_T^γ	95.0%	8	10206375.0	-310.0 – 345.0	-330.0 – 400.0
20	4	p_T^γ	99.0%	8	12661775.0	-350.0 – 380.0	-370.0 – 440.0
20	4	$p_T^{j_1}$	90.0%	9	24009100.0	-215.0 – 250.0	-290.0 – 305.0
20	4	$p_T^{j_1}$	95.0%	9	26549975.0	-235.0 – 265.0	-315.0 – 325.0
20	4	$p_T^{j_1}$	99.0%	9	30832900.0	-260.0 – 295.0	-350.0 – 365.0
20	4	$p_T^{j_2}$	90.0%	8	10129950.0	-515.0 – 540.0	-570.0 – 660.0
20	4	$p_T^{j_2}$	95.0%	8	11706050.0	-550.0 – 580.0	-615.0 – 705.0
20	4	$p_T^{j_2}$	99.0%	8	14507150.0	-615.0 – 645.0	-690.0 – 780.0
20	4	p_T^l	90.0%	7	5618875.0	-285.0 – 305.0	-325.0 – 360.0
20	4	p_T^l	95.0%	7	6507500.0	-305.0 – 325.0	-355.0 – 390.0
20	4	p_T^l	99.0%	7	8092650.0	-340.0 – 365.0	-395.0 – 430.0
20	4	p_T^{miss}	90.0%	8	6857325.0	-345.0 – 365.0	-340.0 – 400.0
20	4	p_T^{miss}	95.0%	8	7929100.0	-375.0 – 390.0	-370.0 – 430.0
20	4	p_T^{miss}	99.0%	8	9835625.0	-415.0 – 435.0	-415.0 – 475.0

N_{min}	N_{min}^{bin}	Observable	CL	Bins	Area [TeV^{-8}]	$f_{T,5}$ [TeV^{-4}]	$f_{T,6}$ [TeV^{-4}]
30	3	η_γ	90.0%	16	26554775.0	-545.0 – 575.0	-585.0 – 670.0
30	3	η_γ	95.0%	16	30527325.0	-585.0 – 615.0	-630.0 – 715.0
30	3	η_γ	99.0%	16	37420450.0	-650.0 – 680.0	-705.0 – 785.0
30	3	η_l	90.0%	15	23305975.0	-545.0 – 570.0	-600.0 – 685.0
30	3	η_l	95.0%	15	26802700.0	-585.0 – 615.0	-645.0 – 730.0
30	3	η_l	99.0%	15	32891725.0	-650.0 – 675.0	-720.0 – 805.0
30	3	η_{miss}	90.0%	15	23305975.0	-545.0 – 570.0	-600.0 – 685.0
30	3	η_{miss}	95.0%	15	26802700.0	-585.0 – 615.0	-645.0 – 730.0
30	3	η_{miss}	99.0%	15	32891725.0	-650.0 – 675.0	-720.0 – 805.0
30	3	$min(p_T^l, p_T^\gamma)$	90.0%	8	16847150.0	-365.0 – 400.0	-380.0 – 445.0
30	3	$min(p_T^l, p_T^\gamma)$	95.0%	8	18123225.0	-390.0 – 425.0	-410.0 – 480.0
30	3	$min(p_T^l, p_T^\gamma)$	99.0%	8	20314500.0	-435.0 – 475.0	-460.0 – 530.0
30	3	$min(p_T^W, p_T^\gamma)$	90.0%	11	37634075.0	-480.0 – 535.0	-515.0 – 645.0
30	3	$min(p_T^W, p_T^\gamma)$	95.0%	11	40631225.0	-515.0 – 570.0	-555.0 – 690.0
30	3	$min(p_T^W, p_T^\gamma)$	99.0%	11	45905825.0	-575.0 – 630.0	-625.0 – 755.0
30	3	$m_{j_1 j_2}$	90.0%	11	26883000.0	-505.0 – 530.0	-565.0 – 650.0
30	3	$m_{j_1 j_2}$	95.0%	11	30102625.0	-545.0 – 570.0	-610.0 – 690.0
30	3	$m_{j_1 j_2}$	99.0%	11	35535875.0	-605.0 – 630.0	-685.0 – 765.0
30	3	$m_{l\gamma}$	90.0%	7	14863325.0	-245.0 – 270.0	-270.0 – 315.0
30	3	$m_{l\gamma}$	95.0%	7	15784600.0	-265.0 – 290.0	-295.0 – 335.0
30	3	$m_{l\gamma}$	99.0%	7	17429075.0	-295.0 – 320.0	-330.0 – 370.0
30	3	$m_T(W\gamma)$	90.0%	6	13597150.0	-230.0 – 255.0	-245.0 – 295.0
30	3	$m_T(W\gamma)$	95.0%	6	14327175.0	-250.0 – 275.0	-265.0 – 315.0
30	3	$m_T(W\gamma)$	99.0%	6	15637725.0	-280.0 – 305.0	-300.0 – 350.0
30	3	$\phi_{l\gamma}$	90.0%	11	65621625.0	-520.0 – 555.0	-565.0 – 655.0
30	3	$\phi_{l\gamma}$	95.0%	11	69990025.0	-560.0 – 595.0	-610.0 – 700.0
30	3	$\phi_{l\gamma}$	99.0%	11	75543325.0	-620.0 – 660.0	-685.0 – 770.0
30	3	p_T^γ	90.0%	8	10547050.0	-310.0 – 345.0	-325.0 – 405.0
30	3	p_T^γ	95.0%	8	12196825.0	-335.0 – 370.0	-355.0 – 435.0
30	3	p_T^γ	99.0%	8	15127775.0	-375.0 – 410.0	-400.0 – 480.0
30	3	$p_T^{j_1}$	90.0%	9	23461300.0	-235.0 – 265.0	-310.0 – 325.0
30	3	$p_T^{j_1}$	95.0%	9	26490975.0	-250.0 – 280.0	-335.0 – 350.0
30	3	$p_T^{j_1}$	99.0%	9	31439425.0	-280.0 – 310.0	-375.0 – 390.0
30	3	$p_T^{j_2}$	90.0%	8	10343000.0	-515.0 – 545.0	-570.0 – 660.0
30	3	$p_T^{j_2}$	95.0%	8	11952775.0	-555.0 – 585.0	-615.0 – 705.0
30	3	$p_T^{j_2}$	99.0%	8	14812275.0	-620.0 – 650.0	-690.0 – 780.0
30	3	p_T^l	90.0%	8	15667000.0	-310.0 – 335.0	-350.0 – 395.0
30	3	p_T^l	95.0%	8	16704150.0	-335.0 – 355.0	-380.0 – 420.0
30	3	p_T^l	99.0%	8	18550600.0	-375.0 – 395.0	-425.0 – 465.0
30	3	p_T^{miss}	90.0%	8	11181125.0	-360.0 – 380.0	-360.0 – 425.0
30	3	p_T^{miss}	95.0%	8	12768775.0	-390.0 – 410.0	-390.0 – 450.0
30	3	p_T^{miss}	99.0%	8	15409825.0	-435.0 – 455.0	-435.0 – 500.0

BIBLIOGRAPHY

[1] V. Trimble, "Existence and Nature of Dark Matter in the Universe," *Ann.Rev.Astron.Astrophys.* **25** (1987) 425–472.

[2] S. Bodenstein, C. Dominguez, K. Schilcher, and H. Spiesberger, "Hadronic Contribution to the muon $g-2$ factor," 1302.1735.

[3] **CMS Collaboration** Collaboration, S. Chatrchyan *et. al.*, "Observation of a new boson at a mass of 125 GeV with the CMS experiment at the LHC," *Phys.Lett.* **B716** (2012) 30–61, 1207.7235.

[4] **ATLAS Collaboration** Collaboration, G. Aad *et. al.*, "Observation of a new particle in the search for the Standard Model Higgs boson with the ATLAS detector at the LHC," *Phys.Lett.* **B716** (2012) 1–29, 1207.7214.

[5] F. Campanario and S. Sapeta, "WZ production beyond NLO for high-pT observables," *Phys.Lett.* **B718** (2012) 100–104, 1209.4595.

[6] **The ATLAS Collaboration** Collaboration, G. Aad *et. al.*, "Measurements of Wgamma and Zgamma production in pp collisions at sqrts= 7 TeV with the ATLAS detector at the LHC," 1302.1283.

[7] "Search for exclusive two-photon production of w^+w^- pairs in pp collisions at 7 tev," Tech. Rep. CMS-PAS-FSQ-12-010, CERN, Geneva, 2013.

[8] K. Arnold, J. Bellm, G. Bozzi, F. Campanario, C. Englert, *et. al.*, "Release Note – Vbfnlo-2.6.0," 1207.4975.

[9] M. E. Peskin and D. V. Schroeder, *An introduction to quantum field theory*. Westview Pr., Boulder, Colo. [u.a.], 2006.

[10] S. Weinberg, "A model of leptons," *Phys. Rev. Lett.* **19** (Nov, 1967) 1264–1266.

[11] A. Salam and J. C. Ward, "Weak and electromagnetic interactions," *Nuovo Cim.* **11** (1959) 568–577.

[12] S. Glashow, "Partial Symmetries of Weak Interactions," *Nucl.Phys.* **22** (1961) 579–588.

[13] P. W. Higgs, "Broken symmetries and the masses of gauge bosons," *Phys. Rev. Lett.* **13** (Oct, 1964) 508–509.

[14] D. J. Gross and F. Wilczek, "Ultraviolet behavior of non-abelian gauge theories," *Phys. Rev. Lett.* **30** (Jun, 1973) 1343–1346.

[15] H. D. Politzer, "Reliable perturbative results for strong interactions?," *Phys. Rev. Lett.* **30** (Jun, 1973) 1346–1349.

[16] P. Z. Quintas, "Measurement of Λ_{QCD} from ν_μ-Fe nonsinglet structure functions at the Fermilab Tevatron," *Phys. Rev. Lett.* **71** (Aug, 1993) 1307–1310.

[17] F. L. Wilson, "Fermi's theory of beta decay," *American Journal of Physics* **36** (1968), no. 12 1150–1160.

[18] **ALEPH Collaboration, DELPHI Collaboration, L3 Collaboration, OPAL Collaboration, LEP Electroweak Working Group** Collaboration, J. Alcaraz *et. al.*, "A Combination of preliminary electroweak measurements and constraints on the standard model," `hep-ex/0612034`.

[19] O. Eboli, M. Gonzalez-Garcia, and J. Mizukoshi, "p p → j j e+- mu+- nu nu and j j e+- mu-+ nu nu at O(alpha(em)**6) and O(alpha(em)**4 alpha(s)**2) for the study of the quartic electroweak gauge boson vertex at CERN LHC," *Phys.Rev.* **D74** (2006) 073005, `hep-ph/0606118`.

[20] G. Altarelli and G. Parisi, "Asymptotic Freedom in Parton Language," *Nucl.Phys.* **B126** (1977) 298.

[21] Y. L. Dokshitzer, "Calculation of the Structure Functions for Deep Inelastic Scattering and e+ e- Annihilation by Perturbation Theory in Quantum Chromodynamics.," *Sov.Phys.JETP* **46** (1977) 641–653.

[22] V. Gribov and L. Lipatov, "Deep inelastic e p scattering in perturbation theory," *Sov.J.Nucl.Phys.* **15** (1972) 438–450.

[23] M. Whalley, D. Bourilkov, and R. Group, "The Les Houches accord PDFs (LHAPDF) and LHAGLUE," `hep-ph/0508110`.

[24] J. Pumplin, D. Stump, J. Huston, H. Lai, P. M. Nadolsky, *et. al.*, "New generation of parton distributions with uncertainties from global QCD analysis," *JHEP* **0207** (2002) 012, `hep-ph/0201195`.

[25] H.-L. Lai, M. Guzzi, J. Huston, Z. Li, P. M. Nadolsky, *et. al.*, "New parton distributions for collider physics," *Phys.Rev.* **D82** (2010) 074024, `1007.2241`.

[26] S. Frixione, "Isolated photons in perturbative QCD," *Phys.Lett.* **B429** (1998) 369–374, `hep-ph/9801442`.

[27] D. Zeppenfeld, "Collider physics," `hep-ph/9902307`.

[28] G. P. Lepage, "VEGAS: AN ADAPTIVE MULTIDIMENSIONAL INTEGRATION PROGRAM,".
G. P. Lepage, "A new algorithm for adaptive multidimensional integration," *Journal of Computational Physics* **27** (1978), no. 2 192 – 203.

[29] J. Alwall, A. Ballestrero, P. Bartalini, S. Belov, E. Boos, *et. al.*, "A Standard format for Les Houches event files," *Comput.Phys.Commun.* **176** (2007) 300–304, hep-ph/0609017.

[30] M. Dobbs and J. B. Hansen, "The HepMC C++ Monte Carlo event record for High Energy Physics," *Comput.Phys.Commun.* **134** (2001) 41–46.

[31] H. Murayama, I. Watanabe, and K. Hagiwara, "HELAS: HELicity amplitude subroutines for Feynman diagram evaluations,".

[32] A. Denner and S. Dittmaier, "The Complex-mass scheme for perturbative calculations with unstable particles," *Nucl.Phys.Proc.Suppl.* **160** (2006) 22–26, hep-ph/0605312.

[33] G. Bozzi, B. Jager, C. Oleari, and D. Zeppenfeld, "Next-to-leading order QCD corrections to W+ Z and W- Z production via vector-boson fusion," *Phys.Rev.* **D75** (2007) 073004, hep-ph/0701105.

[34] S. Catani and M. Seymour, "The Dipole formalism for the calculation of QCD jet cross-sections at next-to-leading order," *Phys.Lett.* **B378** (1996) 287–301, hep-ph/9602277.

[35] T. Kinoshita, "Mass singularities of feynman amplitudes," *Journal of Mathematical Physics* **3** (1962), no. 4 650–677.
T. D. Lee and M. Nauenberg, "Degenerate systems and mass singularities," *Phys. Rev.* **133** (Mar, 1964) B1549–B1562.

[36] T. Figy, C. Oleari, and D. Zeppenfeld, "Next-to-leading order jet distributions for Higgs boson production via weak boson fusion," *Phys.Rev.* **D68** (2003) 073005, hep-ph/0306109.

[37] F. Campanario, "Towards pp $\to$ VVjj at NLO QCD: Bosonic contributions to triple vector boson production plus jet," *JHEP* **1110** (2011) 070, 1105.0920.

[38] G. Passarino and M. Veltman, "One-loop corrections for e+eâ annihilation into $\hat{\mathrm{I}}\frac{1}{4}+\hat{\mathrm{I}}\frac{1}{4}\hat{\mathrm{a}}$ in the weinberg model," *Nuclear Physics B* **160** (1979), no. 1 151 – 207.

[39] G. 't Hooft and M. Veltman, "Regularization and renormalization of gauge fields," *Nuclear Physics B* **44** (July, 1972) 189–213.

[40] W. Siegel, "Supersymmetric dimensional regularization via dimensional reduction," *Physics Letters B* **84** (1979), no. 2 193–196.

[41] J. Alwall, P. Demin, S. de Visscher, R. Frederix, M. Herquet, *et. al.*, "MadGraph/MadEvent v4: The New Web Generation," *JHEP* **0709** (2007) 028, 0706.2334.

[42] T. Gleisberg, S. Höche, F. Krauss, M. Schönherr, S. Schumann, *et. al.*, "Event generation with Sherpa 1.1," *JHEP* **0902** (2009) 007, 0811.4622.

[43] C. Oleari and D. Zeppenfeld, "QCD corrections to electroweak nu(l) j j and l+ l- j j production," *Phys.Rev.* **D69** (2004) 093004, hep-ph/0310156.

[44] O. Schlimpert, "Anomale Kopplungen bei der Streuung schwacher Eichbosonen," Diplomarbeit, ITP, KIT, http://www.itp.kit.edu/diplomatheses.de.shtml, 2013.

[45] M. Seymour, "Jet shapes in hadron collisions: Higher orders, resummation and hadronization," *Nucl.Phys.* **B513** (1998) 269–300, `hep-ph/9707338`.

[46] U. Baur, T. Han, and J. Ohnemus, "QCD corrections to hadronic $W\gamma$ production with nonstandard $WW\gamma$ couplings," *Phys.Rev.* **D48** (1993) 5140–5161, `hep-ph/9305314`.

[47] J. Bellm, "NLO-QCD-Korrekturen zur WZ- und Wγ-Produktion am LHC," Diplomarbeit, ITP, KIT, `http://www.itp.kit.edu/diplomatheses.de.shtml`, 2012.

[48] I. W. Stewart and F. J. Tackmann, "Theory Uncertainties for Higgs and Other Searches Using Jet Bins," *Phys.Rev.* **D85** (2012) 034011, `1107.2117`.

ACKNOWLEDGEMENTS

First of all, I want to thank Prof. Dr. Zeppenfeld for providing me with this interesting topic of current research. His suggestions and his willingness to give me advise whenever it was needed were always highly appreciated. Also, I am grateful for the possibility to visit the annual conference of the DPG in Dresden 2013.

I thank Prof. Dr. U. Nierste for agreeing to be the second referee of my thesis.

My very special thanks goes to Paco (Francisco Campanario) for the numerous explanations and taking the time to answer all my questions. Without this extraordinary commitment this work would not have been possible.

Furthermore, I would like to thank all members of the institute for the pleasant atmosphere and the great willingness to help. Especially, I want to thank the people who proofread this thesis: Johannes Bellm, Matthias Kerner, Robin Roth and Joel Weller.

I want to thank the people with whom I worked during my internships: Alex Himmel, Siegfried Numberger, Kate Scholberg and Peter Wurth. Those experiences have been an important part of my way.

Meinen Freunden und meiner Schwester möchte ich für den Rückhalt und die gemeinsame Zeit danken. Mein besonderer Dank gilt meinen Eltern, dafür, dass sie mir mein Studium ermöglicht und mich dabei stets unterstützt haben. Ganz besonders danke ich auch meiner Freundin Diana für all ihre Liebe und Unterstützung.